EXPERIMENTAL AND THEORETICAL ANALYSIS OF HEAT TRANSFER ON A TRANSONIC BLADE

by

Zaahir Ahmed Essa

Dissertation submitted in fulfilment of the academic requirements for the degree of Master of Science in Mechanical Engineering.

Supervisor: Dr F. Inambao

University of KwaZulu-Natal

Durban

2008

ABSTRACT

This dissertation involves the experimental and numerical analysis of heat transfer on a transonic high turning angle gas turbine blade, which has been performed on the supersonic cascade experimental facility at the University of KwaZulu-Natal (UKZN), as part of the continuous research and development project run under ARMSCOR. Efforts have been made to keep constant maintenance on the experimental rig. This now functional rig was used to generate experimental results, which were used to validate numerical models created using the commercially available computational fluid dynamics (CFD) package of FLUENT.

The facility at UKZN is a continuously running cascade system, which consists of a plenum run under vacuum pressure and houses a four-blade cascade. One of these SMR-95 turbine blades is instrumented with thin-film gauges, which allow heat transfer measurement via a heat transfer analogy through electrical circuit boards. This blade is interchangeable with an instrumented blade with pressure tappings along its span for pressure distribution tests. This facility was used to validate flow measurements, and results compared to previous test data conducted on the rig, using two pressure transducers, a scanivalve and a data acquisition system with LabView software.

The method of generating heat transfer measurement results involved pre-chilling the test blade in a cooling box, before rapidly plunging it directly into a hot-air stream. Re-instrumented and more sensitive thin-film gauges would react resistively according to the temperature change. The heat transfer coefficient distribution was calculated using LabView. The turbulence intensity at the inlet of the cascade was varied using a grid of rods of varying diameter. For 15% turbulence intensity, there was a 16% overall increase in heat transfer on the pressure side, and 25% increase on the suction side. For 25.5% turbulence intensity, there was an overall increase of 23% on the pressure side and 40% on the suction side. The results compared favourably to that of previous results generated by Stieger (1998).

The experimental results were used to validate and compare to the CFD model developed in FLUENT. Improvements were made with the meshes developed previously, and results obtained showed that the general trend of distribution was similar, although certain models varied in the correct prediction of magnitude.

This research includes a comprehensive study of various methods of numerical heat transfer measurement techniques, which would be used to replace the current ageing electrical heat transfer analogue method used at UKZN.

PREFACE

The author hereby states that this entire dissertation, unless specifically indicated to the contrary in the text, is his own original work, and has not been submitted in part or whole to any other university. This dissertation presents the work carried out by the author in the School of Mechanical Engineering at the University of KwaZulu-Natal, Howard College Campus, from March 2006 to March 2008. The project was initially supervised by Prof S. Govender, followed by Dr F. Inambao from October 2007, and forms part of the ongoing study in the turbine blade heat transfer and aerodynamic analysis field.

"Oh well, whatever, nevermind."

– Kurt Cobain

ACKNOWLEDGEMENTS

The following people all made this project and stay at the University possible and worthwhile:

I would like to thank Prof S. Govender, for kindly introducing me to the project, and his constant understanding and supervision throughout the project, as well as his professionalism, friendship and support. I would also like to thank Prof J. Visser, for allowing me to work on this research project.

Dr F. Inambao for showing good interest and helping me push through to the end of the project.

Thanks to Mr G. Snedden and Mr D. de Kock, for their help in the early stages of the project, Mr G. Scheepers, and a special mention of Mr K. Cassie, for helping me get going with the project easier and of course his advice and assistance during 2007.

The workshop staff at the School of Mechanical Engineering, for their help and easy-going nature during the project.

Mrs K. Naicker and Mrs O. Chetty, for sorting out all my admin issues during 2007, and thanks for putting up with my laid-back ways.

Thanks to the office companions; Keith, Jean, Adrian, and Johnathan, for some crazy times and fending off annoying students.

Thanks to Michel for being such an easy target on GeneRally; Meshanthan, Adi, Sebastian, Tilley, Kelvin, Nolan, for being awesome. A special thanks to my brothers-in-arms Azad and Mo, as well as little Naseem, and my family (especially my mum!), for their constant support.

Thank you to God, for making everything happen without worry.

Finally, to Divesha, thank you for getting me through the hardest of times. I cannot imagine where I'd be without you.

TABLE OF CONTENTS

LIST OF FIGURES

CHAPTER 4

CHAPTER 5

APPENDIX B

LIST OF TABLES

APPENDIX C

APPENDIX E

NOMENCLATURE

SYMBOLS

k-ε	kinetic energy term (k) and kinetic energy dissipation rate (ε) in turbulence modelling
k-ω	kinetic energy term (k) and specific dissipation rate (ω) in turbulence modelling
T	temperature
q	heat flux per unit area
$\dot{q}_s(t)$	heat flux rate per unit time
ε	thin-film gauge thickness
k	conductivity
θ	temperature change relative to ambient $(T - T_\infty)$
θ_s	temperature change relative to surface $(T_s - T_0)$
t	time
α	thermal diffusivity
ρ	density
R	thin-film resistance
α_R	temperature coefficient of resistance
κ	constant of proportionality
V	voltage
c	capacitance
c'	distributed electrical capacitance per unit length
r'	distributed electrical resistance per unit length
i	current
$\frac{A^*}{\beta}$	calibration constant for electrical analogue
D	blade chord length
μ	viscosity
U	velocity of the fluid
y^+	non-dimensionalised distance from a wall
H	Heaviside function
∇	differential operator
∇^2	Laplacian operator

P	pressure
x	distance upstream
d	diameter
h	difference in height
p_{op}	operating pressure
p	local gauge pressure (relative to p_{op})
Tu	turbulence intensity

SUBSCRIPTS

0	initial condition
1	metal film material
2	semi-infinite substrate
wall	blade wall
s	surface
∞	ambient condition (space), or infinity (time)
in	inlet
out	outlet
op	operating condition
x	x-coordinate
y	y-coordinate

ABBREVIATIONS

1-D	1-Dimensional
2-D	2-Dimensional
3-D	3-Dimensional
A/D	Analogue to Digital
CCD	Charge-Coupled Device
CFL	Courant Number
CSIR	Council for Scientific and Industrial Research
HP	High Pressure
I/O	Input/Output
LED	Light-Emitting Diode
LES	Large Eddy Simulations

LP	Low Pressure
RANS	Reynolds-Averaged Navier-Stokes
RKE	Realisable k-ε Turbulence Model
RNG	Renormalisation Group Theory
RSM	Reynolds Stress Model
SA	Spalart-Allmaras
SKW	Standard k-ω Turbulence Model
SST	Shear-Stress Transport
TFG	Thin-Film Gauge
TGP	Thermographic Phosphors
TIT	Turbine Inlet Temperature
TLC	Thermochromic Liquid Crystal
UKZN	University of KwaZulu-Natal
UV	Ultraviolet
VI	Virtual Instrument (from LabView)
VKI	Von Karman Institute
YAG	Neodymium Yittrium Aluminium Garnet

models will be discussed in chapter two and the research analysis in chapter four will be viewed in context of the general and Islamic theory. It is important to determine whether the conversion process and experience of the women in this research are aligned with the models that have been advocated. It is relevant at this stage to also discuss Berry's model of acculturation in terms of the women adapting to their new cultural surroundings and to briefly bring into consideration Dr. Joel Crohn's research on couples who marry from different cultural, religious and racial backgrounds and how it affects the marriage, especially as Köse raises this issue in his research.

Chapter three contextualizes the references of conversion to the Islamic traditions in the time of the Prophet Muhammad (pbuh), how the Prophet (pbuh) conducted himself in the context of accepting allegiance from his followers and his requirements of the wives who were not Muslim. It reflects on verses from the Qur'ān that indicate there is no compulsion or coercion in Islam and it looks at the legalities of who is considered lawful for marriage. Thereafter there are comparative references of conversions within the British and American contexts so as to ascertain whether the South African context of Islamic conversion, through the initiation of marriage, is mirrored in other countries and cultures.

Chapter four will cover the research analysis and findings which will be observed in terms of the models discussed in chapter two. The aim of the analysis would be to answer some imperative questions. Do the women who convert to Islam for marriage do so without compulsion as they state at the conversion ritual, or do they feel compelled because of overriding pressures and influence? What are the effects they experience because of the conversion process? Has the conversion been a positive step in their lives? Did they get support or advice from an Islamic organization? Do they think that a support group would be beneficial for women such as themselves? What advice would they offer to other women who are considering converting for the purpose of marriage? Do they feel accepted by the social community? In addition, the outcome of the findings would be set against the framework of the models looking at criteria such as: the age of conversion,

turbine inlet temperature (TIT), governed by the efficiency equation of the ideal Brayton cycle (Cengel and Boles (2001)), and by the use of lighter and stronger materials that can operate close to their thermal limits. These limits would define the operating temperature of the components within the turbine blade set, chiefly the stator vanes, which are right after the combustion chamber, known as nozzle guide vanes. Such components would need to perform and survive for lengthy periods of operation above their melting point to maintain a high TIT and efficiency. Thus, cooling is an important area of research, together with an accurate prediction of heat transfer coefficients of the turbine blades to gauge and monitor the life of the blades to prevent any catastrophic failure of components (Han *et al.* (2000)).

Internal cooling techniques involve using bypassed air at a relatively cold temperature, running through hollow passages inside the turbine, as shown in Figure 1-2. There have been further studies to implement external cooling techniques, such as 'film cooling', which basically involves using the bypassed air being fed out through small holes at discrete locations along the turbine blade, as described by Han *et al.* (2000). This forces a 'blanket' of relatively cold air around the turbine blade, which serves as a protective layer against the extremely hot-gas stream passing over it.

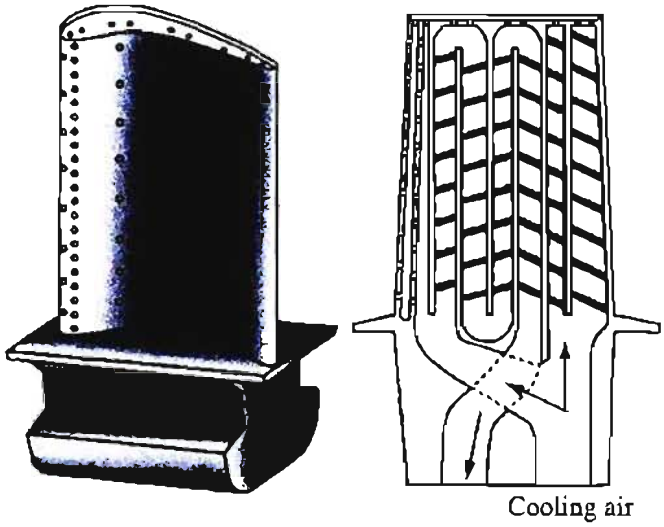

Figure 1-2: Examples of film cooling and internal cooling passages (reproduced from http://www.mmlab.mech.tuat.ac.jp/mmlab/research-e.htm)

The heat transfer to the turbine blades involves steady heat transfer, which is based on mean-flow conditions, including unsteady heat transfer, which is caused by various fluctuations in the main flow. This is contributed to by the combustor reactions, which generate freestream turbulence and shock waves from blade row interaction, as described by Hayashi *et al.* (1989).

Such turbulence levels would affect the heat transfer coefficients on the blades, and would need to be taken into account if they are to be accurately predicted (Holden (1972)).

One of the methods of predicting the behaviour of heat transfer over a turbine blade is to use computational fluid dynamics (CFD). This method allows a large amount of money to be saved with regards to experimental equipment and testing, but must be used correctly in order to determine accurate results that would give a fair guideline on what would be expected in the application. Although a much cheaper and effective way of prediction compared to real-life testing, experimental results must be sought in order to judge and validate the true accuracy of the computational model and results. Once the simulation result is confirmed to be reliable and of the general trend compared to the experimental test, then the computational model could be safely used for other situations and conditions that would be difficult to implement quickly and cheaply with experimental equipment.

The work in this dissertation describes the experimental evaluation of heat transfer across an SMR-95 high turning angle turbine blade. This was attained using the continuously running supersonic cascade facility at the University of KwaZulu-Natal (UKZN). The experimental rig runs under vacuum pressure, and a plunging device implemented by Snedden (1995) was used to plunge the blade into the relatively hot-air stream. Turbulence intensity-generating grids were implemented to gauge the effects of turbulence on the heat transfer of the blade. These results were generated to verify previous work performed on the rig, using the same techniques and procedures and to establish the current working condition of the experimental facility.

Further research was conducted to investigate alternate heat transfer measurement techniques to replace the analogue circuitry with a simpler numerical model. A numerical analysis of the heat transfer was achieved using the computer program FLUENT, a popular CFD package and readily available at UKZN. The geometry for the model was created using the pre-processor GAMBIT. The data achieved from the analysis was compared to the experimental results, and previous results attained by preceding students who worked on the project.

CHAPTER 2

LITERATURE SURVEY

2.1 OVERVIEW

Ever since its serious inception into industrial applications and as transportation powerplants in the late 1930s, extensive research has been done into improving the efficiency and power of gas turbine engines, as well as continuous development of predicting heat transfer over turbine blades. There are decades of existing literature which describe developments of test facilities and various methods of simulating the localised environment of a turbine blade in an operating gas turbine engine. From the many different facilities, there are a number of diverse methods of acquiring the heat transfer data, each with its own advantages and disadvantages, best suited to its application of intention. By looking to increase the TIT and resulting increase of power, extensive and thorough research has been done to improve cooling methods, and to investigate other phenomena that would cause any drop in efficiency. Such developments and techniques were reviewed, as well as the various testing facilities and methods to acquire heat transfer coefficients. There have also been advancements in numerical predictions and CFD codes, which were also investigated. Previous literature surveys investigated by Cassie (2006) and De Villiers (2002) proved to be helpful, and this chapter is a summary of their investigations together with further studies of existing literature and new developments.

2.2 EXPERIMENTAL FACILITIES

2.2.1 INTRODUCTION

At various institutions around the world, there have been a few different methods of simulating the operating environment and aerodynamics of a rotor turbine blade and investigating any resulting heat transfer. The basic goal to achieve this is to have a scaled test blade at a certain temperature exposed to a hotter air stream flowing over it. By using a suitable data acquisition technique, the temperature difference and heat transfer can be measured, and then converted to heat flux for analysis and ultimately the calculation of the heat transfer coefficients along the span of the blade. Certain aspects that represent real world conditions as accurately and realistically as possible, such as Mach numbers, Reynolds numbers, and turbulence effects need to be taken into account. Such facilities and data acquisition will be discussed.

2.2.2 Shock Tube Facilities

The shock tube method uses shock waves to compress and heat the gas, and this high pressure gas is passed rapidly through the test section. The shock wave is produced by a quick discharge of a driver gas at high velocity of either nitrogen or helium in one tube, and a driven gas at a low pressure (usually air) in another tube. The tubes are separated by a diaphragm, which bursts at a selected time, causing a shock wave due to the pressure difference between the gases in both tubes. The shock wave proliferates through the lower pressure test gas, and then reflects off the end of the shock tube. This creates an area of almost gas which is of high pressure and temperature, and expanded through a converging diverging nozzle to create a constant mass flow through the test section. This method only works for a very short duration, however, as the facility would make use of the flow behind the shockwave.

Other variations of shock tube facilities include the 'gun tunnel'. This facility consists of two tubes, namely a driver tube and a driven tube, otherwise referred to as the barrel. This is separated from the converging diverging nozzle by valves. A piston is placed at the position of the driver chamber and the barrel. The piston is propelled down the barrel to force gas through the nozzle. As the gas passes through the divergence in the nozzle, it expands and accelerates rapidly over a short distance. Since only a limited amount of gas is expanded through the nozzle, the stagnation conditions do not last long and the duration of the test is relatively short.

Figure 2-1: Experimental setup of a gun tunnel (reproduced from http://www3.imperial.ac.uk/hypersonics/facilities/mach9hypersonicguntunnel)

2.2.3 LIGHT PISTON COMPRESSION TUNNELS

Light piston compression tunnels work in a similar fashion to shock tube facilities. The idea is unchanged in that it achieves a sudden step change in temperature and resulting heat flux. The operating conditions are achieved by compressing air isentropically using a light piston. The air is compressed against a shutter valve, and once the correct pressure and temperature levels have been reached, the valve opens and releases the high-temperature and high-pressure air over the relatively cold blade cascade.

A sonic throat is located just after the test section, before the dump tank, to create a constant mass flow through the test section. The purpose of the dump tank is to allow for varying of the Mach number by adjusting the pressure. An example of such a facility is the CT-3 rig at the Von Karman Institute (VKI) in Belgium (as shown in Figure 2-2). The test duration of such facilities ranges between 0.2 – 0.4 seconds. During blow-down, the acceleration of the rotating parts is limited by an inertia wheel. Further details of operation are given on the VKI website (http://www.vki.ac.be/).

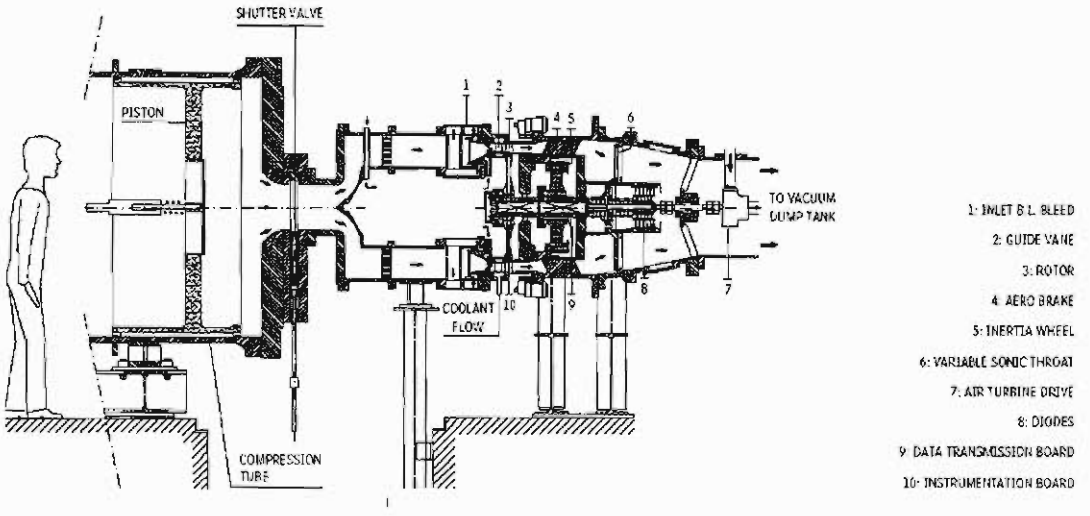

Figure 2-2: CT-3 Isentropic Compression Tube Facility (reproduced from http://www.vki.ac.be/facilities/index.html)

A disadvantage with regard to light piston compression tunnels is the transient establishment of the flow through the test section. An unsteady supersonic flow develops before it reaches steady state as the test section is under vacuum pressure before the shutter valve is opened. This facility would also need a large storage area. An advantage, however, would be that the running costs would be relatively low compared to other types of facilities. Such compression tunnels have been used for research by Jones and Launder (1973) and Consigny and Richards (1982).

2.2.4 CONTINUOUSLY RUNNING FACILITIES

The problem of needing relatively large storage volumes for the previous methods is addressed with continuously running facilities. This method involves having a constant stream of hot air flowing over the test blades. Such a facility was used at UKZN and the work presented in this dissertation was performed on the same experimental rig.

The facility operates under vacuum pressure and the air is recirculated within the plenum via a centrifugal compressor. The Reynolds number and Mach number are set by adjusting the speed of the compressor. The air that circulates inside the plenum is relatively hot and is constantly flowing over the turbine test blade in the cascade. For there to be a temperature difference to calculate resulting heat flux and heat transfer coefficients, the test blade is extended into a cooling box, with the bottom of the blade being the 'dummy' section exposed to the hot air while the section with thin-film gauges is being cooled. The air in the plenum runs through a circular radiator, and thus the temperature of the air is controlled by adjusting the flow of water through the radiator. Once the correct temperatures and pressures have been reached, a pneumatically operated device replaces the dummy blade with the instrumented blade by rapidly plunging it down into the hot-air stream. This ensures that the flow over the blade is not disrupted.

Van der Steege (1990) initially designed and used the test facility to assess the performance of turbine blades with cooling. It was then used by McDonald (1994) for the study of tip clearance effects on turbine endwalls. Snedden (1995) began the implementation of heat transfer measurement and testing by putting into operation thin-film gauge instrumentation on the blade, the data acquisition system required for analysis and post-processing of data. Stieger (1998) investigated various aerodynamic discrepancies in the turbine blade flow by creating various turbulence intensities using grids, and tripping the flow using wires at specific points on the span of the blade. He also performed flow visualisation tests to show the aerodynamic effects occurring on the test blade. De Villiers (2002) verified the previous heat transfer measurements, and conducted analyses using FLUENT to generate numerical predictions with a CFD package. Cassie (2006) was involved in restoring the experimental rig to operating order, and looked to implement film-cooling techniques, as well as generating heat transfer data with a newly instrumented test blade.

Some of the other continuously running facilities were used by Reiss, Bölcs and Drost (1998) at the University of Limerick in Ireland, and Graziani *et al.* (1980), who used a low-speed, open-circuit wind tunnel to generate endwall and airfoil surface heat transfer data.

2.3 Heat Transfer Measurement Techniques

2.3.1 Introduction

There are numerous instrumentation techniques that are capable of reading the temperature change in a heat transfer test, from which the data is used to convert to heat flux and resulting heat transfer coefficients. Some methods have been more popular than others, and the ultimate decision to implement a technique is based on the size and suitability of the test section and the facility of housing.

2.3.2 Naphthalene Sublimation

The naphthalene sublimation technique is one of the most convenient mass transfer methods to determine local heat transfer coefficients by using the heat and mass transfer analogy. The application of naphthalene onto the blade can be performed using a variety of ways including casting or spraying. Once the coating of naphthalene is applied to the blade, the initial thickness is noted. After an experiment is complete, the thickness of the naphthalene is measured and the difference between the initial and final thickness is recorded. Therefore, the rate of mass transfer per unit surface area is known, and the mass transfer coefficient can be calculated. This is expressed by the Sherwood number, which can be used to calculate the Nusselt number, thereby determining the local heat transfer coefficients. This is achieved with relatively high accuracy, and the technique is straightforward. The disadvantages of this technique is that new coats of naphthalene have to be applied for each measurement, and it cannot be used for high-speed flows due to the recovery temperature effects, as well as for natural convection due to thermal buoyancy effects of sublimation latent heat, as outlined by Goldstein and Cho (1995).

There have been further studies into different techniques to measure naphthalene thicknesses in order to improve accuracy on arbitrary shapes. One such method, using optics developed by Hong and Song (2007), is to illuminate a collimated laser light onto a glass substrate and a CCD camera detects the scattered light to measure the thickness before and after the sublimation process. Such techniques enable fast and accurate recordings of naphthalene thicknesses.

2.3.3 THERMOCHROMIC LIQUID CRYSTALS

The thermochromic liquid crystal (TLC) method involves monitoring the change of colour of a TLC-covered surface over a defined period. A change in temperature causes the TLCs to change colour, and this is monitored by a video camera. Disadvantages of this technique include the amount of data recorded by the video camera, and that a clear line of sight of the TLC-covered surface is needed. The advantages of this technique include a high spatial resolution, and that the change of colour process is completely reversible, unless for the case of damaged TLCs. This process has been used by Stasiek and Kowalewski (2002) and Reiss, Bölcs and Drost (1998). The change of colour for a heat flux step change is shown in steps in Figure 2-3 below.

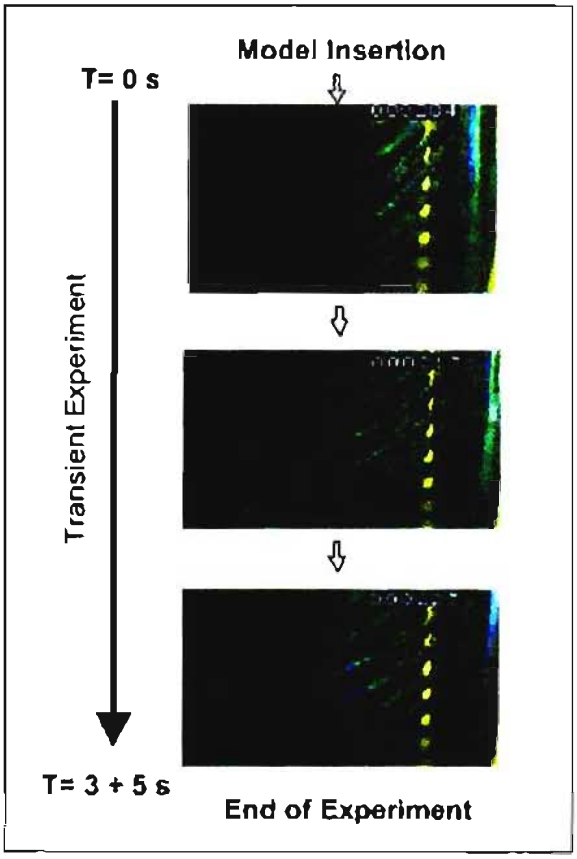

Figure 2-3: Colour changes of TLCs due to temperature change
(reproduced from Reiss *et al.* (1998))

the gauges, calibration methodology and signal processing. This will be discussed further in Chapter 3. The basic operation of a TFG is that if a constant current is applied to the TFG, any surface temperature change would result in a proportional voltage change across the gauge in question. The paint to provide connectivity from the surface of the blade to the wire leads was gold paint. The purpose of the gold paint was that the air flow remained undisturbed, as well as its attribute of low resistance relative to the platinum gauge. Because of this attribute, one can neglect the resistive element of the gold paint, and assume the resistance changes occur only across the platinum gauge. The resulting voltage change from the resistance is converted to heat flux by electrical analogue circuit boards. These are constructed with resistors and capacitors arranged to produce voltages and currents analogous to heat flux and temperature. The output voltage would therefore be heat flux. The design of the electrical analogue boards to convert the voltage reading to heat flux was developed by Oldfield *et al.* (1978), and implemented at UKZN by Snedden (1995). This implementation was successful and the results presented in this dissertation use the thin-film gauge technique.

The main advantage of TFGs is that the heat flux can be measured directly, as opposed to the other techniques discussed, which calculate heat flux indirectly (for example, heat flux with naphthalene sublimation must be calculated via a mass transfer reading). The other advantage of TFGs and measuring the heat flux directly is that for the surface temperature reconstruction from heat flux, an integration process is needed. This is a noise-reducing operation with regard to numerical calculations, as opposed to the differential calculations needed if the surface temperature were measured directly and then the heat flux calculated, which would be noise generating. Numerical post-processing techniques will be discussed further in Section 2.3.6.

Hand-painted gauges can be prone to irregularities in surface area and thickness, and the resulting total resistance. Snedden (1995) painted platinum gauges of 1mm wide and 10 mm long. These were painted onto the Macor substrate and fired and separately baked in an oven. Extreme caution and attention to detail are required during the gauge construction. The details on the method of construction will be discussed in Section 5.3.2.

2.3.6 Numerical Post-Processing Techniques

There are a number of numerical heat transfer measurement techniques that can be used, depending on the suitability and compatibility of the experimental facility being used, which will be discussed quite briefly. Bezuidenhout (2000) looked at the Cook-Felderman (1996) technique, which uses a derivation of an analytical equation to calculate heat flux, and thus a

noise-generating method. By using various filters, results were achieved, but it was believed that the trend of the original trace would be altered after passing through the numerous smoothing filters. Bezuidenhout proposed the use of the Walker (1997) method. This would be a true inverse approach, as it makes use of boundary conditions at the "back" surface, i.e. temperature, heat flux, semi-infinite solid. The Walker method was found to be more stable than the Cook-Felderman technique, because the derivative of the temperature distribution is not taken. The method is statistical in nature, which means effects of noise on the data can be reduced by use of an iterative process of the flux at the surface. This method, however, would require the measurement of temperature at the "back" surface of the blade, which would require a total reconstruction and design of the current SMR-95 blade in the experimental facility at UKZN, which is only on a small enough scale to measure the temperature at the surface.

A review of heat transfer measurement techniques by Dénos (1996) proved to be helpful. The Fourier Transform, which can be used to convert surface temperature history to flux history, was looked at as well as the Crank-Nicholson scheme. A transform is performed on the time signal T(t) resulting in an equivalent series in the frequency domain T(ω). A complex product is performed with the complex transfer function H(*j*ω) giving the flux solution in the complex domain. An inverse transform then provides the flux in the time domain (Dénos (1996)). The advantage of the Fourier transform is its ability to fit any transfer function, however, there are problems of transient response at the end of the signal after the extensive calculations. The temperature profile inside the medium is obtained and the flux at the wall is derived from the derivative of the temperature profile at the wall using the Crank-Nicholson scheme. This method uses the following equation:

$$\frac{T_i^{n+1} - T_i^n}{\Delta t} = \alpha \frac{\left[\eta\left(T_{i+1}^{n+1} - 2T_{i+1}^{n+1}\right) + (1-\eta)\left(T_{i+1}^n - 2T_i^n + T_{i-1}^n\right)\right]}{\Delta x^2} \qquad (2.6.3.1)$$

where η is a parameter defining the contribution of terms at time (n+1) and at time n in the different terms, i is the index for the depth in the substrate. If all terms at time (n+1) are brought onto the left-hand side, all terms on the right are known. In this form, the tridiagonal matrix can be solved with various algorithms. Dénos (1996) compared this method to experimental data and the results compared favourably. The Crank-Nicholson scheme was noted to be much faster than the Cook-Felderman technique for larger time series. This scheme would be the most favourable to replace the analogue circuits currently at the UKZN test facility with reasonable accuracy after numerical smoothing.

2.3.7 Effects of Turbulence Intensity

Various research papers concentrated on the effects of heat transfer coefficients as a result of different turbulence intensities applied. Gratton (2004) at the Virginia Polytechnic Institute and State University undertook extensive research with regard to turbulence intensities. To simulate an engine-representative pressure distribution, with accelerated flow on the suction side, Gratton (2004) made use of a contoured endwall designed in the CFD program FLUENT. This significantly accelerated the flow and increased the heat transfer by 40%. Trip wires were used to simulate boundary layer perturbation caused by coolant injection, as would be the case if the blade were film cooled. Such studies have not been conducted at UKZN. Turbulence intensity-generating grids were used to observe the resulting effects on the heat transfer coefficients, and similarly to the results obtained by Nix (2003) of the same university, there was a general increase of the heat transfer coefficients along the blade profile. With a turbulence intensity of 10%, the increase in heat transfer was 17% on the pressure side, and 8% on the suction side, for a blade geometry of a high turning, generic GE first-stage rotor blade. Little or no information could be found regarding heat transfer tests using the specific SMR-95 blade geometry internationally. Previous tests and results performed at UKZN, including further tests by Snedden (1995) at the CSIR (1998), are directly discussed and compared to the author's work in Chapter 5.

Turbulence intensity studies were performed at UKZN by Stieger (1998), using turbulence-generating grids which resulted in 15% and 25.5% turbulence intensities. Various phenomena were observed at the base condition (no grids, 3% intensity) including separation bubbles formed close to the leading edge on both the pressure and suction sides. With the implementation of the turbulence-generating grids, the overall heat transfer was increased, and a more local observation showed that there was no indication of the separation bubble forming near the trailing edge, which occurred at 3% intensity.

This method of turbulence generation proved favourable, as was used similarly by Radomsky and Thole (1998), Boyle *et al.* (1998), and Polanka and Bogard (1999) to generate high levels of turbulence, which ranged between 10% and 20% by using parallel bars placed upstream. No turbulence intensity investigations have been performed since Stieger (1998).

2.4 NUMERICAL PREDICTION

Numerical prediction currently available serves more as a guideline to heat transfer measurements and flow characteristics than as a replacement for experimental tests. Although financially extremely feasible compared to experimental facilities, there is no numerical code that can accurately predict the complex flow patterns and heat transfer over a turbine blade. Basic tests can be run on both experimental and numerical, and compared to judge the accuracy, before moving on to more complex tests.

With the current processing power of computers of today, however, computational fluid dynamics (CFD) has provided a greater insight into the understanding of flow fields in the localised area of turbine blades in jet engines, including faster processing times compared to older technology where it would take painstakingly long periods of time to number-crunch the complex algorithms of numerical models.

Over the years, there have been two basic methods to model the flow and heat transfer characteristics on turbine blades. These methods are boundary layer codes and full Navier-Stokes solvers. The boundary layer codes would give a general and quick analysis of the flow field in the boundary layers over surfaces, however, extra information regarding the main flow stream must be specified. The full Navier-Stokes code will be able to compute and solve the entire flow field with special revisions applied to the near-wall regions.

Prandtl developed the boundary layer by simplifying the full set of Navier-Stokes equations by using an order of magnitude reduction technique. These equations are only local to boundary layers, and the main flow field needs to be solved via other methods. Prandtl proposed that the boundary layer zone was subject to viscous effects, whereas these effects could be neglected in the main flow region. This inviscid region can be solved by using Euler's equations, which use the momentum and energy equations, neglecting the viscosity terms. This method is thus solved in series, with the results for one set used as boundary conditions for the other set of equations.

STAN 5 is a popular two-dimensional boundary layer code that was developed by Crawford and Kays (1976) at Stanford University. General use of these codes proved that there usually was over-prediction, as discussed by Graziani *et al.* (1980). This over-prediction was a probable result of the flow field not being resolved accurately enough. One of the main reasons is due to finding the correct use of turbulence model. The most common models are the two-equation turbulence models of standard k-ε, two-layer k-ε and the $k-\omega$. One-equation models include

the Baldwin-Lomax model and, more popularly, the Spalart-Allmaras model. Wang *et al.* (1985) incorporated the low Reynolds number version of the k-ε model into the STAN 5 code, and compared the numerical prediction results to experimental data of the same turbine blade profile. Although there was some over-prediction at the leading edge, the general trend for the heat transfer results proved to have a good correlation with the experimental data. Thus this relatively accurate method of simulating transitional flow came to be popularly used.

The other main technique of modelling flow field characteristics and heat transfer in CFD is by using the full set of Navier-Stokes solvers, which are capable of solving the main flow field as well as applying special adaptations to the near-wall region (boundary layer). The equations use different approaches with regard to the representation of turbulence. The Reynolds-averaged Navier-Stokes (RANS) equation approach transforms the Navier-Stokes equations to represent transport equations for the time-averaged solution. Thus new terms were introduced into the momentum equation, which were referred to as "Reynolds stresses". Thus the definition of turbulence and the Reynolds stresses were defined by models such as Reynolds stress model (RSM), k-ε, and k-ω.

The other method is large eddy simulations (LES) which analyses turbulence as space averaged at a fixed point in time. This solves relatively large-scale eddies/turbulence directly, and smaller-scale effects are solved using subgrid-scale stress models, similar to that of the RANS equations approach. The disadvantages of this approach are the lengthy computational times and large data storage space needed.

The commercially available CFD package of FLUENT was used to generate results presented in this dissertation. The program FLUENT is the solver and post-processor of the CFD process, while the pre-processing program of GAMBIT was used in conjunction. Geometry models were created in GAMBIT, as well as the creating and refining of meshes. The boundary surfaces were also set in GAMBIT, which could then be used to have boundary conditions readily set in FLUENT, including material properties and solver settings. FLUENT is capable of solving the inviscid and Navier-Stokes equations, as well as the RANS and LES approaches including the setting of various turbulence models.

CHAPTER 3

THEORY

3.1 OVERVIEW

To improve gas turbine engine efficiency and performance, a more thorough and better understanding is needed of heat transfer and the flow characteristics over a turbine blade to make improvements and monitor the life cycle of the blade.

To analyse the heat transfer on a turbine blade, the heat transfer coefficients must be calculated using the heat flux. At UKZN, the technique for extracting heat flux data from the temperature changes created by the operation of the experimental facility is thin-film gauges of platinum. This is painted onto a Macor substrate which is assumed to be semi-infinite. As discussed in Section 2.3.5, the advantage of extracting heat transfer data from thin-film gauge instrumentation is that an integration process is used, which is noise reducing. If the surface temperatures were being read, then a differential process would be needed to convert to heat flux data, which is a noise-generating process. The technique implemented at UKZN was the use of electrical analogue circuit boards to create a heat flux analogy, used by Ligrani *et al.* (1982), and implemented by Snedden (1995) and used to determine the results presented in this dissertation.

This chapter is to provide an extensive description of the heat transfer theory, and the defining equations behind the technique of thin-film gauges and the analogue cards for heat flux analogy. Ligrani *et al.* (1982) provided the theory of heat transfer measurements and calibration, as will be discussed, and Schultz and Jones (1973) provided the theory behind the electrical analogue circuit board operation that would be analogous to heat flux and temperature.

3.2 HEAT TRANSFER THEORY

3.2.1 HEAT FLUX THEORY

To define heat transfer on the turbine blade setup at the UKZN test facility, the Macor substrate on which the TFG was painted is assumed to be semi-infinite. This means that during a test the "back surface" is assumed to remain the same temperature as at initial conditions, to simplify,

that the thickness of the substrate should be large enough such that conductive heat transfer does not penetrate to the back surface. This one-dimensional heat transfer is represented as seen in Figure 3-1 below.

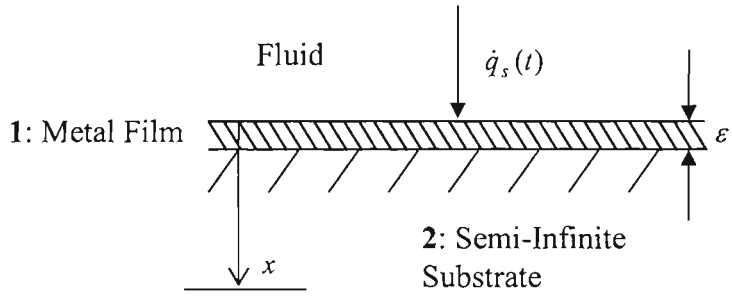

Figure 3-1: 1D heat conduction into a metallic film and semi-infinite ceramic substrate

The differential equations that describe the 1D heat transfer of the metallic TFG and the substrate are:

$$\frac{\partial^2\theta_1}{\partial x^2} = \frac{1}{\alpha_1}\frac{\partial\theta_1}{\partial t} \qquad (3.2.1.1)$$

$$\frac{\partial^2\theta_2}{\partial x^2} = \frac{1}{\alpha_2}\frac{\partial\theta_2}{\partial t} \qquad (3.2.1.2)$$

where θ represents the temperature change relative to the ambient temperature, $(T - T_\infty)$, at distance x and time t. The thermal diffusivity of the material is represented by α.

The following boundary conditions apply for 1D heat transfer:

$$-k_1\frac{\partial\theta_1}{\partial x} = \dot{q}_s \quad \text{at} \quad x = 0 \qquad (3.2.1.3)$$

$$k_1\frac{\partial\theta_1}{\partial x} = k_2\frac{\partial\theta_2}{\partial x} \text{ and } \theta_1 = \theta_2 \quad \text{at} \quad x = \varepsilon \qquad (3.2.1.4)$$

$$\theta_2 = 0 \quad \text{at} \quad x = \infty \qquad (3.2.1.5)$$

An assumption is made that the gauge temperature is uniform due to its relatively small area. It can also be assumed that the thickness of the TFG has a negligible effect on heat conduction,

since its thermal conductivity is relatively high. By letting $\varepsilon \to 0$ in the differential equations described, this leaves:

$$\frac{\partial^2 \theta_2}{\partial x^2} = \frac{1}{\alpha_2} \frac{\partial \theta_2}{\partial t} \qquad (3.2.1.6)$$

with the following boundary conditions applicable:

$$-k_2 \frac{\partial \theta_2}{\partial x} = \dot{q}_s \quad \text{at} \quad x = 0 \qquad (3.2.1.7)$$

$$\theta_2 = 0 \quad \text{at} \quad x = \infty \qquad (3.2.1.8)$$

and the initial condition that $\theta_2 = 0$ at $t = 0$ for all x (3.2.1.9)

By taking the Laplace transform of both sides of equation 3.2.1.6:

$$\bar{\theta}_s = \frac{1}{\sqrt{\rho C k}} \frac{\bar{q}_s}{\sqrt{s}} \qquad (3.2.1.10)$$

where the overbar denotes the Laplace transformation, with the Laplace variable represented by s, and the subscript 2 is dropped. By using the convolution theorem, the inverse transformation of $\bar{\theta}_s$ is obtained:

$$\theta_s = \frac{1}{\sqrt{\pi}\sqrt{\rho C k}} \int_0^t \frac{q_s(\tau)}{\sqrt{t-\tau}} dt \qquad (3.2.1.11)$$

Integrating this equation, for t > 0 and constant heat flux, gives:

$$\theta_s = \frac{2\dot{q}_s}{\sqrt{\pi}} \sqrt{\frac{t}{\rho C k}} \qquad (3.2.1.12)$$

By simple rearranging, the heat flux can be expressed as:

$$\dot{q}_s = \frac{\sqrt{\pi}}{2} \sqrt{\frac{\rho C k}{t}} \theta_s \qquad (3.2.1.13)$$

Thin-film gauge resistance, varying with temperature, is given by:

$$R = R_0(1 + \alpha_R(T - T_0)) \tag{3.2.1.14}$$

where R is the thin-film resistance at surface temperature T, R_0 is the thin-film resistance at temperature T_0, and α_R is the film temperature coefficient of resistance. By applying a constant current, simple manipulation via Ohm's law ($V = I \times R$), the equation becomes:

$$V = V_0(1 + \alpha_R(T - T_0)) \tag{3.2.1.15}$$

Before an experimental test, if the initial voltage V_0 is measured at the initial temperature T_0, then $T_\infty = T_0$ and

$$\theta_s = \frac{\Delta V}{\alpha_R V_0} \tag{3.2.1.16}$$

where ΔV is the change in the thin-film output voltage with reference to the initial voltage V_0. By substituting into equation 3.2.1.13, the surface heat flux can be represented in terms of the output voltage as:

$$\dot{q}_s = \sqrt{\frac{\rho C k}{t}} \frac{\sqrt{\pi}}{2} \frac{\Delta V}{\alpha_R V_0} \tag{3.2.1.17}$$

The temperature resistance coefficient α_R is calibrated for each thin-film gauge before testing. By simple rearrangement of equation 3.2.1.14:

$$\alpha_R = \frac{1}{R_0}\left(\frac{R - R_0}{T - T_0}\right) \tag{3.2.1.18}$$

The value of $\left(\frac{R - R_0}{T - T_0}\right)$ is found by varying the temperatures that a gauge is exposed to, and recording the associated resistance values. The graph of R *vs* T yields a straight line graph, of which the gradient is $\left(\frac{R - R_0}{T - T_0}\right)$. R_0 is found by measuring the resistance of the TFG at the point just before input to the analogue circuit board. The full calibration procedure is given in Section 5.3.3 of Chapter 5.

3.2.2 ELECTRICAL ANALOGUE THEORY

By using the analogue circuit boards, the heat flux calculations are noise reducing, as discussed previously. The circuit boards are made up of capacitors and resistors that allow it to be directly analogous to thermal heat flux.

The transient heat conduction equation is given by:

$$\frac{\partial^2 T}{\partial x^2} = \frac{\rho C}{k}\frac{\partial T}{\partial t} \tag{3.2.2.1}$$

and the transmission line equation is given by:

$$\frac{\partial^2 V}{\partial x^2} = r'c'\frac{\partial V}{\partial t} \tag{3.2.2.2}$$

The derivation of these equations is given by Schultz and Jones (1973) and is shown in Appendix D1.1.

Taking Laplace transform of equation 3.2.2.2 yields:

$$\frac{\partial^2 \overline{V}}{\partial x^2} = r'c's[\overline{V} + V(t=\infty) - V(t=0)] \tag{3.2.2.3}$$

where $V(t=\infty)=0$.

The following boundary conditions are applied:

$$\overline{V} = 0 \qquad \text{at} \qquad t = 0 \tag{3.2.2.4}$$

$$\overline{V} = 0 \qquad \text{at} \qquad x = \infty \tag{3.2.2.5}$$

$$-\frac{1}{r'}\frac{\partial \overline{V}}{\partial x} = \overline{i}_{in} \qquad \text{at} \qquad x = 0 \tag{3.2.2.6}$$

By applying the initial conditions, equation 3.2.2.3 becomes:

$$\overline{V} = A\exp(x\sqrt{r'c's}) + B\exp(-x\sqrt{r'c's}) \tag{3.2.2.7}$$

where A and B are constants. By applying the boundary conditions,

$$A = 0 \tag{3.2.2.8}$$

$$B = \bar{i}_{in}\sqrt{\frac{r'}{c'}}\frac{1}{\sqrt{s}} \tag{3.2.2.9}$$

Thus, when $x = 0$, equation 3.2.2.7 can be expressed as:

$$\Delta\bar{V} = \bar{i}_{in}\sqrt{\frac{r'}{c'}}\frac{1}{\sqrt{s}} \tag{3.2.2.10}$$

Since the circuit input is the thin-film output,

$$\Delta\bar{V} = \alpha_R V_0 \bar{\theta}_s \tag{3.2.2.11}$$

Substituting this into 3.2.2.10 and gives:

$$\bar{i}_{in} = \sqrt{\frac{sc'}{r'}}\alpha_R V_0 \bar{\theta}_s \tag{3.2.2.12}$$

Equation 3.2.1.10 is the heat conduction equation that is analogous to 3.2.2.10:

$$\bar{q}_s = \sqrt{\rho Ck}\sqrt{s}\bar{\theta}_s \tag{3.2.2.13}$$

Substituting for $\bar{\theta}_s$ yields

$$\bar{q}_s = \sqrt{\rho Ck}\sqrt{\frac{r'}{c'}}\frac{1}{\alpha_R V_0}\bar{i}_{in} \tag{3.2.2.14}$$

The analogue circuits designed by Oldfield *et al.* (1985) made use of a current to voltage converter. This has an output voltage which is directly proportional to the current supplied, and by using a proportionality constant, κ, the equation of $V_{out} = \kappa i$ is substituted into equation 3.2.2.14 and becomes:

$$\bar{q}_s = \sqrt{\rho Ck}\sqrt{\frac{r'}{c'}}\frac{1}{\alpha_R V_0}\frac{V_{out}}{\kappa} \tag{3.2.2.15}$$

The values for the surface heat flux $\dot{q}_s$, from equations 3.2.1.17 and 3.2.2.15 must be equal if $\dot{q}_s$ is constant, for $t > 0$ and if $T_\infty = T_0$. Therefore:

$$\bar{\dot{q}}_s = \sqrt{\rho C k}\sqrt{\frac{r'}{c'}}\frac{1}{\alpha_R V_0}\frac{V_{out}}{\kappa} = \sqrt{\frac{\rho C k}{t}}\frac{\sqrt{\pi}}{2}\frac{\Delta V}{\alpha_R V_0} \qquad (3.2.2.16)$$

The calibration constant for the analogue time can be defined by rearranging into:

$$\frac{A^*}{\beta} = \frac{\bar{\dot{q}}_s \alpha_R V_0}{\sqrt{\rho c k} V_{out}} = \sqrt{\frac{r'}{c'}}\frac{1}{\kappa} = \frac{\Delta V}{2V_{out}}\sqrt{\frac{\pi}{t}} \qquad (3.2.2.17)$$

Although this term contains the period t, it is however still constant, as the ratio $\frac{\Delta V}{\sqrt{t}}$ is constant with a parabolic signal. To calibrate the circuit boards, a parabolic signal is fed into the system, which generates a step output voltage. This can be seen in Figures 3-2 and 3-3.

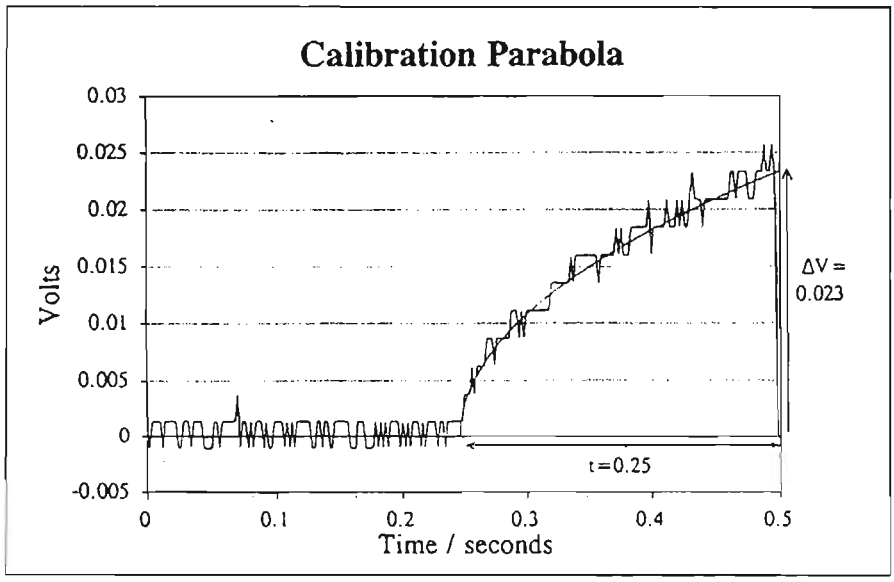

Figure 3-2: Parabola voltage signal to calibrate electrical analogue circuit boards (reproduced from Snedden (1995))

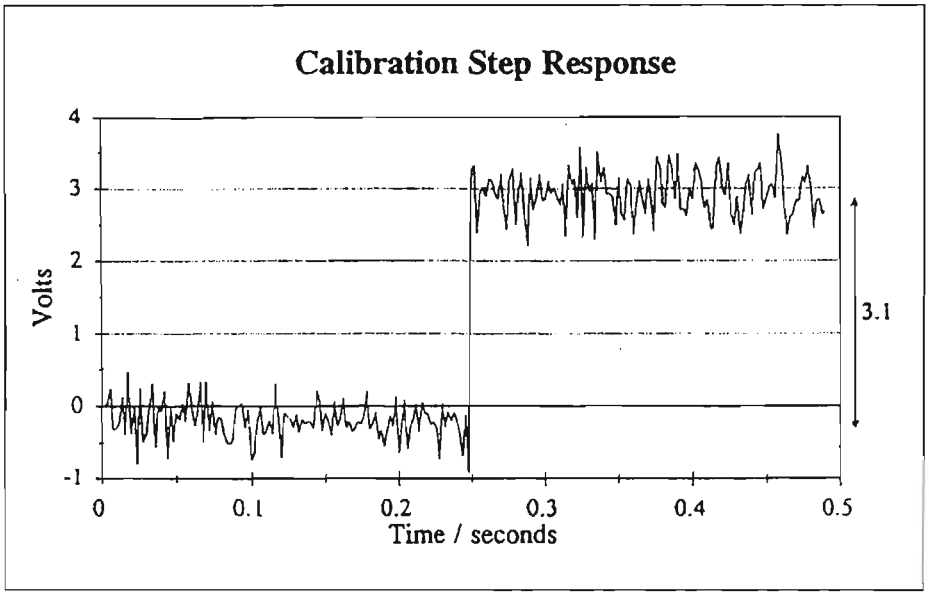

Figure 3-3: Step output from electrical analogue circuit boards as result of an input parabola voltage (reproduced from Snedden (1995))

From equation 3.2.2.17, the heat flux can be calculated in terms of the gauge and analogue circuitry as:

$$\dot{q}_s = \frac{V_{out}}{V_0}\frac{\sqrt{\rho C k}}{\alpha_R}\frac{A^*}{\beta} \qquad (3.2.2.18)$$

If V_0 is not measured at T_0 but at T_∞, an additional term compensates for this possibility, as given by:

$$\dot{q}_s = \frac{V_{out}}{V_0}\frac{\sqrt{\rho C k}}{\alpha_R}\frac{A^*}{\beta}(1+\alpha_R(T_\infty - T_0)) \qquad (3.2.2.19)$$

3.2.3 Surface Temperature Reconstruction

The acquisition and calculation of the heat transfer coefficient are performed from the reconstruction of the surface temperature from the heat flux. Schultz and Jones (1973) first worked out the details of this solution, with Ligrani *et al.* (1982) providing much more detail.

If one assumes that the analogue signal for surface heat flux has been converted to a series of digital data points, any data point at a given time t can be represented as:

$$\dot{q}_s(t) = \sum_n H(t - t_n).a_n(t - t_n) \tag{3.2.3.1}$$

Where $H(t - t_n) = 1$ for $t \geq t_n$, and is equal to 0 for all else, and:

$$a_n = \frac{\dot{q}_{n+1} + \dot{q}_{n-1} - 2\dot{q}_n}{\Delta\tau} \tag{3.2.3.2}$$

To calculate the heat flux at a time t_x with a total of m data points:

$$\begin{aligned}
\therefore \dot{q}_s(t_x) &= \sum_{n=1}^{m} H(t_x - t_n).a_n(t_x - t_n) \\
&= H(t_x - t_1).a_1(t_x - t_1) + H(t_x - t_2).a_2(t_x - t_2) + \ldots \\
&\quad \ldots + H(t_x - t_{x-1}).a_{x-1}(t_x - t_{x-1}) + H(t_x - t_x).a_x(t_x - t_x) + \\
&\quad + H(t_x - t_{x+1}).a_{x+1}(t_x - t_{x+1}) + \ldots + H(t_x - t_m).a_m(t_x - t_m) \\
\therefore \dot{q}_s(t_x) &= \sum_{n=1}^{x-1} a_n(t_x - t_n)
\end{aligned} \tag{3.2.3.3}$$

Similarly,

$$\dot{q}_s(m) = (m-1)\dot{q}_0 - m\dot{q}_1 + \dot{q}_m \tag{3.2.3.4}$$

Therefore, the function will follow the actual data points of the signal exactly, if the first two data points in the series are forced to be zero. Taking a single element from equation 3.2.3.1,

$$\dot{q}_n = H.a_n(t - t_n) \tag{3.2.3.5}$$

which can also be expressed as:

$$\dot{q}_n = \int_{t_n}^{t} H.a_n d\tau \tag{3.2.3.6}$$

Using the convolution theorem to transform the equation, by letting $f(t-u)=1$ and $g(u)=H$, $F(s)=\frac{1}{s}$ and $G(s)=\frac{e^{-t_n s}}{s}$, the resulting transformation is

$$\bar{\dot{q}}_n = a_n e^{-t_n s} s^{-2} \tag{3.2.3.7}$$

As the sum of Laplace-transformed terms is equal to the Laplace transform of the sum,

$$\bar{\dot{q}}_n = \sum_n a_n e^{-t_n s} s^{-2} \tag{3.2.3.8}$$

This is substituted into equation 3.2.1.10:

$$\bar{\theta}_s = \frac{1}{\sqrt{\rho c k}} \sum_n a_n e^{-t_n s} s^{-5/2} \tag{3.2.3.9}$$

By using the convolution theorem again, this is inverted by making $F(s)=s^{-3/2}$ and $G(s)=\frac{e^{-t_n s}}{s}$, then $f(t)=2\sqrt{t/\pi}$ and $g(t)=H(t-t_n)$, resulting as:

$$h(t) = \int_0^t H(\tau - t_n) \frac{2}{\sqrt{\pi}} .(\tau - t_n)^{1/2} d\tau \tag{3.2.3.10}$$

By simple integration,

$$h(t) = \frac{4}{3\sqrt{\pi}} H(t-t_n).(t-t_n)^{3/2} \tag{3.2.3.11}$$

Substituting back into equation 3.2.3.9:

$$\theta_s = \frac{4}{3\sqrt{\rho c k \pi}} \sum_n a_n H(t - t_n).(t - t_n)^{3/2} \qquad (3.2.3.12)$$

And substituting for a_n,

$$\theta_s = \frac{4}{3\sqrt{\rho c k \pi}} \sum_n \left(\frac{\dot{q}_{n+1} + \dot{q}_{n-1} - 2\dot{q}_n}{\Delta\tau} \right) H(t - t_n).(t - t_n)^{3/2} \qquad (3.2.3.13)$$

and finally removing $\Delta\tau$ and $H(t - t_n)$ from the summation, the final expression used to calculate the surface temperature from the heat flux is as follows:

$$\theta_s(m.\Delta\tau) = \frac{4\sqrt{\Delta\tau}}{3\sqrt{\rho c k \pi}} \sum_{n=1}^{m-1} (\dot{q}_{n+1} + \dot{q}_{n-1} - 2\dot{q}_n).(m - n)^{3/2} \qquad (3.2.3.14)$$

CHAPTER 4

EXPERIMENTAL APPARATUS

4.1 OVERVIEW

Currently at UKZN, the facility to acquire heat transfer research is a continuously running supersonic cascade rig. Van der Steege (1990) initially designed and used the test facility to assess the performance of turbine blades with cooling. Snedden (1995) began the implementation of heat transfer measurement and testing by putting into operation thin-film gauge instrumentation on the blade, the data acquisition system required for analysis and post-processing of data.

This chapter serves to describe the various components of the rig and their respective functions.

4.2 HIGH SPEED RIG

4.2.1 INTRODUCTION

A hot-air stream is constantly run through the four-blade cascade, contained in a cylindrical plenum, of which one of the blades is instrumented to acquire heat transfer data. This air stream is circulated by a centrifugal compressor, which is driven by a hydraulic motor.

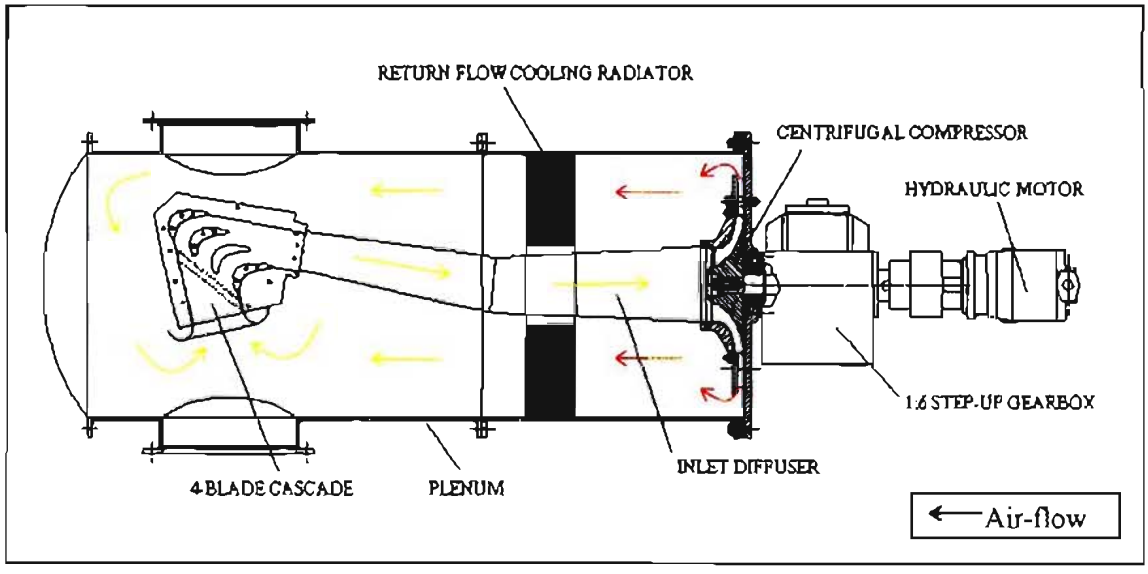

Figure 4-1: Supersonic cascade facility (top view, reproduced from De Villiers (2002))

As can be seen in Figure 4-1, the circulation of air begins by the drawing of air through a bell-mouth of the cascade by the centrifugal compressor, passes through the cascade, and then finally the air is pushed out back into the plenum. This air is constantly recirculated through these stages. Since the flow of air through the compressor causes an increase in temperature (hot-air stream), a temperature-regulating system of an annular radiator was fitted. By controlling the flow rate of the cooling water passing through the radiator, one is able to control the temperature of the air stream inside the plenum.

Once the correct temperatures and pressures have been reached, a pneumatically operated device replaces a dummy test blade with the instrumented blade (housed in a cooling box) by rapidly plunging it down into the hot-air stream. This causes a temperature difference and voltage step change with the heat flux analogue equipment, which can be analysed and used to calculate the heat transfer coefficients of the blade.

4.2.2 PLENUM

The plenum is a cylindrical chamber of dimensions 1.55 m in length, and 0.6 m in diameter, which houses the centrifugal compressor, four-blade cascade and annular radiator, as shown in Figure 4-2. The plenum can be accessed on either side, and it is split down the middle as well for access to the annular radiator. The back of the plenum contains access to the mechanical carbon seal, which allows the compressor shaft to go into the plenum.

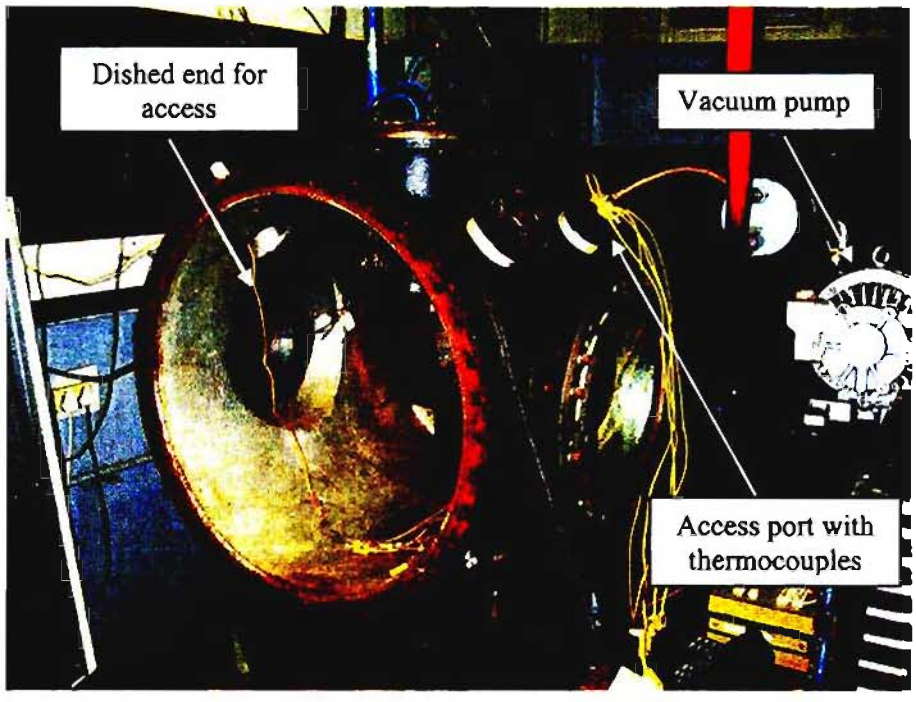

Figure 4-2: Outer view of the plenum

The most common area used to access the cascade is at the dished end to make the adjustments for heat transfer readings or pressure readings. All these access points contain a large gasket to ensure that when tightened, the plenum is airtight and can reach its required vacuum pressure easily. There are four sight glass portals that allow one to view and monitor the inside of the plenum once it has been closed and sealed. There are also four access ports that allow certain measurement cables and leads to pass out the plenum, such as thermocouples or pressure tapping tubes. In addition to the tightened bolts, gaskets and O-rings, the access ports and other points that are prone to leaks are sealed with silicon.

The plenum operates at an absolute pressure of 0.4 bar. This unusual decision of running the facility below atmospheric pressure is based on the fact that running under lower densities, less energy is required to circulate the air through the cascade, which of course means less power needed to drive the centrifugal compressor at operating conditions of the rig. This is achieved by using a Rietschle VCE 25 submerged oil vane type vacuum pump. This pump is connected to the plenum via a shell-and-tube heat exchanger, which allows for cooling of the vacuum pump during operating conditions.

The vacuum pressure used to be controlled by a Schmidt trigger (controller based on a comparator with built-in hysteresis), but a new system was implemented by G. Kennedy in 2004. A 4-20 mA pressure transducer monitors the total pressure inside the plenum by sending the corresponding voltage signal to a digital controller board. This has a relatively simple user interface, which allows the user to select the desired vacuum pressure levels, and displays this pressure as well as a reading for the total inlet temperature. The controller operates by sensing when the plenum reaches the set value of pressure, and sends a signal to a closed solenoid valve on the suction pipe of the vacuum pump which disengages it. The inevitable leakage in the system causes the pressure to rise, which opens the solenoid valve and re-activates the vacuum pump. By following this "loop", the pressure in the plenum is kept constant.

Varying the operating pressure inside the plenum allows for the varying of the Reynolds number based on chord length. The Reynolds number is directly proportional to density, which is directly proportional to the pressure, as shown in equations 4.2.2.1 and 4.2.2.2:

$$\mathrm{Re} = \frac{\rho D U}{\mu} \qquad (4.2.2.1)$$

where D = blade chord length, U = velocity of the fluid at a point, and μ = viscosity.

$$\rho = \frac{P}{RT} \qquad (4.2.2.2)$$

where P = respective pressure at the point, R = 287 J/kg.K = universal gas constant for air, and T = respective temperature at the point.

If the pressure is varied, it can be seen that this would result in a corresponding varying of the Reynolds number.

4.2.3 HYDRAULIC DRIVE AND CENTRIFUGAL COMPRESSOR

The centrifugal compressor rotor inside the plenum is driven by a hydraulic motor of 65 kW through a step-up gearbox of ratio 1:6. Air from the cascade flows into the eye of the compressor, and is expelled radially outwards into the plenum and recirculates back into the bell-mouth and cascade box.

A Uchida pump supplies the power and oil to the hydraulic motor. By changing the angle of the swash-plate on the Uchida pump (by manually turning a power screw above the pump), as shown in Figure 4-3, the flow rate of the hydraulic oil is adjusted. This is how the speed of the motor is controlled. The maximum working speed for the motor is 3 000 rpm, which translates to a maximum of 18 000 rpm of the compressor blade speed when run through the 1:6 step-up gearbox.

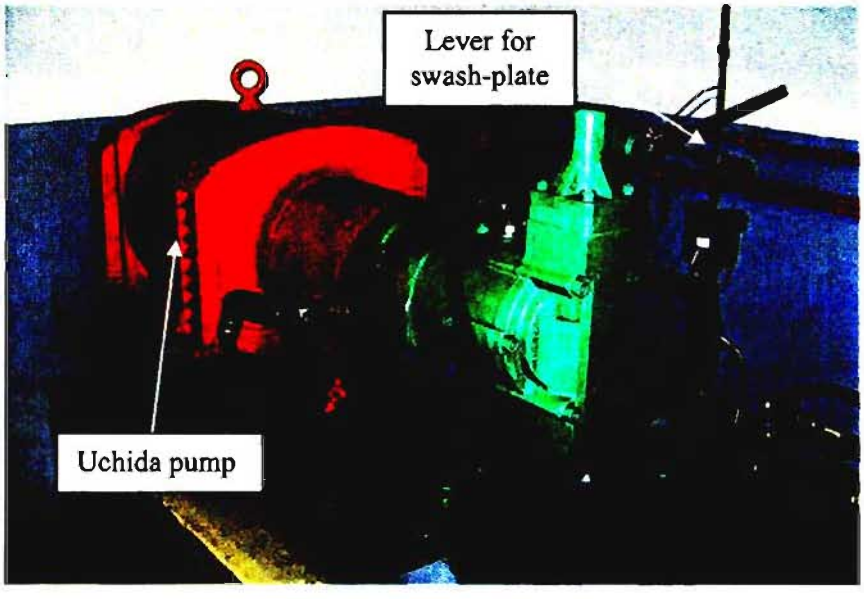

Figure 4-3: Uchida hydraulic swash-plate pump

By changing the angle of the swash-plate of the pump, the motor speed is varied, and therefore the velocity of the air and resulting Mach numbers can be adjusted to the desired value. The range of Mach numbers used at the inlet to the cascade box is between 0.3 and 0.5. There are various safety interlocks which are checked and passed before the hydraulic pump can be started, which includes the condition that the plenum pressure must be below 0.55 bar to avoid damage to the centrifugal compressor and carbon seal located at the back of the experimental rig. Once these checks have been passed, the prime pump and the main pump can be started.

4.2.4 GEARBOX LUBRICATION

The 1:6 step-up gearbox operates on a relatively high rpm range, and requires constant lubrication while in operation to avoid any catastrophic failures. A pneumatic motor provides the lubrication oil to the gearbox, which is driven by the workshop Hydrovane compressor operating at 6 bar. The oil is provided from an external 60 *l* oil sump, of which the operating temperature needs to be between 50 – 70 °C.

The decision to use a pneumatic motor to pump the lubrication oil was made because in the event of a power failure, lubrication oil will still be pumped through the gearbox for enough time while the centrifugal compressor safely slows down to a complete stop. To prevent the oil temperatures rising too high, the oil is passed through a shell-and-tube heat exchanger. By varying the water flow rate through the heat exchanger, the oil temperature can be safely controlled. Other safety interlocks that were installed are to check air pressure, oil pressure and oil flow rate. If any of these are compromised, any running of the gearbox would result in certain failure, and the hydraulics are prevented from starting.

4.2.5 FOUR-BLADE CASCADE

The cascade box within the plenum holds four SMR-95 high turning angle turbine blades, including the actual test blade itself. This test blade is used for all measurements, including the ability to take pressure measurements and heat transfer tests. The cascade has an inlet bell-mouth from which the air is sucked in, and has a square flange at the back to allow it to be bolted to the angled inlet diffuser that leads to the compressor. The tailboards on the pressure and suction side of the blade are fixed, although Snedden (1995) allowed for the tailboards to be adjustable. This allowed for minor adjustments if it was found that the cascade was losing periodicity. The cascade also has provisions to accommodate turbulence-generating rods to

measure the effects of turbulence intensities. These rods can be slotted in in front of the blades, and bolted tight. The rod sizes available are 2.4 mm grid (generating 15% turbulence intensity) and 3.2 mm grid (generating 25% turbulence intensity).

Table 4-1: Original Blade and Aerothermal Details (reproduced from Snedden (1995))

	INLET	OUTLET
Relative gas velocity (m/s)	410.46	613.72
Static pressure (kPa)	796.89	603.5
Static temperature (K)	1304.5	1216.1
Relative Mach No.	0.581	0.8997
Relative Reynolds No.	597713	756284
Relative flow angle	38.4°	28.6°
Chord (mm)	33.27	
Pitch (mm)	21.33	
T_{wall}/T_{∞}	0.86	

Table 4-2: Test Blade Details (reproduced from Snedden (1995))

Blade chord (mm)	94.8
Pitch/Chord ratio	0.675
Camber angle	113°
Blade span (mm)	80
Leading edge diameter (mm)	10
Scale amplification	2.85

The details for the SMR-95 test blade are given in the above tables. There are also total temperature and pressure probes that are placed at the inlet of the cascade, and inlet and outlet static pressure tappings. A top view layout of the cascade is shown in Figure 4-4.

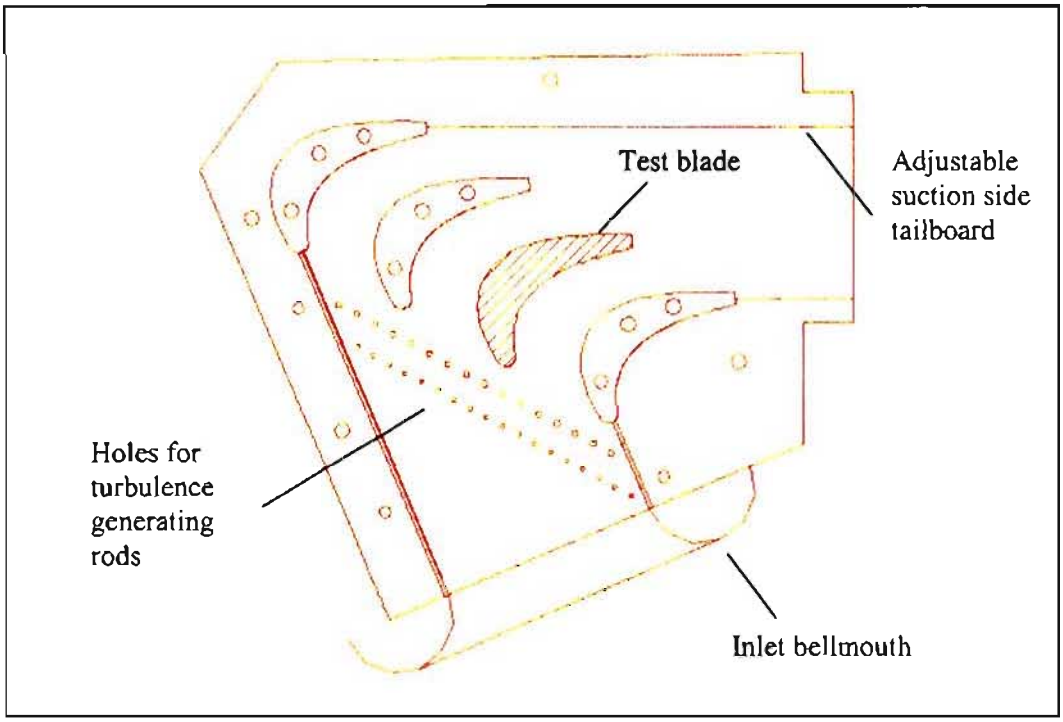

Figure 4-4: Top view of four-blade cascade (reproduced from De Villiers (2002))

4.2.6 ANNULAR RADIATOR

Housed inside the plenum, the annular radiator (shown in Figure 4-5) was fitted such that most of the exhaust air from the centrifugal compressor passed through it before entering the cascade box. At operating conditions, the temperature of the air would rise at undesirable levels, and would cause undue damage to certain components within the plenum. The temperature thus needed to be reduced and, quite importantly, needed to be controlled to be kept constant to allow continuity with numerous experimental tests that are run in series. By using this method, one can manually control the flow rate of water supplied through the radiator via two valves.

Figure 4-5: The annular cooling radiator

4.2.7 COOLING BOX

As discussed previously, heat transfer measurements are recorded from the experimental rig after a temperature change over the turbine test blade occurs. If the freestream air running over the blade is heated to around 100 °C, then the test blade needs to be at a much cooler temperature to allow for a sufficient temperature difference. Realistic freestream temperature ratios experienced in gas turbine engines are approximately 0.8.

The initial cooling method used on the supersonic cascade experimental rig was designed by McDonald (1994), which made use of a turbocharger that ran on the compressed air supply of the workshop's Hydrovane compressor after passing the air through four radiators. This method was replaced, as the wearing of the turbocharger seals proved to be a problem, including sealing problems against the vacuum pressure on the inlet of the turbocharger. It was replaced by an Effepizeta belt-driven blower, which utilises a closed loop within the plenum via two shell-and-tube heat exchangers. By running in a closed loop at the pressure within the plenum, it prevented problems with the overall performance of the vacuum pump and maintaining vacuum pressure of the plenum if an external source had been used. The cooling circuit begins where air is sucked from the base drain of the plenum through one heat exchanger. After passing through the blower, the air is run through another heat exchanger to achieve the desired cooling temperatures that would allow the test blade to remain at around 25 – 30 °C.

The cooling box is made from steel, with a lid that has a pair of inlet ports to run the cooled air from the blower over the test blade. The blade is surrounded by a perforated copper plate which allows for impingement, thereby increasing the cooling effect on the blade. The box is sealed with polyurethane foam to insulate it from the heated plenum air. A reasonably close tolerance hole is located at the bottom of the box to allow for the test blade to be plunged into the cascade and freestream air, without the gaps being large enough to let a significant amount of hot air inside.

4.2.8 PNEUMATIC RAM

To plunge the blade stack (consisting of the test blade on top of the dummy blade) from the cooling box into the cascade, and to retract it, a pneumatic ram is used together with a sliding mechanism. The device consists of a cylinder with two ports and a sliding ram, which is driven by compressed air. The ports on the cylinder are connected to two solenoid valves. By alternating which valve is open or closed, the direction from which the cylinder will fill up with compressed air is controlled, thereby allowing the user to control whether to plunge the blade into the cascade, or retract the blade back up into the cooling box. This is done via a simple switch on the data acquisition console.

The sliding mechanism is bolted onto the underside of the cascade, and consists of a plate with four linear bearings that run on nitrided rods. The blade stack is bolted onto the sliding plate. Since the plunging force caused a high acceleration (blade stack came to rest in 0.2 s) and impacted the bottom of the sliding mechanism quite hard, it caused a large spike in voltage readings as the shock affected the analogue circuitry quite badly. This was improved by adding FESTO pneumatic shock absorbers at the end of the sliding mechanism.

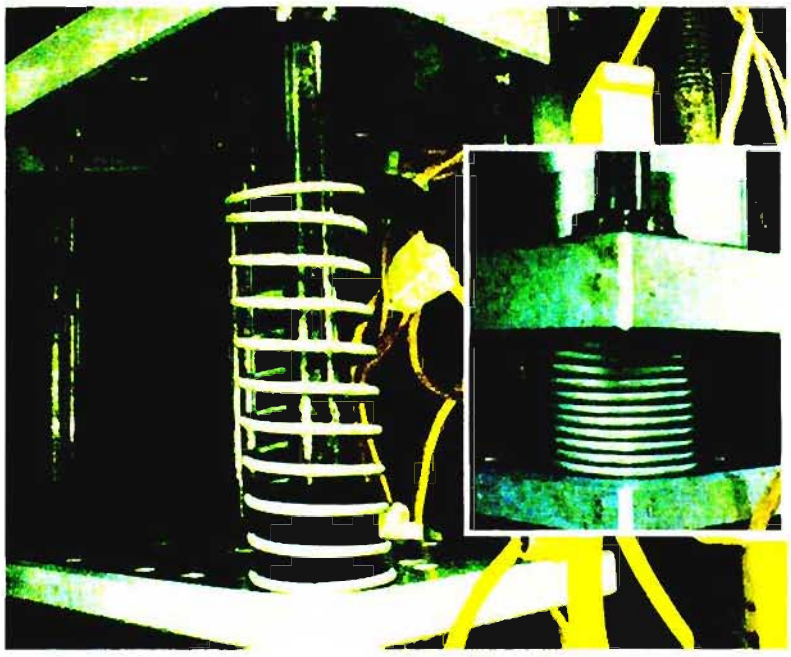

Figure 4-6: Compression spring to aid retraction process (insert shows the spring in its compressed position)

Due to corrosion on the nitrided surfaces, the process of retracting the blade stack became hampered, and the blade would get stuck in between at certain times. To rectify this problem, some lubrication was added to the rods, as well as the implementation of a helical compression

spring (as shown in Figure 4-6). This spring compressed upon the process of plunging the blade into the cascade, and the extra force of the spring allowed for full movement of the sliding mechanism when the blade was retracted. A schematic diagram of the pneumatic ram and sliding mechanism arrangement can be seen in Figure 4-7.

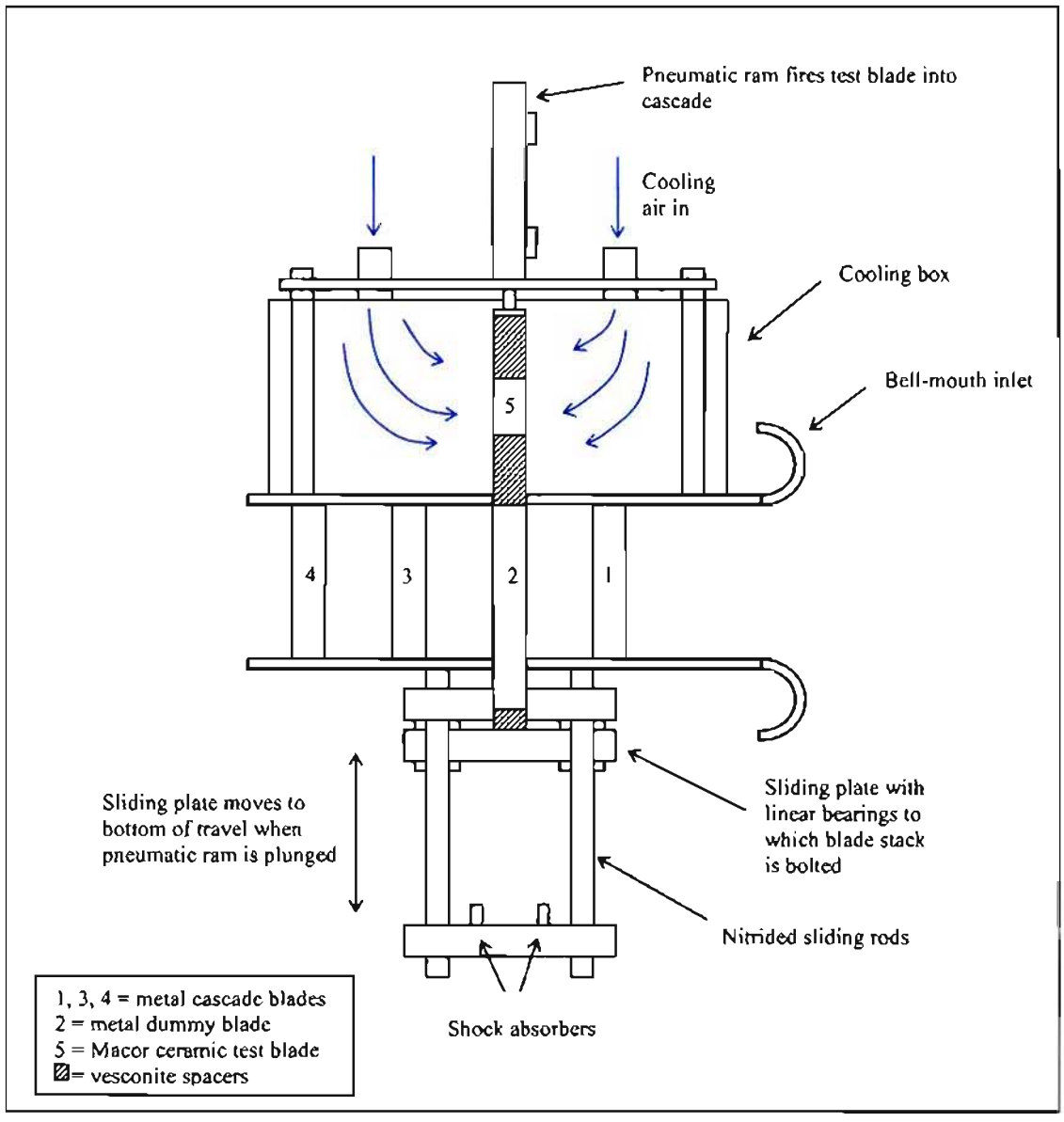

Figure 4-7: Layout of blade stack, cooling box and sliding mechanism assembly (reproduced from De Villiers (2002))

4.2.9 Safety and Control Circuitry

As discussed in previous sections, the successful and safe operation of the rig requires certain components to be functioning at minimum conditions such that there is no breakdown of any part of the rig. As there are so many fundamental components that need to be operating at a base

condition, there is no way to manually monitor the conditions safely. Thus a safety and control circuit was installed for constant automatic monitoring and shutting down of the rig if certain criteria are not met. The oil and air pressure are monitored, as well as the oil flow to the gearbox and the vacuum pressure inside the plenum. If any of these are compromised, the main hydraulics will be shut down and thus the rig operation will come to a halt, preventing any major damage that would result if it continued to run.

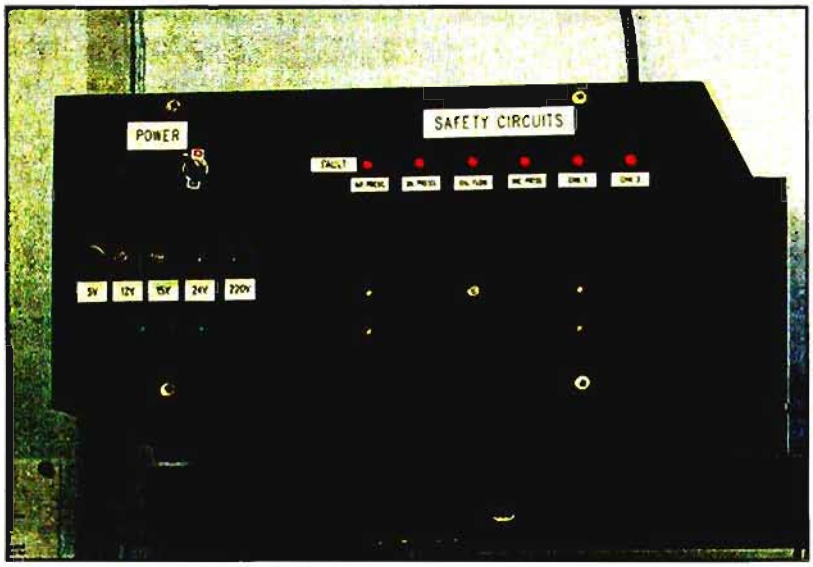

Figure 4-8: Safety control box

The safety interlock box is shown in Figure 4-8, made up of simple LEDs to inform the operator of the status of various components on the rig, by switching from red to green. Sufficient air pressure must be supplied from the workshop's Hydrovane compressor, and the vacuum pressure must be below 0.55 bar absolute.

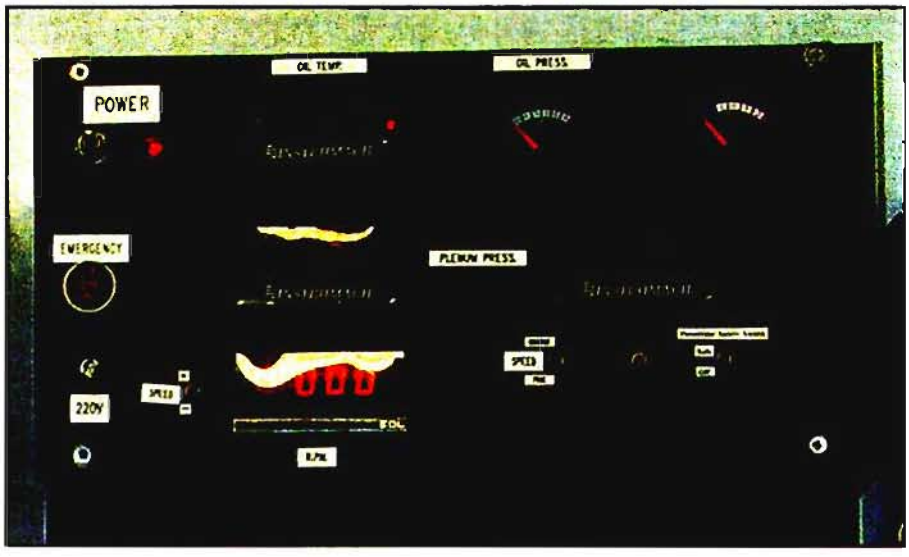

Figure 4-9: Display and control box

A Kulite pressure transducer provides the signal for the pressure control circuitry, and is digitally displayed on the display and control box, shown in Figure 4-9. There are also digital displays for the oil temperature and pressure, total and static inlet pressures, and the hydraulic motor speed. One of the most important readings is the oil temperature reading, and the operator must wait until the lubrication oil is heated to around 50 – 70 °C before starting up the hydraulics. A full rig starting procedure is given in Appendix C1.1. There is also a switch on the display box that can switch between fine and coarse adjustment of the hydraulic motor speed. This speed is measured by a tachometer and displayed in rpm. A large emergency stop button allows for the immediate and safe shutdown of the rig if there is any unforeseen failure of a component on the rig.

4.3 Heat Transfer Measurement

4.3.1 Blade Stack

The cascade box in the plenum houses three SMR-95 dummy blade profiles and one instrumented blade. For heat transfer measurements, a blade stack is bolted to the pneumatic ram and sliding mechanism to be plunged and retracted in and out of the cascade and cooling boxes, as discussed in previous sections.

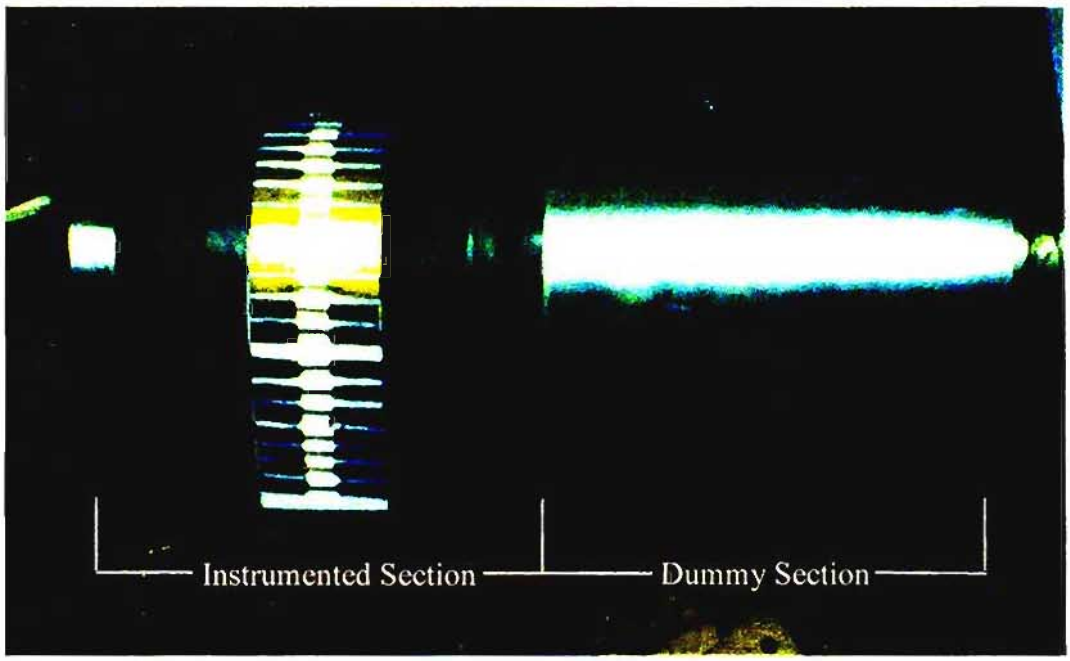

Figure 4-10: Blade stack

The instrumented blade is layered such that a dummy section can be displaced by the instrumented section when needed to, and vice versa. The instrumented Macor profile sits in the middle of the section, and spaced to the centre with Vesconite spacers. The dummy section is basically made of aluminium to the profile of the blade, as seen in Figure 4-10. Together with its purpose of spacing the Macor blade to the centre of the section, the Vesconite spacers also aid in preventing heat transfer from the aluminium dummy section.

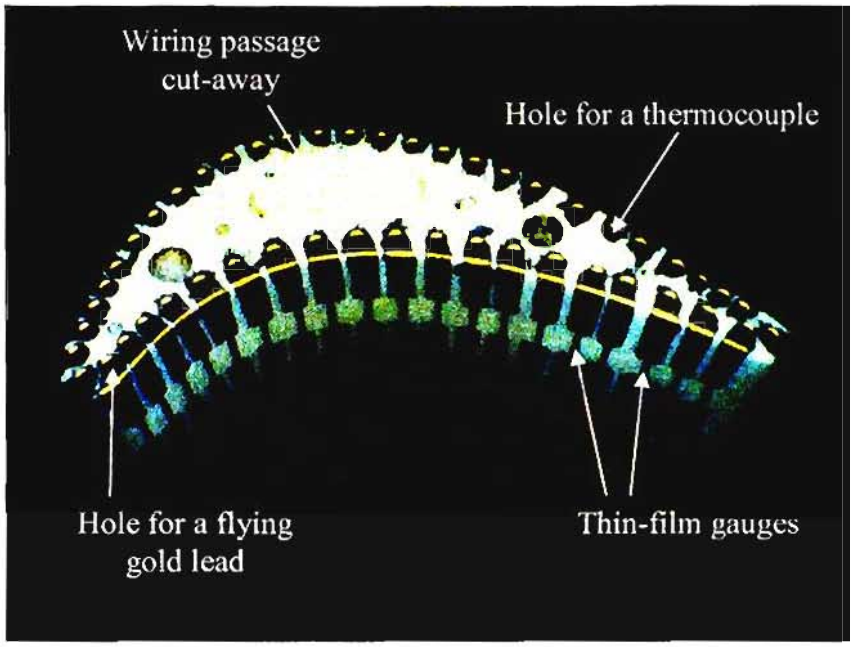

Figure 4-11: Instrumented Macor test blade

The Macor test blade is instrumented with platinum thin-film gauges, with 28 sensors on the suction side and 20 sensors on the pressure side, as shown in Figure 4-11. A full description of the painting and preparation of the thin-film gauges is given in Section 5.3.2, with the circumferential positions of each sensor shown in Appendix A1.2. These painted sensors are connected to flying gold lead attachments on the inside of the test blade via gold paint. The attachments are thereby connected to six D-type connectors (thus 8 sensors for each connector). The wiring and cable to the connectors are passed directly below the blade, away from the air stream and span-wise path of the blade stack when plunging and retracting, to avoid damage and further electrical noise to the external analogue cards. Four thermocouples are also set in at certain points inside the test blade, giving a more accurate representation of the blade temperature in the plunging process when needing to calculate the final heat flux distribution.

4.3.2 DATA ACQUISITION

The process of heat transfer data acquisition involves using a temperature-resistant thin-film gauge as discussed, which relates to a voltage change once the resistance changes when exposed to a higher or lower temperature. This voltage change is converted to a heat flux via physical analogy cards. Therefore, for each sensor on the blade, there must be a separate analogue card for each one. With there being 48 sensors on the teat blade, and wired into six different D-type connectors, there are only eight analogue cards that are used at a time for each D-type connector.

The analogue cards were designed by Oldfield *et al.* (1985), and incorporate a logarithmic method, as opposed to the method of Ligrani *et al.* (1982). This cuts down the required 32 sections to nine sections, and incorporates the use of lower-tolerance capacitors. The cards implemented by Snedden (1995) follow a suggestion from Oldfield *et al.* (1985) to implement the sections onto a total circuit, including a constant current source, voltage amplifier, and current-to-voltage converter. The cards were also improved with regard to noise reduction and sensitivity, such that the voltage change could be more apparent and clearer. A schematic diagram of the analogy cards is shown below in Figure 4-12.

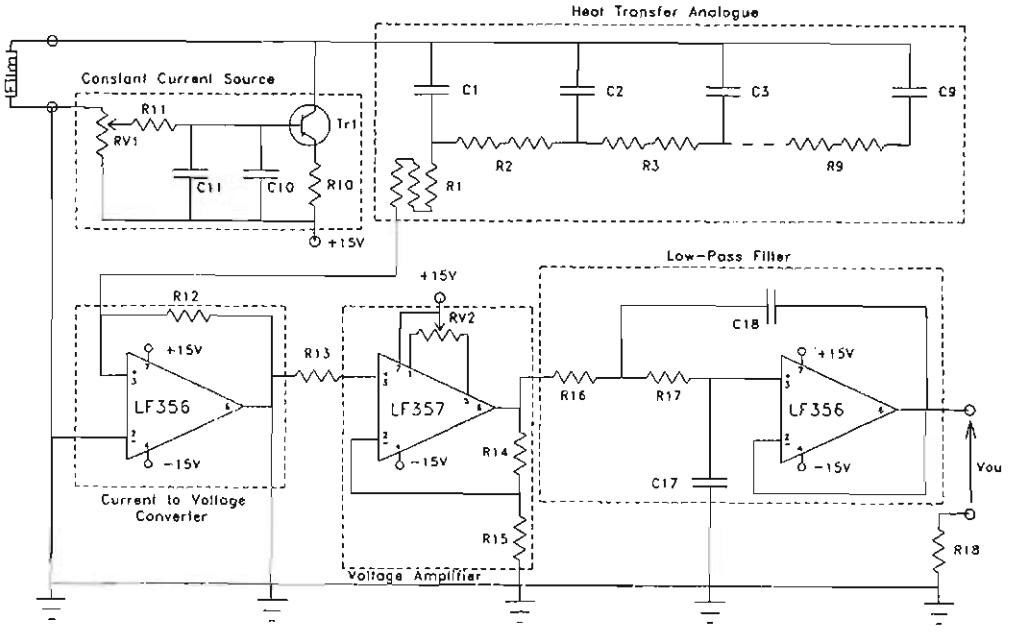

Figure 4-12: Heat transfer analogue circuit diagram (reproduced from Snedden (1995))

The disadvantage of this method is the electrical noise picked up in the readings, as well as the ability to only read the sensors sequentially. Thus the temperatures and compressor blade speeds will vary during the total period of reading of all six D-type connectors, and the overall result would not be as accurate as reading every sensor instantaneously at that specific time, for those specific conditions.

The output from the analogue cards is passed into a PC71 interface card designed by Eagle Technologies. This is connected to a PC30 PGL A/D card, which can be configured to display a range of 0-10 V or a bipolar range of ±5 V. The post-processing program used to display the resulting voltage readings is WaveView, of which the data can be captured and analysed. Various parameters can be set within this program, including the number of samples to be taken, the frequency and sampling time, and various other factors that would affect the final data capture file used to calculate heat transfer coefficients.

The data is analysed using LabView software, and makes use of a program that was written by Snedden (1995) to read in the voltage inputs and changes, and calculate the resulting heat transfer coefficients by reconstructing the wall temperature history from the captured data and voltage step change. This output is displayed by the program as typically seen in Figure 4-13. Further properties of the program "Isotemp1" are given in Appendix D1.2.

A graph of heat flux vs. temperature is plotted, and as explained by Ligrani *et al.* (1982), the isothermal heat flux is calculated by judging the gradient of straight line portion, and projecting it back to the y-axis, as shown below in Figure 4-14. The isothermal heat transfer coefficients are thus calculated by dividing each isothermal heat flux value by the change in temperature of the freestream air and the blade wall. After calculating the heat transfer coefficients for each sensor, the heat transfer distribution can be plotted along the midspan of the blade.

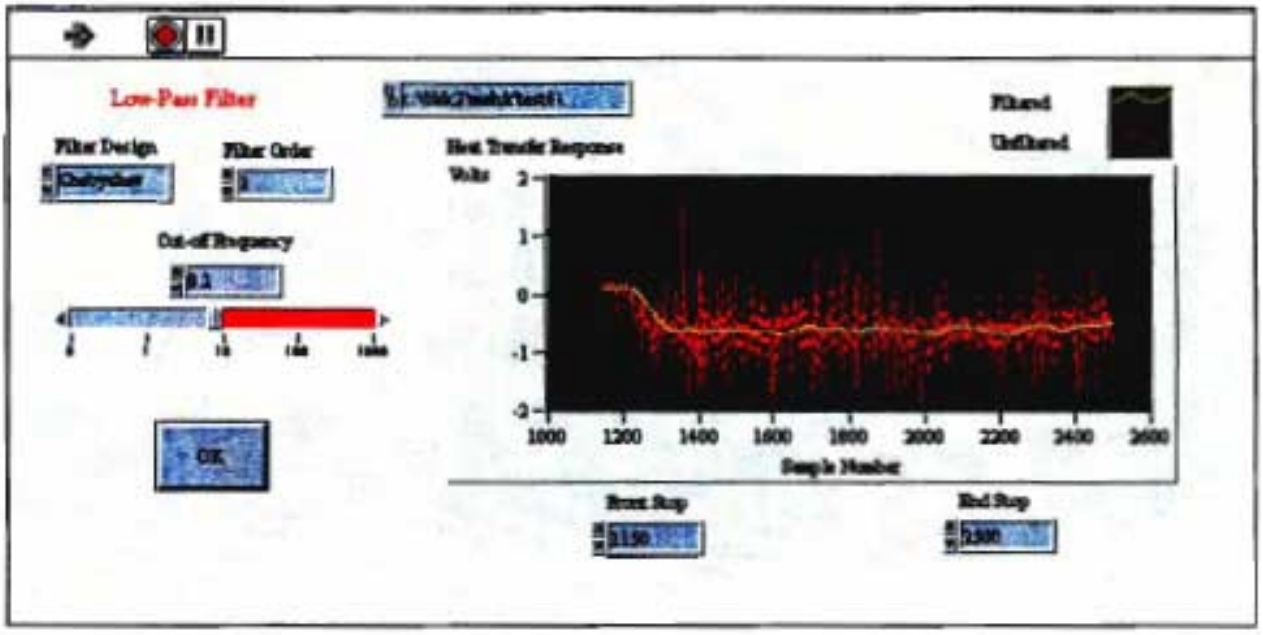

Figure 4-13: Typical voltage change and filtering using LabView

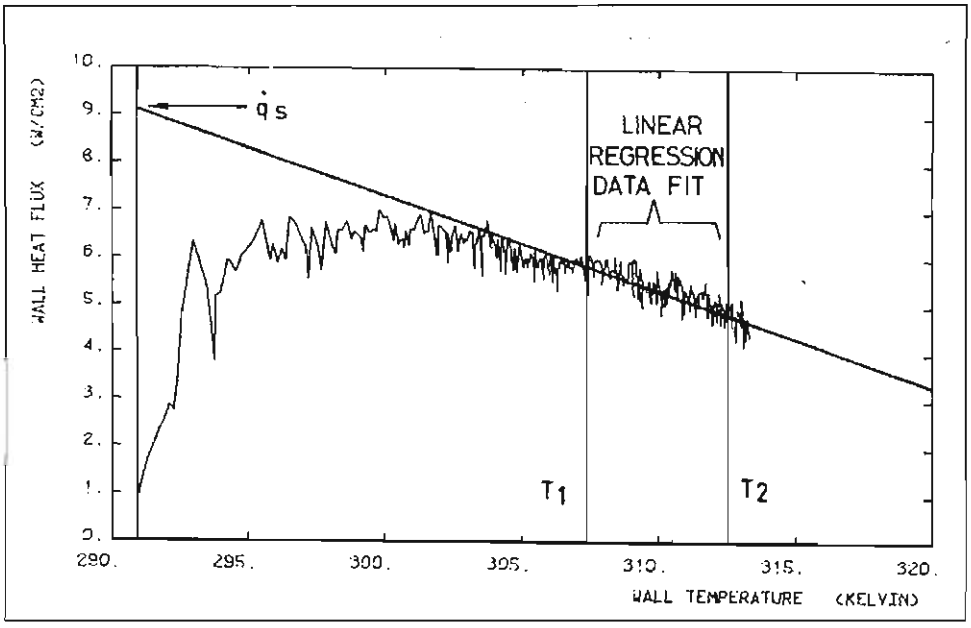

Figure 4-14: Heat flux vs. Temperature (reproduced from Ligrani *et al.* (1982))

4.3.3 Turbulence Generating Rods

The varying levels of turbulence during testing were generated using different sizes of vertical rods that were placed upstream of the SMR-95 test blade. These rods were designed and made by Snedden (1995) using the empirical correlation derived by Roach (1987) using the following formula:

$$Tu \approx 0.8\left(\frac{x}{d}\right)^{-\frac{5}{7}} \qquad (4.3.3.1)$$

where Tu represents the streamwise component of turbulence, x is the distance upstream, and d is the diameter of the rods.

The following restrictions are, however, placed on the dimensions of the grid:

1) The grid array should be less than 10% of the minimum side length. For example, if the grid span is 100 mm, the maximum distance perpendicular to the flow is 10 mm.

2) The array solidity must be less than 50%. This means that for a maximum spacing of 10 mm, the maximum rod diameter is limited to 5 mm.

It is also noted that homogeneous turbulence is only achieved at ten times the mesh length downstream, where the mesh length is the distance between the rod centres. Thus non-homogeneous turbulence exists at positions less than ten lengths downstream of the grid.

Snedden (1995) designed two sets of grids for two levels of turbulence intensity. The first set of rods were designed for a predicted 9.3% near homogeneous turbulence level, and used 2.4 mm diameter rods that were placed 10 mm apart and 6.21 mm perpendicular to the flow and 50 mm upstream of the test blade. The second set of rods was designed to generate non-homogeneous turbulence of 19.1%, and used 3.2 mm diameter rods placed 11.3 mm apart and 7 mm perpendicular to the flow and 25 mm upstream of the blade.

Turbulence measurements performed by Snedden (1998), however, showed that there was under-prediction of the turbulence levels. The grid that was designed to generate 9.3% was measured to generate 15.0%, and the grid designed to generate 19.1% was measured to generate 25.5% turbulence intensity at the operating conditions needed. He also noted that the turbulence level measured without grids was 3.0%. This is summarised in Table 4-3.

Table 4-3: Turbulence Generating Rods

Turbulence Grid	Rod Diameter	Distance Upstream	Rod Spacing	Predicted Tu %	Measured Tu %
None	N/A	N/A	N/A	0%	3.0%
Grid 1	2.4 mm	50 mm	10 mm	9.3%	15.0%
Grid 2	3.2 mm	25 mm	11.3 mm	19.1%	25.5%

4.4 Static Pressure Measurement

4.4.1 Test Blade

The static pressures are measured along the SMR-95 blade profile using a test blade instrumented with 42 pressure tappings, split into 20 pressure tappings on the pressure side and 23 tappings on the suction side (inclusive of the leading edge tapping). The two tappings at the trailing edge of the suction and pressure side are connected to the same port, which measures the average pressure at that point. These tappings were drilled along the mid-span of the blade, and are 0.5 mm in diameter. The positions of the pressure tapping points on the blade are shown in Figure 4-15. The exact circumferential distances are given in Table A1-3 in Appendix A1.2.

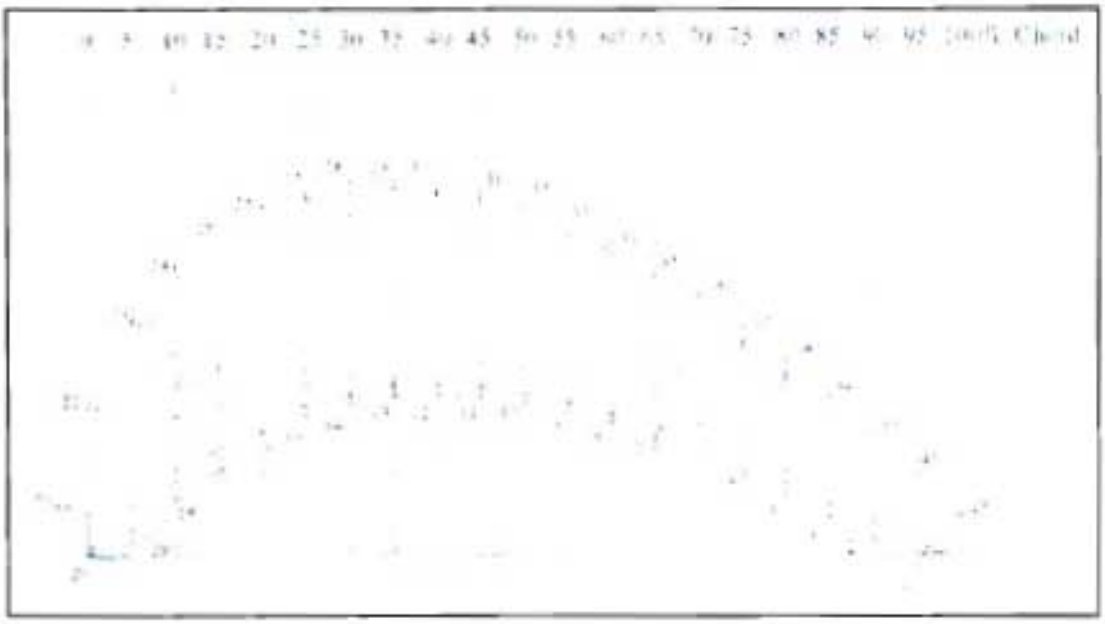

Figure 4-15: The SMR-95 test blade profile with static pressure tapping positions (reproduced from Snedden (1995))

This blade replaces the instrumented test blade for heat transfer when placed in the cascade. The cut-away in the cascade to make provision for the plunging process used in the heat transfer measurements (discussed in Section 4.2.8) is not needed for the static pressure tests, and the blade is fixed directly to a plate that covers the cut-away.

4.4.2 SCANIVALVE

The data acquisition of the pressure measurements involves the use of the scanivalve and pressure transducers. The scanivalve is a device used to capture the data of multiple pressure readings, and is shown in Figure 4-16. It has two 1-pole – 24-throw fluid switch wafers which are able to accommodate 24 readings per wafer taken in turn by a pressure transducer.

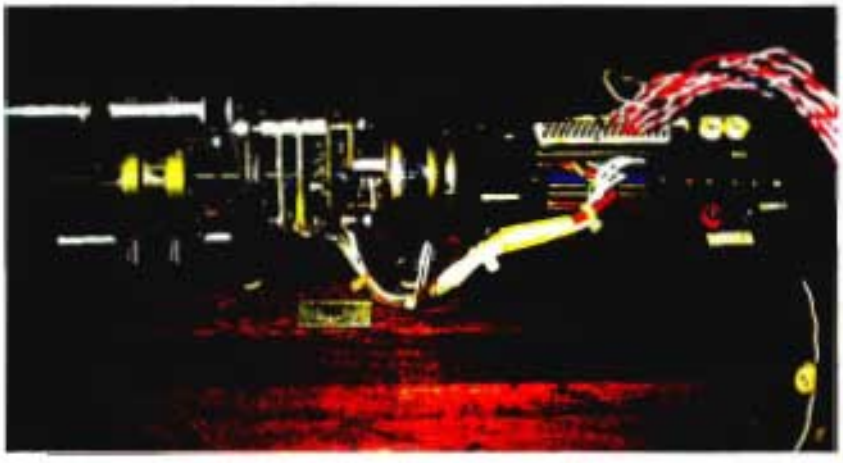

Figure 4-16: Scanivalve

Since there are two wafers and two pressure transducers, the 42 pressure tappings can all be connected to the scanivalve using silicon tubes, and this allows simultaneous measurement and all the data can be captured in one test. This minimises the experimental error, as the period for capturing allows fairly consistent operating conditions for every static pressure tapping measurement. A rotor in the scanivalve steps between each reading, which connects a common port on the wafers to each of the 24 ports on the stators.

The tappings on the suction side were connected to one wafer, while the tappings of the pressure side of the blade were connected to the remaining wafer. A balance pressure that is equal to (or greater than) the average pressures measured is needed to act as a rotor thrust bearing on the scanivalve. The total inlet pressure that was measured by a Kiel probe was connected and used to act as the balance pressure for the wafers. The two pressure transducers were connected to the common ports on the wafers, such that when the scanivalve steps to a new position, the reading from the wafers are read by the transducers. Remaining open ports on the scanivalve were used to read the static pressures at the inlet and outlet of the cascade.

4.4.3 ROSEMOUNT PRESSURE TRANSDUCERS

The measurement of the static pressures along the blade profile is performed using two Rosemount Range 5 differential pressure transducers. The output voltage from the transducers is proportional to the differential pressure. The input voltage is supplied from the scanivalve, which is outputted as a current (4 – 20 mA). This current is passed through a resistor of 470 Ω, and the resulting voltage is measured. The voltage range is between 1.88 V and 9.40 V.

The two ports on the transducer represents a high-pressure side (HP) and a low-pressure side (LP). The pressure difference between the two is measured. The common port from rotor on the scanivalve is connected to the LP side. A Kulite ITQ – 1000 total pressure transducer is used to measure the total cascade inlet pressure, and has a voltage range between 0 mV and 100 mV. This is connected to the HP side of the Rosemount transducer, and the total inlet pressure is monitored. Once the data is measured and converted to a pressure reading, the static pressures are calculated by subtracting the total inlet pressure with the measured pressure.

The pressure transducers were previously set to a certain pressure range by De Villiers (2002), who noted that the static pressures never exceeded 40 kPa as measured by Stieger (1998). Thus a calibration screw on the transducer was used to set the zero point at 1.88 V (the lowest output possible from the transducer) and the maximum pressure value of 40 kPa was set to correspond with the maximum voltage output of 9.4 V.

4.4.4 DATA ACQUISITION

The data acquisition system for the pressure measurement involves the use of an interface card, an A/D card, and the data is read into the software program LabView.

Previously, the voltage output signals from the scanivalve were read into a PC 30 U card used for voltage protection from large voltage spikes before being fed into the PC 30 PGL A/D card. Cassie (2006) replaced the PC 30 U card with a more advanced PC 71 interface card, which not only served as voltage protection, but improved the ease of interfacing and noise reduction and ground noise pickup. The first two channels for the voltage inputs were used to read the outputs of the Rosemount pressure transducers, and the card was configured such that LabView could read the voltages.

The PC 30 card serves as the main board of operations for the data acquisition system, and is connected to the PC 71 interface card. The card has 16 single-ended inputs and allows for different output ranges, namely bipolar (range between -5 V and +5 V) and unipolar (range between 0 V and 10 V). There were a number of settings on the card that were configured for the pressure testing. By reviewing the PC 30 card manual supplied by Eagle Technologies, the jumper settings were configured to allow for differential input, which reduces the noise that is usually experienced with the single-ended inputs. This reduced the 16 inputs down to eight analogue inputs. These were set for a unipolar input range to accommodate the voltage range of the Rosemount pressure transducers (range between 1.88 V and 9.4 V).

The software program LabView allowed for the controlling of the stepper motor used for the scanivalve, together with reading the voltages from the pressure transducers and monitoring the position of the scanivalve rotor. The program "Pressure Measurement", which was written by De Villiers (2002), also converted the voltage readings to pressure by using calibration constants acquired from calibrating the Rosemount differential pressure transducers and the Kulite pressure transducer.

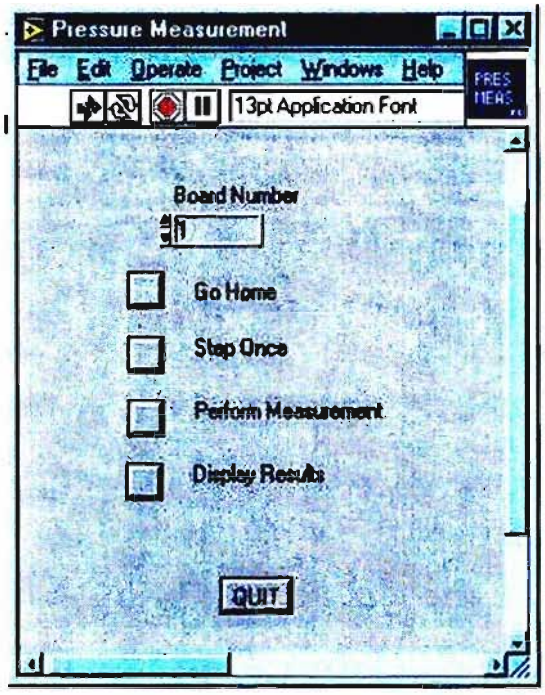

Figure 4-17: Display interface for the program "Pressure Measurement"

As can be seen in Figure 4-17, the program allows for a number of tasks to be performed. By creating a program using built-in sub-programs called VIs (Virtual Instruments) and recreating the Pascal program written by Stieger (1998), De Villiers (2002) was able to provide and interface between the PC 30 card and LabView. The "Go Home" button ensures the scanivalve is in its original position to start any tests by stepping the rotor until that position is reached. "Step Once" allows the user to step the scanivalve rotor once, which basically validates that all systems are working. "Perform Measurement" gives the command for the scanivalve to begin stepping between each port and recording the readings from the Rosemount pressure transducers. "Display Results" finally shows the results of the test and converts the voltage readings into pressure measurements.

The details of this program are given in Appendix 2 of De Villiers (2002).

CHAPTER 5

EXPERIMENTAL FLOW AND HEAT TRANSFER MEASUREMENT

5.1 OVERVIEW

The supersonic cascade experimental facility at UKZN has been used as an ongoing project to generate heat transfer results as well as aerodynamic studies by testing static pressure distributions across the blade. The long-term aim would be to have an experimental facility that would be reliable and easy to use, and generate accurate results with good repeatability. This would allow for the possible implementation of different blade profiles, knowing that results can be generated quickly and efficiently. This would also allow for the study of specific problems experienced in real-world circumstances, and the research would thus be directly helpful to the related industry.

The current work performed on the experimental facility is to ensure repeatability, and to show that there has been continuity of results despite various lengthy downtimes between students and general issues that have affected the performance of the rig, mainly the ageing factor and maintenance.

Since the implementation of data acquisition of heat transfer in 1995, little has been done to evolve the testing methods and techniques of the UKZN facility. The rig has been plagued by problems, with certain components breaking down and malfunctioning due to ageing. Thus it has seemed to be a constant cycle of repairing all the items in question, and generating results to compare to previous work to ensure that the facility has been repaired to a satisfactory condition.

The tests performed and results generated, illustrated in this dissertation, have been done to summarise and validate what results the facility is capable of generating. Thus, the way forward is shown in terms of upgrading equipment, techniques and methodology, to keep on track from the main long-term goal, which has seemed to be derailed due to various circumstances, planning and funding.

Static pressure tests were performed to validate the flow study that has been performed by every previous student who has worked on the project. This validation would be necessary to move on to the heat transfer measurement testing, and establish that the rig would be functioning in a

similar condition to when results were generated previously. The downtime, repairing and replacement of certain components made this validation necessary. The heat transfer test blade needed restoration, as there was an unsatisfactory number of broken sensors on the blade. With the limited resolution of sensors already on the blade, most of them had to work such that an accurate analysis of the heat transfer coefficient distribution could be performed.

A secondary reason for the restoration of the sensors was that the data acquisition system generated too much electrical noise, an amount that could affect the results as the sensitivity was relatively poor in this regard. By repainting the sensors on the blade, it was thought to have increased sensitivity under temperature changes so that the output would be clearer. It was anticipated that the post-processing procedure would yield better results as there would be no compromise in searching for correct values through an unwanted amount of data filtering due to the electrical noise. The test blade was repainted with platinum thin-film heat gauges, together with the gold paint connections, which provided full resolution on the blade and an increased sensitivity with regard to temperature changes.

Turbulence intensity generating grids were also used in testing to validate results attained by Stieger (1998), since no related tests have been performed on the rig since then. The grids used were designed by Snedden (1995) and generated turbulence intensities of 15% and 25.5%, and by using similar test conditions, the results were compared directly to Stieger's with favourable outcomes. All heat transfer data was generated using the existing data acquisition technique implemented by Snedden (1995).

5.2 Static Pressure Tests

5.2.1 Introduction

The flow and aerodynamic analysis of the SMR-95 blade was performed by analysing the static pressure distribution along the blade profile. By performing this test, one could also assess the condition of the supersonic cascade facility, as there had been numerous problems hindering the consistency of its performance and reliability. Before testing could commence, the pressure measurement equipment had to be calibrated, which included the calibration of the pressure transducers. Once this was completed, the static pressure tests could be performed and directly compared to that of the results of previous postgraduate students.

5.2.2 CALIBRATION

The calibration of the pressure transducers included the calibration for both Rosemount A and Rosemount B differential pressure transducers, as well as for the Kulite total pressure transducer. This involved plotting the relationship between the differential pressure measured and the corresponding output voltage signal. The resulting curve is thus essential to accurately relate the voltage signals and converting them to the correct pressure readings.

The calibration procedure varied slightly for the different types of transducers. For the Rosemount transducers, the total inlet pressure tapping of the plenum was connected to the low-pressure (LP) side, and the high-pressure (HP) side was left open to atmospheric pressure. The pressures were closely observed with the use of a simple U-tube mercury manometer. To observe the voltage signals, the PC 30 A/D card was connected on the first two channels and read through the software program WaveView. The previous setting on the card was for differential voltage output of -5 to +5 V, and by using the Eagle Technologies PC 30 card manual, the required jumper setting was found to change the voltage output to the absolute range of 0 V to10 V.

The vacuum pump was switched on and the pressure inside the plenum began to decrease. While the voltage changes were being captured in WaveView, the height of the mercury in the manometer was observed. The different heights were recorded in 20-second intervals for 3 minutes and 20 seconds (10 measurements) using a stopwatch.

The height measurements were converted into pressure readings using the formula:

$$\Delta P = \rho g h \qquad (5.2.2.1)$$

where ρ = 13600 kg/m^3 (density of mercury), and g = 9.81 m/s^2 (acceleration due to gravity), and h is the difference in the height of the mercury level.

Once the differential pressures are calculated, the values are plotted against the output voltage readings. These are acquired from the data file extracted from WaveView, and each voltage reading corresponding to the 20-second intervals used for the height measurements was recorded. An example of a Rosemount sensor calibration curve is shown in Figure 5-1. The calibration curves and procedure are given in Appendix C1.4.

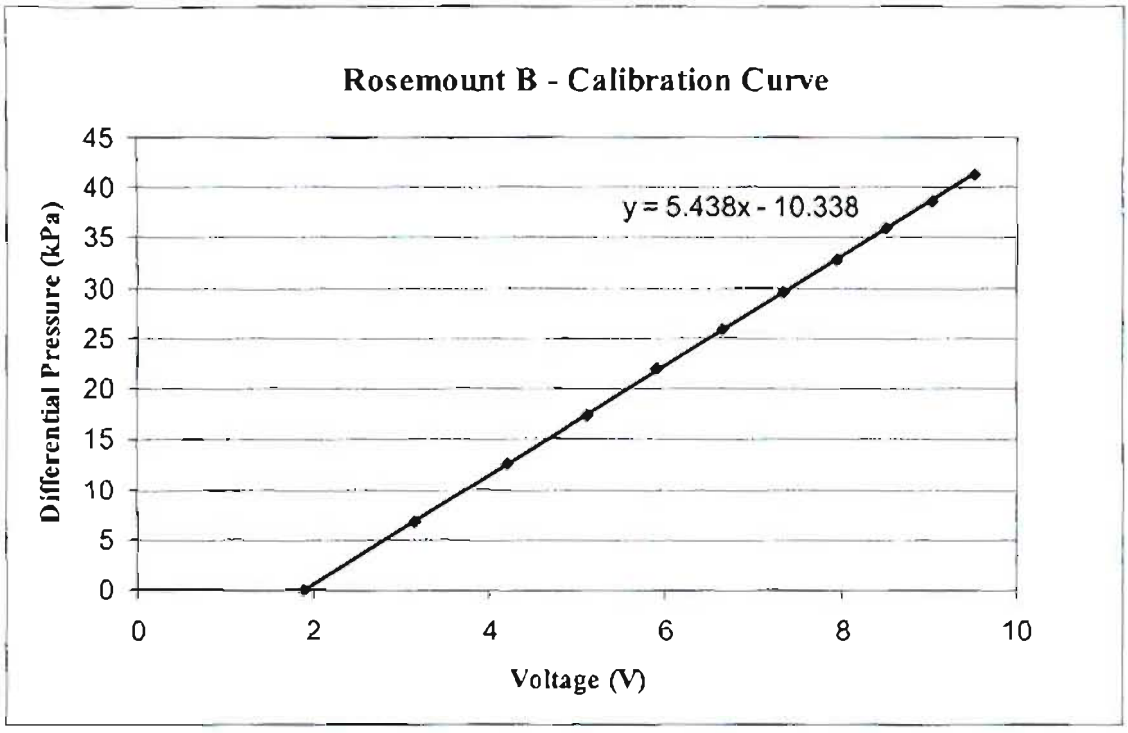

Figure 5-1: Calibration curve for Rosemount B differential pressure transducer

To calibrate the Kulite ITQ-1000 pressure transducer, the third channel of the PC 30 A/D card was connected and a similar procedure was followed to that of the Rosemount transducers. The total pressure was plotted against the voltage changes as the Kulite pressure transducer measures total pressure and not differential pressure. This total pressure range of the plenum was plotted against the 0 -100 mV range of the Kulite voltage output, as shown in Figure 5-2. The full procedure for calibration of the Kulite pressure transducer is given in Appendix C1.5.

The calibration constants are acquired by calculating the *y*-intercepts and the gradients of the straight lines. These values need to be used as parameter constants in the LabView program "Pressure Measurement", written by De Villiers (2002), as described in Section 3.4.6. Once these values were acquired, the pressure tests could be performed.

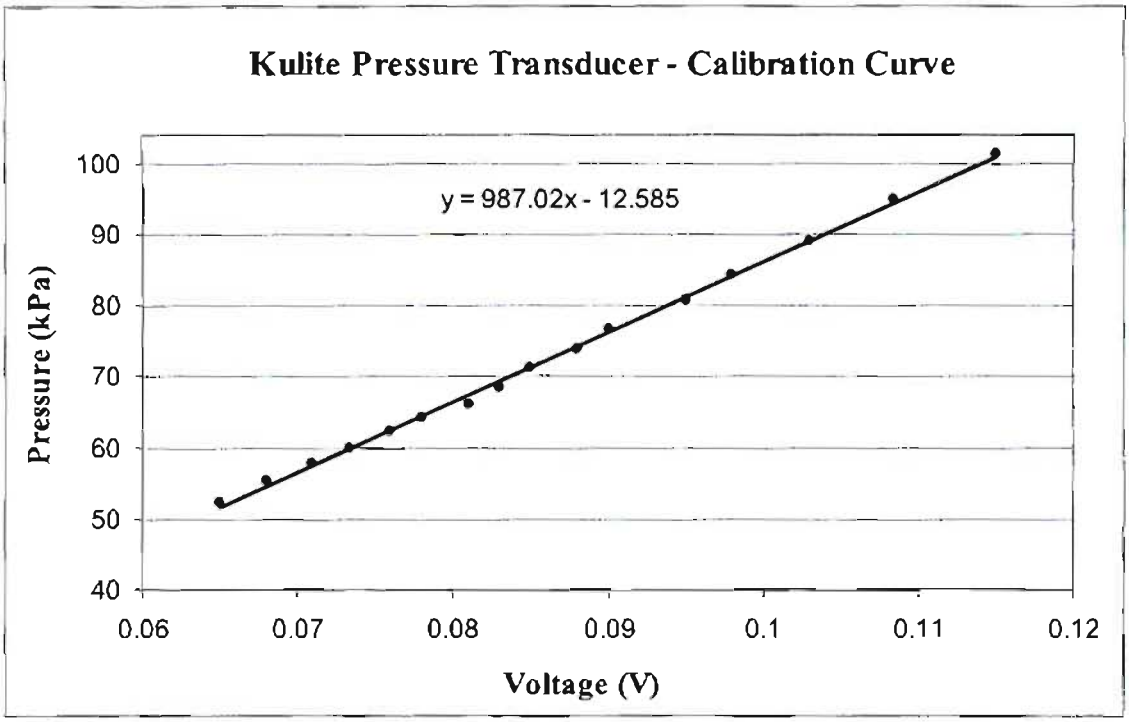

Figure 5-2: Calibration curve for the Kulite pressure transducer

5.2.3 Static Pressure Testing

5.2.3.1 Running of the Facility

The experimental cascade rig was set up for pressure testing by carefully assembling the pressure acquisition equipment. The cascade box was removed from inside the plenum, and the SMR-95 test blade with the static pressure tappings was bolted onto a plate which was fitted to the cascade. The various ports on the plenum that were set up for heat transfer testing were removed and replaced with those to accommodate the silicon pressure tubes from the test blade.

Once the cascade box was carefully placed inside the plenum and bolted to the diffuser in its correct position, the test blade needed to be connected to the scanivalve for data acquisition. The 42 silicon tubes from the blade were carefully labelled and fitted to the corresponding ports on the scanivalve via the plenum port. The pressure-side tappings were connected to one of the scanivalve switch wafers, while the suction-side tappings were connected to the remaining wafer. The ports that were left open were connected to other pressure tappings fitted around the plenum. The two inlet and two outlet static pressure tappings of the cascade box were joined together in similar fashion to provide an average pressure of the cascade inlet static pressure and outlet static pressure separately. These two silicon tubes were connected to the ports of the

scanivalve. The Kiel probe that measured the cascade inlet total pressure was also connected to the ports free on one of the scanivalve wafer. The final items of equipment were the two Rosemount differential pressure transducers, which were also connected to the ports. Once all the tubing was connected successfully, final checks were done to ensure everything was fitted properly. The loose silicon tubes and thermocouple wires inside the plenum were fixed in positions that would not cause disruptions to the air flow into the cascade inlet by using clear tape, and the dished end was sealed.

Before starting up the rig, the oil levels of the various concerning equipment were checked, and the setting of the water valves was reset. The vacuum pump was switched on and the hydraulic drive was started up without a problem. The actual detailed start-up procedure for the supersonic cascade rig can be found in Appendix A1.1. The rig was then set up for base test conditions for the data acquisition. These were the same conditions as used by previous students who worked on the project, and this was done to directly compare results and to demonstrate the facility's continuity.

The vacuum pump was set to evacuate the air in the plenum until the total absolute pressure reached 40 kPa. The compressor blade speed was increased to 2 500 rpm, which resulted in the inlet Mach number to be around 0.44 and the outlet Mach number at around 0.77 as measured by De Villiers (2002). As the speed of the compressor blade and air flow increased, the temperature inside the plenum also increased. This temperature was monitored and adjusted to the desired value of 100 °C by the use of the cooling water flow rate through the annular radiator. This value fluctuated, together with that of the compressor speed, and both had to be constantly monitored and adjusted throughout the testing procedure. As no turbulence intensity grid was used, the value of the freestream turbulence is 3%, as measured by Snedden (1995). The base test conditions are outlined in Table 5-1.

Table 5-1: Test Conditions

Total Inlet Pressure (absolute)	40 kPa
Compressor Motor Speed	2500 rpm
Turbulence Intensity	3%
Mach Number at Inlet	0.44
Mach Number at Outlet	0.77
Reynolds Number	2.8×10^5

Once the conditions were reached, the data could be acquired and the LabView program "Pressure Measurement" was run. Two sets of readings were taken to ascertain the repeatability of the results. The rig was then shut down after the scanivalve had switched through all its ports, and the data was then analysed and plotted, and compared to previous results.

5.2.3.2 Static Pressure Results and Analysis

The static pressure results were acquired using LabView, and extracted into Microsoft Excel. Since the acquired data resulted from tests performed with the Rosemount differential pressure transducers, the values had to be subtracted from the total inlet pressure of 40 kPa (absolute) to attain the static pressure values. These values were plotted against the circumferential distance of the SMR-95 test blade, as shown in Figure 5-3.

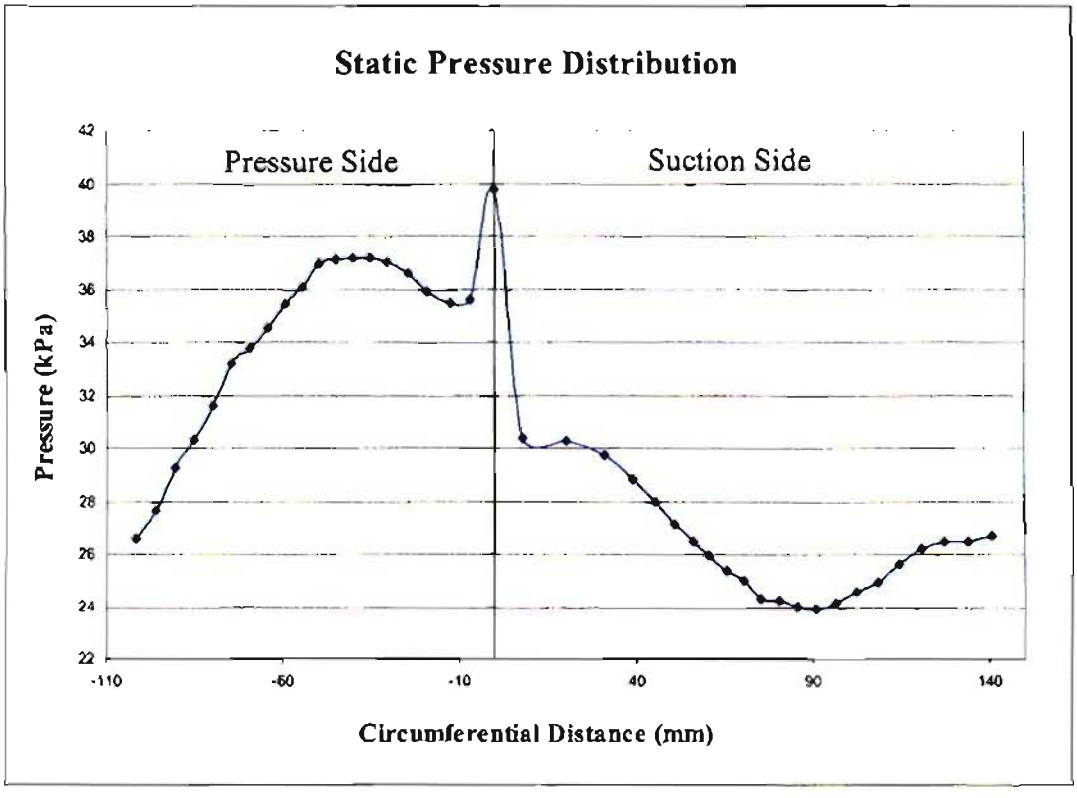

Figure 5-3: Experimental static pressure distribution

One can see the maximum static pressure logically at the leading edge of the blade, where the air impinges. On both sides of the leading edge of the blade, the resulting drop in pressure to around 34.8 kPa on the pressure side and 30 kPa on the suction side before pressure recovery is indicative of a separation bubble that forms due to acute angle change of the geometry of the SMR-95 blade. This is discussed in detail later in Section 5.3.5.4 of Chapter 5.

The most recent static pressure testing on the experimental supersonic cascade facility was performed by Cassie (2006), and the results were compared directly in Figure 5-4. The data measured compared really well to that of Cassie (2006), with minimal discrepancy, showing the favourable continuity and stability of the experimental facility.

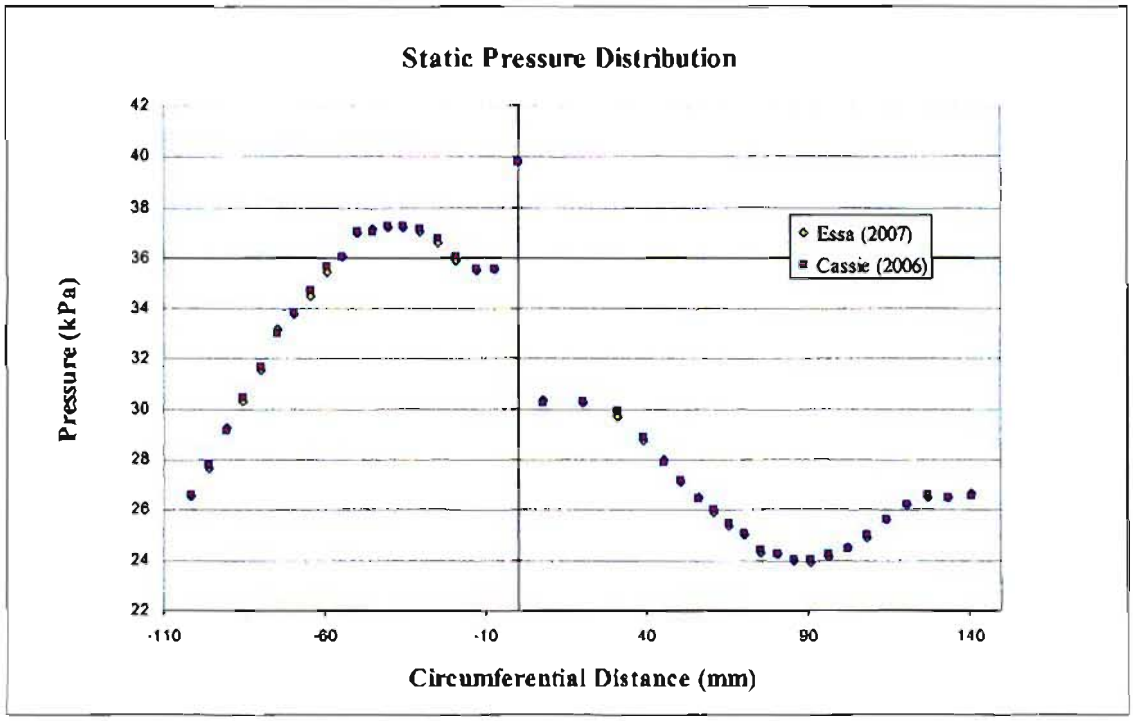

Figure 5-4: Direct comparison of results with Cassie (2006)

The tests that Cassie (2006) carried out involved using two working Rosemount pressure transducers, and he compared his results to that of De Villiers (2002), who only used one pressure transducer, as shown in Figure 5-5. The accuracy of those results would be hindered since two runs must be completed with one transducer for both the pressure side and suction side. This proved to be the case, as investigation by Cassie (2006) revealed that the compressor blade speed was at 100 rpm higher for De Villiers' (2002) suction-side test. This resulted in the correlation on the suction side to vary slightly, and this was found to be the only real discrepancy in results. The static pressure results of Snedden (1998) also correlated well, with minor deviations as also shown in Figure 5-5.

Thus the static pressure distribution compares extremely well to that of results of previous students, most notably to that of Cassie (2006), as the experimental rig was in very similar condition when performing the tests.

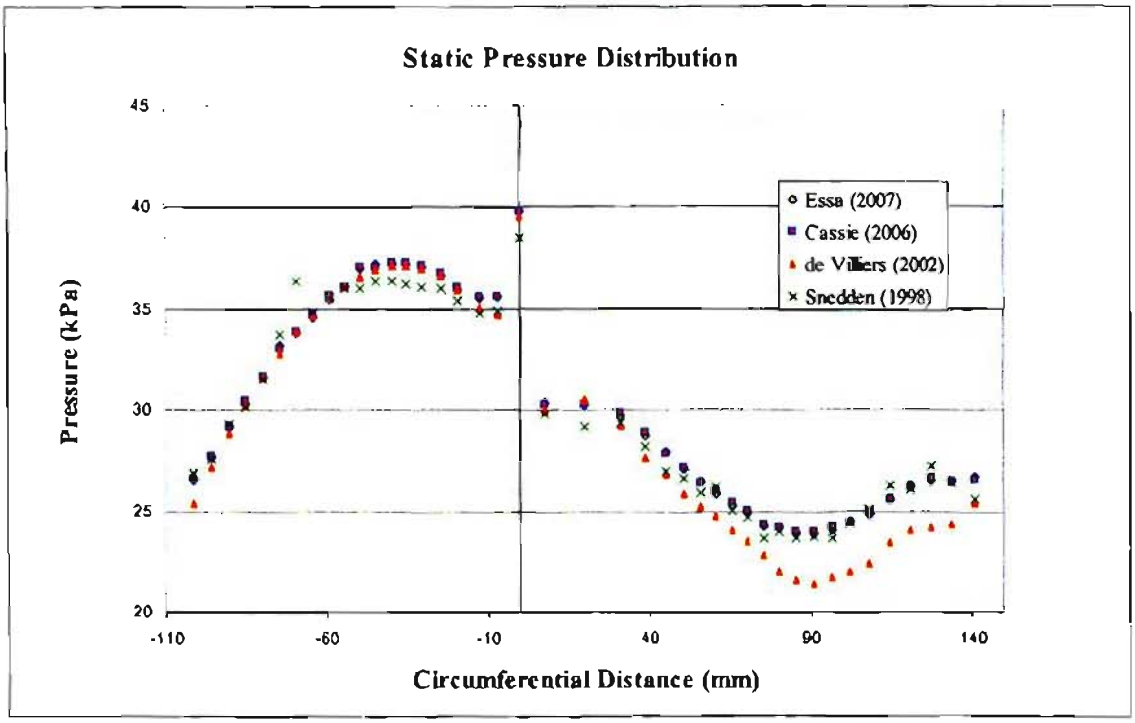

Figure 5-5: Comparison of static pressure results

After the initial tests to acquire the static pressure distribution on the SMR-95 blade, the results proved to compare favourably to those of previous students who worked on the project. There are numerous experimental errors that could contribute to the final accuracy of results, which mainly concern the varying compressor motor speeds and total temperature. These had to be kept constant by manual adjustment, but the conditions were kept fairly consistent throughout the process due to the fact that the data acquisition system could acquire all the measurements on the blade profile in one test. Not having this full resolution could cause major inaccuracies as demonstrated by the results of De Villiers (2002), who had to run two separate tests for both the pressure side and suction side. This brought about the possibility of different operating conditions, which was evident as discussed by Cassie (2006).

Together with further insight into the aerodynamic properties and behaviour, it was encouraging that the experimental rig was functioning reliably. Results could be obtained and compared without much discrepancy or deviation, which is a successful aim achieved before undergoing the heat transfer testing, which was the main focus of the dissertation.

5.3 HEAT TRANSFER TESTS

5.3.1 INTRODUCTION

To successfully generate an accurate heat transfer coefficient distribution along the profile of the test blade, all components and electrical equipment had to function optimally. Over the years since its implementation by Snedden (1995), some sensors on the blade have been damaged and broken, as well as certain circuitry issues which plague the data acquisition system. Broken op-amps on the heat transfer analogue cards were found and replaced, and it was decided to repaint all the sensors on the blade to achieve higher sensitivity as well as full resolution.

5.3.2 RE-INSTRUMENTATION OF THIN-FILM GAUGES

5.3.2.1 PREPARATION OF MACOR

Before applying and making the new sensors on the SMR-95 test blade, the existing sensors had to be removed and the surface of the Macor substrate sufficiently prepared for the gauges to be baked correctly. The heat transfer blade stack was carefully taken apart to isolate the Macor section. It was noted at the fragility of the internal wiring, and in the process of dismantling the blade, some gold leads broke off the ends of the wires quite easily and needed to be soldered back on before re-assembly.

Once the Macor section was totally isolated, the existing sensors were easily removed by scraping them off with water paper. Before applying the paint on the surface, it needs to be perfectly smooth such that the paint does not sink into any cracks and cause a malfunction of the sensor. The blade surface was then repolished with finer grades of water paper, with the final grade being 1 200 grade. Excessive sanding was avoided to keep the loss of material to a minimum, as the remaining sections of the blade stack were a fixed size and any step in the blade stack surface would result in losses in the air stream.

The process of smoothing the blade surface involved constant scrutiny using a metallurgy microscope. Ligrani *et al.* (1982) used cerium oxide powder on the surface of the substrate as a final polish in the procedure for a near optical finish as to optimise adhesion of the paint. OPS suspended silica was used instead due to the availability at the UKZN Metallurgy section.

5.3.2.2 PLATINUM PAINTING

The next step after ensuring a satisfactory smooth substrate surface is to paint the thin-film gauges. The Council for Scientific and Industrial Research (CSIR) donated Liquid Bright Platinum 05-X for the thin-film gauges, and Liquid Bright Gold NW for the electrical connectivity to the gold leads on the inside of the blade.

Before application of the platinum paint, a number of considerations were taken into account. The positions of each sensor were kept the same as the previous set, for ease of comparison to previous results. The spacing between each of the previous sensors was noted before removal, and a general guideline was to follow the lead holes on the sides of the blade. To achieve the required resistance, each sensor has to be painted using a specific length, width and concentration of paint. Following suggestion from Ligrani *et al.* (1982), the paint was applied to the surface, 1mm in width and approximately 1cm long, using a ruling pen for intricacy and a Vernier caliper for measurement. Before application, the paint was mixed with a thinner with a ratio of two drops per drop of paint. This ensured that the paint was not too concentrated such that there would be poor adhesion, and a higher value of resistance. To achieve the required value of resistance, it was necessary to paint and fire another layer of paint over the previous layer. This was following a guideline of Snedden (1995) in which he painted three layers of paint to achieve resistances of under 50 Ω.

The process followed to successfully paint and bake the thin-film platinum gauges is as follows:

- Carefully paint lines of paint onto one side of the blade.
- Dry the paint under an infra-red lamp.
- Complete painting platinum strips on opposite side of the blade.
- Dry the remaining wet paint under the infra-red lamp.
- Fire the blade in an open furnace at 350 °C for 30 minutes.
- Complete baking by placing the blade in a closed furnace at approximately 680 °C for another half an hour.
- Repeat entire process if another layer is required.

The process involved painting and drying each side of the blade separately to avoid any running of wet paint on the other side, since only one lamp was available to use. The paint generally required approximately half an hour to dry under the lamp. The baking and firing of the blade was performed to remove the carriers in the paint, and the platinum to bond to the substrate surface. This was achieved by firing the blade in an open furnace at 350 °C for half an hour. The

ventilation allowed removal of the solvents from the paint such they did not hamper the sintering process. This process was achieved by closing the door of the electric furnace and baking the blade at 700 °C for another half an hour. It was noted that the furnace did take approximately 40-45 minutes to reach the desired temperature. This process sinters the metal particles together, which ensures good electrical properties and adhesion to the substrate surface. After this entire process of painting and firing, the blade was left in the cooling furnace such that there is no sudden shock to the surface to a massive temperature change, which may lead to the development of cracks. The process described above required an entire day for each layer of paint needed.

Once the desired resistances were reached after two layers of paint, the blade was placed in the furnace at 180 °C for three days as an annealing process, and the resistances were monitored each day for any changes. This was taken as a suggestion from Snedden (1995), who noted that it took approximately three days for there to be no reduction in the resistances in his annealing process. Once this is achieved, one can calibrate the blade safely, as calibration would involve heating and cooling of the blade. If the annealing process is neglected, there might be resistance changes despite calibration, and the resulting experiments will be inaccurate.

5.3.2.3 GOLD PAINTING

The Liquid Bright Gold NW paint used for the connectivity of the platinum thin-film gauges was almost ideal for electrical properties and convenience. The change in resistance of the platinum gauges when plunging the blade is only needed, and the resistance of the connecting paint, leads and wiring must be kept to a minimum to maintain accuracy. The advantage of using the gold paint is that the resistance is minimal, and the process of painting and firing of the gold is almost identical to that of the platinum painting process. This saves a lot of time in what is already a lengthy process.

The gold paint was mixed in similar fashion to the platinum with the thinners, and painted carefully on the blade using a very fine paintbrush. To keep resistance as low as possible, the thickness of the painted strips must be as large as possible. This is defined by distance between the platinum thin-film gauges. Each gold paint strip was painted as wide as possible, limited by the gold strip of the next sensor as shown in Figure 5-6. Care was taken such that the strips did not overlap, which would cause an interconnection between gauges and thus a resulting malfunction of both the gauges.

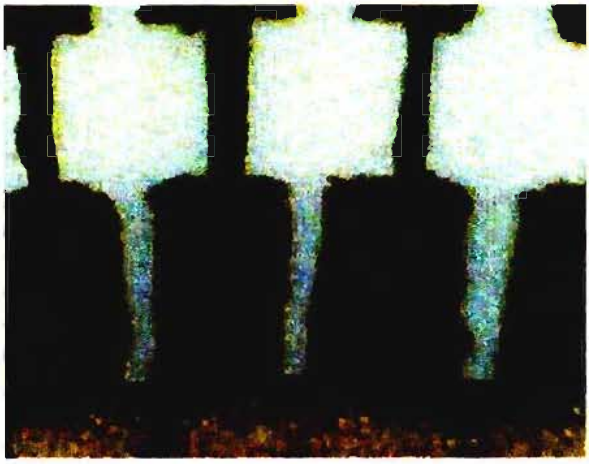

Figure 5-6: Gold strips painted as wide as possible

After the days of painting and baking of the gold strips, each gauge was tested for connectivity and resistance at the holes on the side of the blade (where the gold flying leads would be attached). It was found that most of the sensors lost connectivity at the holes, but were functioning on the surface of the blade. Referring to Ligrani *et al.* (1982), it was noted that painting the gold around sharp corners caused excessive thinning in the layer, and a loss of connection at the point. The thin-film gauges had to be redone, and the sides of the blade were chamfered and smoothed to remove all traces of sharp corners, such that the gold paint could bond well to the surface all around the corner. After running through the painting process of the platinum and gold again, most of the connections functioned perfectly. There were some gold strips that required another layer of paint to function properly.

Once all the gauges were found to be functioning correctly, the final step of the sensor preparation was to lightly polish each gauge with the OPS suspended silica. This was done to raise each resistance to approximately 50 Ω.

As mentioned previously, a few gold leads were lost during the disassembly of the blade stack and wiring, and these were carefully soldered back on. Each gold lead was placed in the corresponding hole on the sides of the test blade in relation to order of the D-type connector. The 96 wires were carefully compacted on the sides of the blade and the test blade was reassembled. Wires that had disconnected at the D-type connections were also soldered back on carefully. The connections of each gauge were checked at the D-type connector and all functioned perfectly. The final instrumented Macor SMR-95 test blade is shown in Figure 5-7.

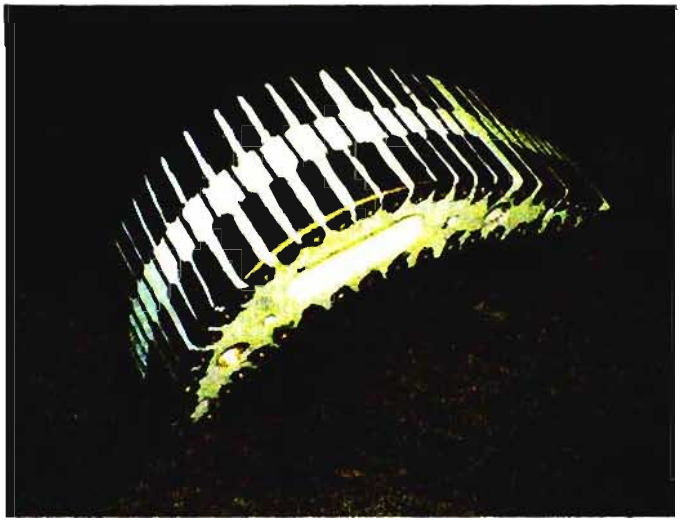

Figure 5-7: Final instrumented blade with thin-film gauges

5.3.3 Thin-Film Gauge Calibration

Once the process of repainting and firing the thin-film gauges was completed and successful, one needed to calibrate each of the sensors to resolve the relationship between the temperature changes and corresponding resistance changes. This data would be needed to calculate the constants of the temperature resistance coefficient α_R, which is needed in the post-processing program to calculate the corresponding isothermal heat transfer coefficients (discussed in Section 3.2.1). The program that utilises these parameter constants is the LabView program "Isotemp1" written by Snedden (1995), the properties of which are given in Appendix D1.2.

The value for α_R is given by equation 3.2.1.18 as $\alpha_R = \frac{1}{R_0}\left(\frac{R - R_0}{T - T_0}\right)$. Thus by calibrating each sensor, one is able to obtain the gradient of the relationship between the temperature and resistance, which would yield the value of the $\left(\frac{R - R_0}{T - T_0}\right)$ term, and R_0 measured at the plunging temperature of T_0 = 40 °C.

The blade was calibrated with Cassie (2006) using a convection oven in the UKZN metallurgy department. It was decided to acquire the resistances at five different temperatures. Instead of just calibrating the sensors with the blade stack placed in the convection oven and measuring the resistances off the D-type connectors, it was decided to implement the entire acquisition system including the selector boxes and heat transfer analogue cards. Thus any resistance in that system would be compensated for in the calibration, and would therefore be a more accurate

measurement. A number of thermocouples were used, connected to a Fluke 52 K/J thermometer. The thermocouples were placed around the oven to get an averaged temperature in the oven that the blade was being exposed to. The resistances of the thin-film gauges were measured using digital multimeters.

The procedure of running the calibration was to first acquire the resistances at ambient temperature. By using the selector box, it was easier and faster to switch between all the resistances for each D-type connector, as opposed to physically measuring the resistance at each pin on the connectors. This process was used for every temperature reading. The oven temperature was raised in 20 °C increments and the resistances checked at each of these intervals, until the oven reached 100 °C.

Once the resistances were recorded for all five temperature intervals, the data was used to calculate the parameter constants α_R and R_0, as well as to judge if there had been any increased sensitivity of the new platinum thin-film gauges compared to the previous set.

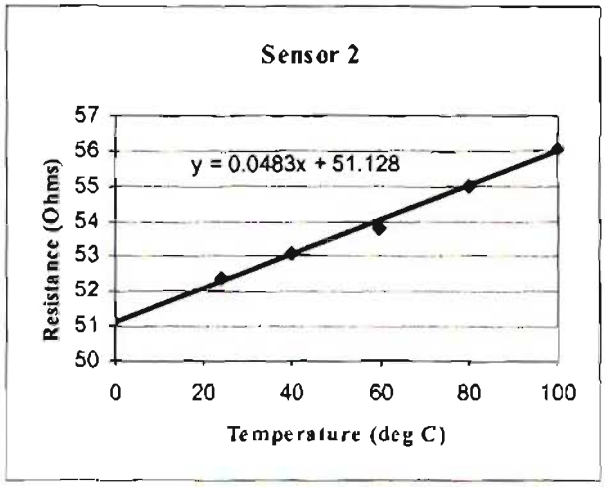

Figure 5-8: Example of a graph plotted from the calibration procedure

After reviewing the calibration graphs for each sensor compared to the previous set of sensors, as shown in Figure 5-8, it was noted that the general trend of sensitivity was followed, without much increase. The fundamental difference between the newly painted platinum and the old sensors was that the resistances were reset to around 50 Ω. One could question the amount of time needed to disassemble the blade stack, repaint and rebake the sensors, and calibrate the gauges, after noticing only a minor increase in sensitivity. The advantage of the whole process was that every sensor was functional, and Cassie (2006) stated there was a noticeable difference in the consistency of results, to be discussed later.

5.3.4 Analogue Boards Calibration

Before testing could commence, the circuitry of the electrical heat transfer analogue boards needed to be calibrated to acquire the values of the constants needed in the post-processing program to calculate the heat transfer coefficient distribution. The constants needed results from the average step response output of the voltages when a parabolic signal is supplied into the system.

This process was relatively straightforward, as the program and procedure had already been tried and tested by Snedden (1995). Two 15 V voltage supplies were connected to the system (to provide 15 V to both the positive and negative terminals) and the PC71 interface card was connected to the inputs. The Pascal program "CAL30" (written by Snedden (1995)) was used to supply the boards with a parabolic signal, as shown in Figure 5-9. The calibration was performed independent of the current source, and the blade stack disconnected from the circuit. The relatively small amplitude parabolic signal was sent into the system, and the resulting output step response was recorded.

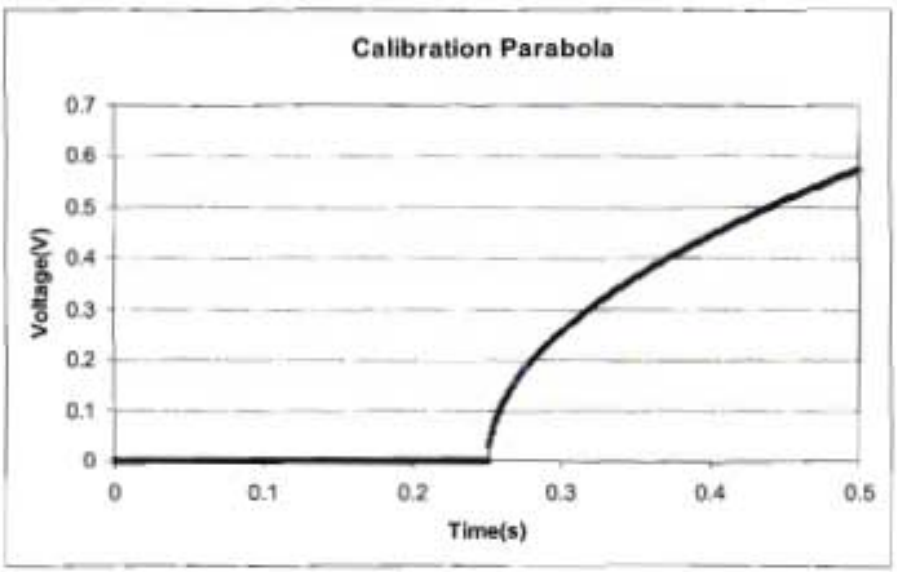

Figure 5-9: Parabolic signal (reproduced from Cassie (2006))

The process was followed for each circuit board, and the data was plotted and calculated in a Microsoft Excel spreadsheet which resulted in output step voltages of amplitudes for the six boards ranging between 2.616 V and 3.107 V, with an example shown in Figure 5-10. This compared to an average step response of 3.110 V of Snedden (1995). Multiple readings were taken and averaged following suggestion from Snedden (1995) that a single reading could prove to be inaccurate due to the noise levels. This slight difference in constant values would affect

the final heat transfer coefficient calculation drastically, and the calibration procedure proved valuable in this regard. Previous students such as De Villiers (2002) assumed no change in the circuit calibration constants and used the values calculated by Snedden (1995).

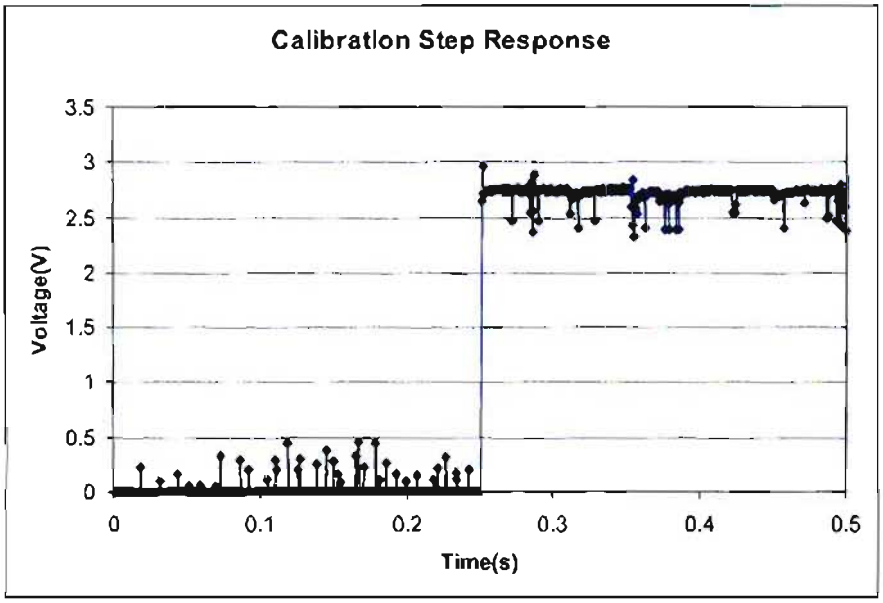

Figure 5-10: Circuit step output voltage (reproduced from Cassie (2006))

5.3.5 Experimental Testing

5.3.5.1 Comparison of Recent Results

Once calibration of the thin-film gauges and heat transfer analogue boards was completed, testing could begin to assess the changes in experimental results.

After testing and post-processing, Cassie (2006) stated that the comparison of the heat transfer coefficient distribution of the blade to the old set showed a significant increase in predictability and consistency, as the old sensors generated an irregular distribution, as indicated in Figure 5-11. It was noted that the procedure for the post-processing of the heat transfer data was as difficult as before, with the electrical noise causing disruptions to the output voltage signal. The minor increase of the sensitivity of the gauges proved to be insignificant in the final data output signal.

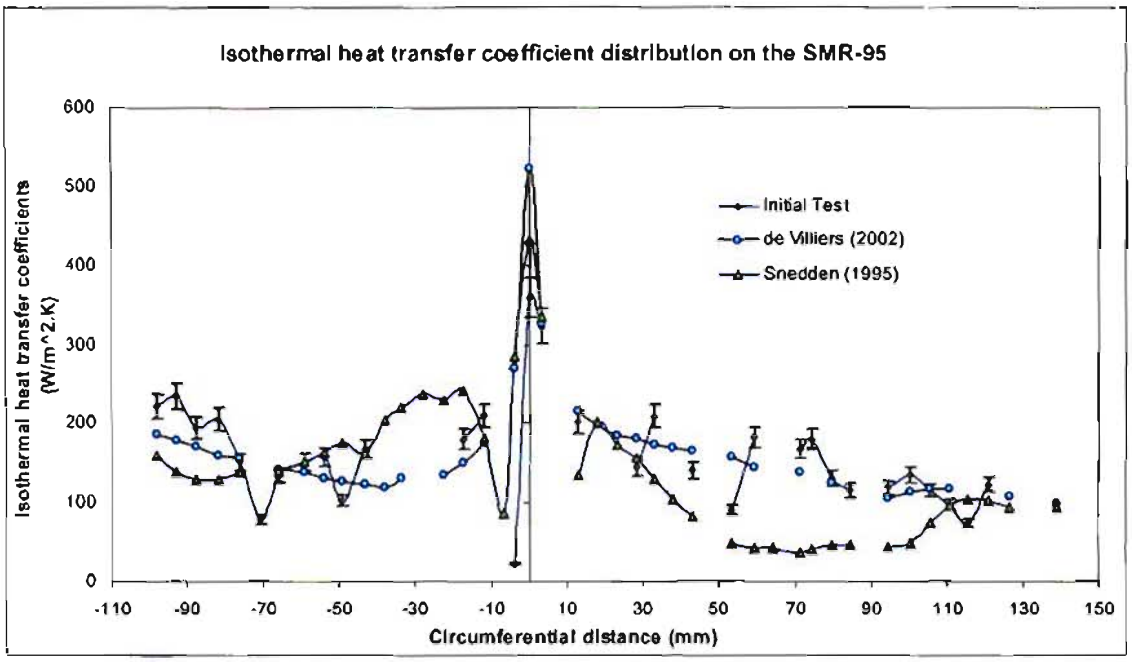

Figure 5-11: Isothermal heat transfer coefficient distribution before re-instrumentation (reproduced from Cassie (2006))

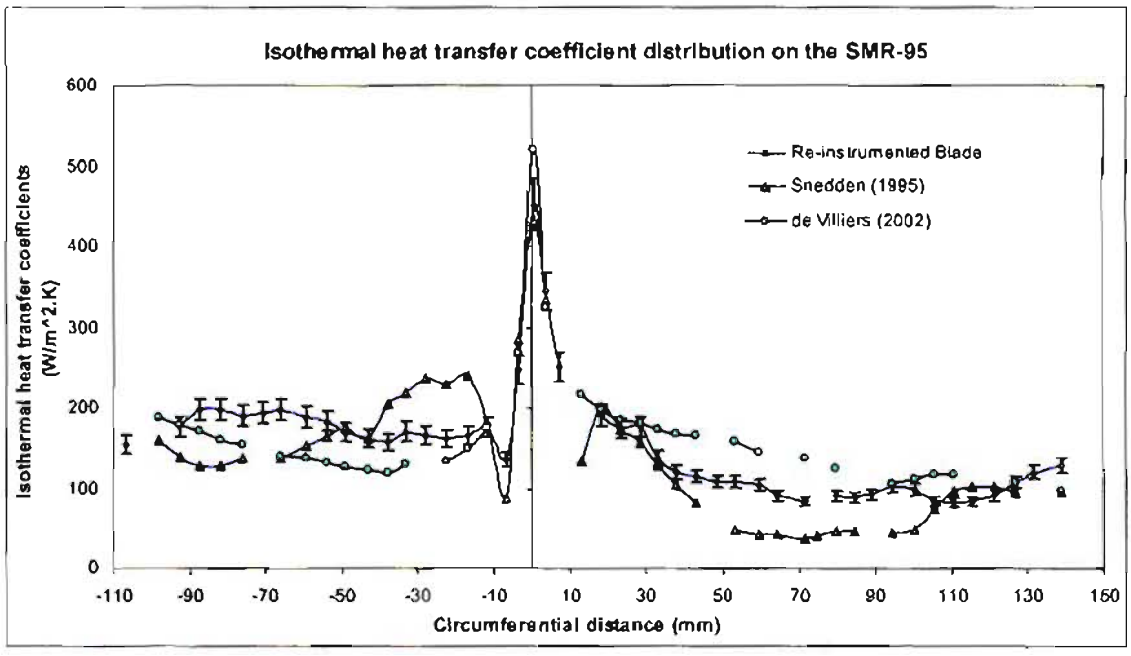

Figure 5-12: Isothermal heat transfer coefficient distribution after re-instrumentation (reproduced from Cassie (2006))

One can see the improvement in consistency and resolution of the results after the initial tests in Figure 5-12, on both the pressure side and suction side of the SMR-95 test blade. The trend of the graph on both the suction side and pressure side differed slightly to that of the results from Snedden (1995) and De Villiers (2002). The explanation for the distribution trend will be

discussed later in Section 5.3.5.4. The accuracy of the heat transfer coefficient distribution was heavily dependent on certain factors, including the operating conditions and the parameters entered into the post-processing program. The effects of entering inaccurate parameters were investigated by Kennedy (2007). During the experimental runs, every parameter needed for the post-processing program was carefully observed. Though similar running conditions were used by previous students, the compressor blade did not stay at a constant speed. This mainly affected the inlet and outlet pressures, and the temperature of the blade. The following tests would need to be conducted carefully, ensuring precise readings of all constants and test values, and maintaining the experimental rig at operating conditions as accurately as possible.

5.3.5.2 INITIAL TESTS

Before experimental testing could commence, the instrumented blade was checked to see if all the available sensors were still working correctly. The sensor responses were tested by using a hot-air gun provided by the UKZN workshop. After numerous tests, there were a number of sensors that inexplicably stopped working. The blade was checked carefully for scratches, since the suspected problem was the actual plunging process of the blade in and out of the cascade. The current plunging system proved to be problematic in the sense that the re-assembly of the blade stack into the cascade could be inaccurate, and the blade could be plunged at a slight angle. The re-assembly of the blade, cascade and pneumatic ram had to be performed in the cramped conditions of the plenum access port, and it was very difficult to line up the blade perfectly straight and centralised. The reason for the angle of the re-assembled blade to be almost perfect is the very small tolerance of the hole shaped around the SMR-95 profile, between the cascade and the cooling box. This is to minimise any unwanted turbulence in that area, to simulate a sealed edge once the blade is plunged into the cascade box. If the blade is not centralised, the plunging and retracting process could lead to the edges of the blade sliding along the cut opening of the cascade box.

This unfortunate process led to minor scratches on the blade upon inspection which, however, did not account for the numerous sensors lost. It was decided to disassemble the entire blade stack again, which revealed disconnected leads at the soldered joints. All these joints were redone properly, and other soldered connections were redone to avoid the chance of a recurring problem.

Once the time-consuming process of reassembling the blade stack was completed, the connectivity of each sensor was checked. There were three sensors that seemed to be damaged

by the plunging process. The blade was assembled carefully in the plenum, and the test could be performed to check the consistency of results with that of Cassie (2006).

Before starting up the experimental rig, the instrumentation was set up. Four thermocouples attached to the inside of the blade stack were set up for monitoring the averaged blade temperature. Two multimeters were connected to record the initial voltages and resistances when it would be time to plunge the blade into the hot-air stream.

The blade stack was attached to the plunging mechanism, and assembled together with the cascade box inside the plenum. The first D-type connector (labelled 'P1') was attached to the heat transfer analogue cards box, and the output voltages were monitored on WaveView. The initial voltages varied around the 0 V line (on a scale of -5 V to +5 V, set via jumpers on the PC 30 A/D card). Each of the eight analogue boards has a built-in DC offset screw, which can adjust the output voltages in either polarity direction at amplitude of around 1.8 V. The voltages were adjusted such that each output reading settled on 0 V.

The instrumentation was set up and testing could commence. The starting and operating procedure of the supersonic cascade rig remained the same as previous years. This step-by-step process was outlined by De Villiers (2002), and can be found in Appendix C1.1. To achieve operating conditions, the compressor blade speed was increased to achieve a higher operating temperature. The speed is manually controlled in the neighbouring room with the hydraulic motor, as described in Section 4.2.3. The speed of the compressor blade does fluctuate slightly with time, and must be constantly monitored to maintain operating conditions. This process is vital, since the procedure must be repeated for all six of the D-type connectors and waiting for the blade temperature to cool between plunging.

Once the plenum temperature reached 100 °C, the compressor blade speed was reduced from the maximum of 3 000 rpm down to the operating speed of 2 500 rpm. The water flow rate through the annular radiator was increased to cool the air flowing in the plenum, and balanced to maintain the temperature of 100 °C as accurately as possible.

During the period of setting the plenum to operating temperatures, the blade was left to cool in the cooling box. The temperature inside the cooling box inevitably increased due to losses and heat transfer from the air inside the plenum. This temperature increase was kept to a minimum by the cooling circuit and blower. Once the temperature of the blade reached 40 °C, the instrumentation was set up to record the heat transfer data just before plunging. The resolution of data points was configured in WaveView to capture for three seconds at 4 000 Hz, which was

activated almost immediately after plunging the blade into the hot-air stream using the pneumatic ram. Just before plunging, the blower was switched off to avoid any additional electrical noise in the data output, as well as recording the initial voltages, resistances and pressures needed for the post-processing program. The heat transfer data was outputted as a text file to be analysed later.

The blade was then retracted immediately back into the cooling box, and left to cool to the desired temperature of 40 °C. The process was repeated for each D-type connector, and after many hours of testing, sufficient data was captured for every sensor on the blade to analyse in the post-processing program in LabView, and the rig was shut down and reviewed for any leaks or damages. It was noted that there was a large oil leak in the hydraulic drive motor, which was concerning for future experimental runs.

5.3.5.3 POST-PROCESSING

With the data captured for P1 to P6, the post-processing program "Isotemp1" was executed and the data loaded. A number of teething problems and recurring errors arose when running the program. The solutions to these problems were given by De Villiers (2002), which basically involved a correct sequential procedure to enter in the data, as discussed in Appendix 6 of the dissertation of De Villiers (2002). The procedure to generate isothermal heat transfer coefficients from the program was also discussed, which proved useful. The first step of analysing the data was to filter the results using the software filters. The main filters used were Chebyshev and Chebyshev II, and most of the noise was filtered out by adjusting the cut-off frequencies as shown in Figure 5-13 and Figure 5-14.

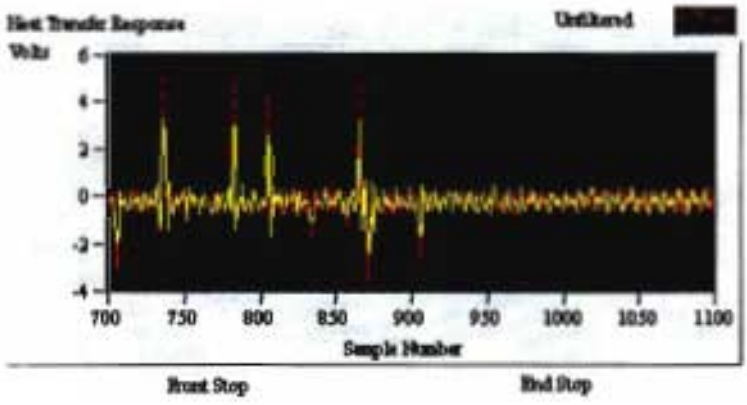

Figure 5-13: Unfiltered data trace

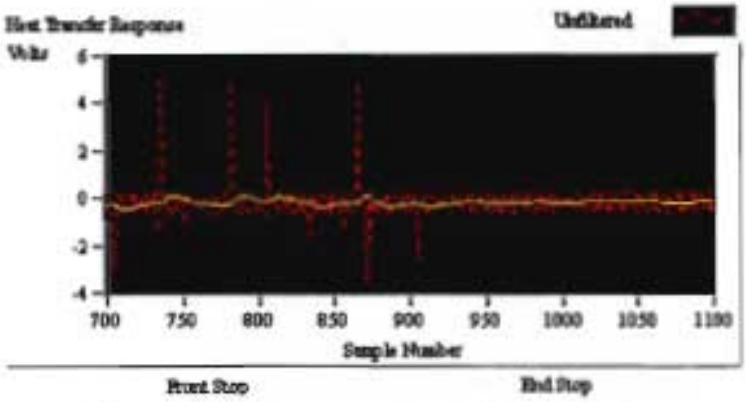

Figure 5-14: Data trace after sufficient filtering

The location of the voltage step in the signal had to be isolated to achieve the desired results. This section was described in Ligrani *et al.* (1982) and mentioned by De Villiers (2002) as from the portion just before the voltage step. The ends of the signal were defined by the minimum length required by "Isotemp1", as isolating a small section resulted in the error of "Number of Samples > 0". The length of the localised signal did not seem to affect the final heat transfer coefficient calculation after numerous attempts.

It was noted that the sample time of three seconds resulted in the data signal just barely of a sufficient length. In following experiments, the sample time would be set to five seconds, and the frequency doubled to 8 000 Hz as a precaution to avoid any errors. The voltage step response that was isolated can be seen in Figure 5-15, as well as the noticeable noisy signal that had been filtered.

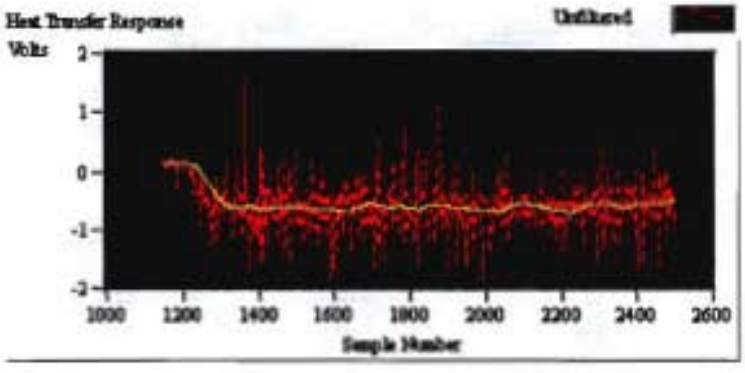

Figure 5-15: Localised signal including the voltage step

This result compared favourably to that of Snedden (1995), who reported a general voltage step change of around 1 V in amplitude. Once every data signal was filtered and adequately localised for each sensor, the next screen prompt was to enter all the calibration constants and initial operating conditions for each sensor recorded. These values were accurately measured and observed before testing could commence, and they were entered into the program.

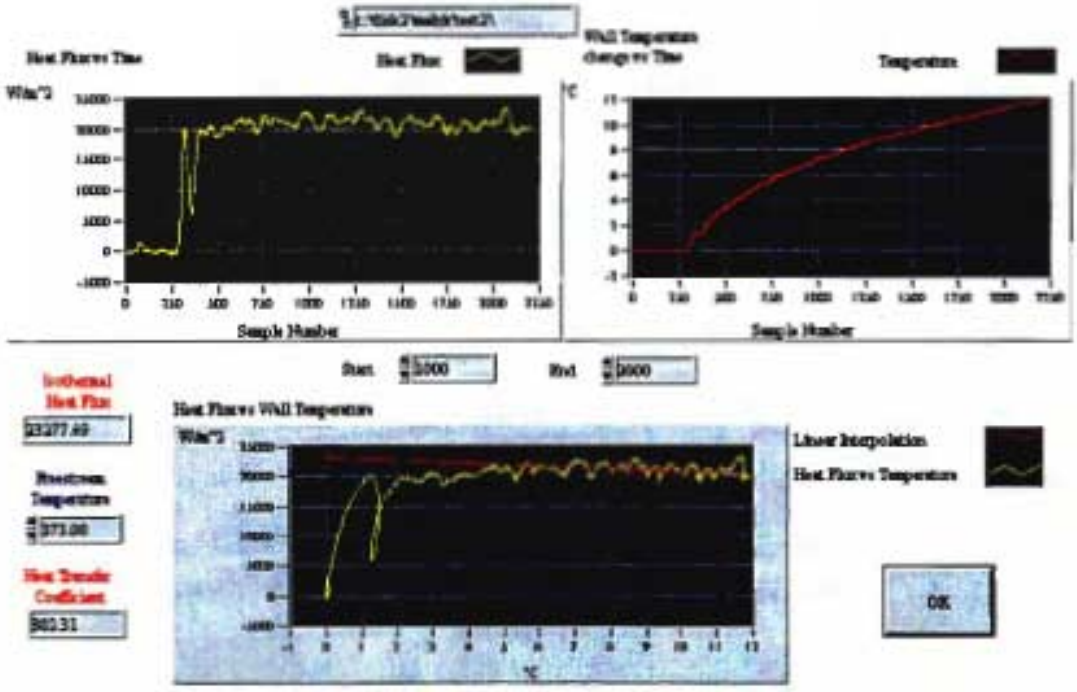

Figure 5-16: Calculation of heat transfer coefficient in LabView

The final graph window shown in "Isotemp1" was to analyse the data entered and commence with the conversion of heat flux, reconstruction of the wall temperatures and, with the aid of the user, to calculate each isothermal heat transfer coefficient.

The graphs calculated and drawn by the program must be analysed by the user to generate the correct heat transfer coefficient. This is done by judging the straight line portion of the graph of Heat Flux vs. Wall Temperature, as shown in Figure 5-16. This best-fit line is projected back to where it intersects with the *y*-axis, and the isothermal heat flux is calculated. This method is described by Ligrani *et al.* (1982). The process is repeated for every sensor on the blade, and the data was entered into an Excel spreadsheet. The isothermal heat transfer coefficients were calculated by dividing the heat flux values by the change in temperature between the blade wall and freestream hot air.

Once every heat transfer coefficient was calculated for every associated working sensor, the values were plotted using the circumferential distances of the sensors on the blade, and the heat transfer coefficient distribution was drawn.

5.3.5.4 RESULTS ANALYSIS OF TU = 3%

As shown in Figure 5-17, the heat transfer coefficient distribution was of a similar trend, except the overall magnitude was lower than that of Cassie (2006).

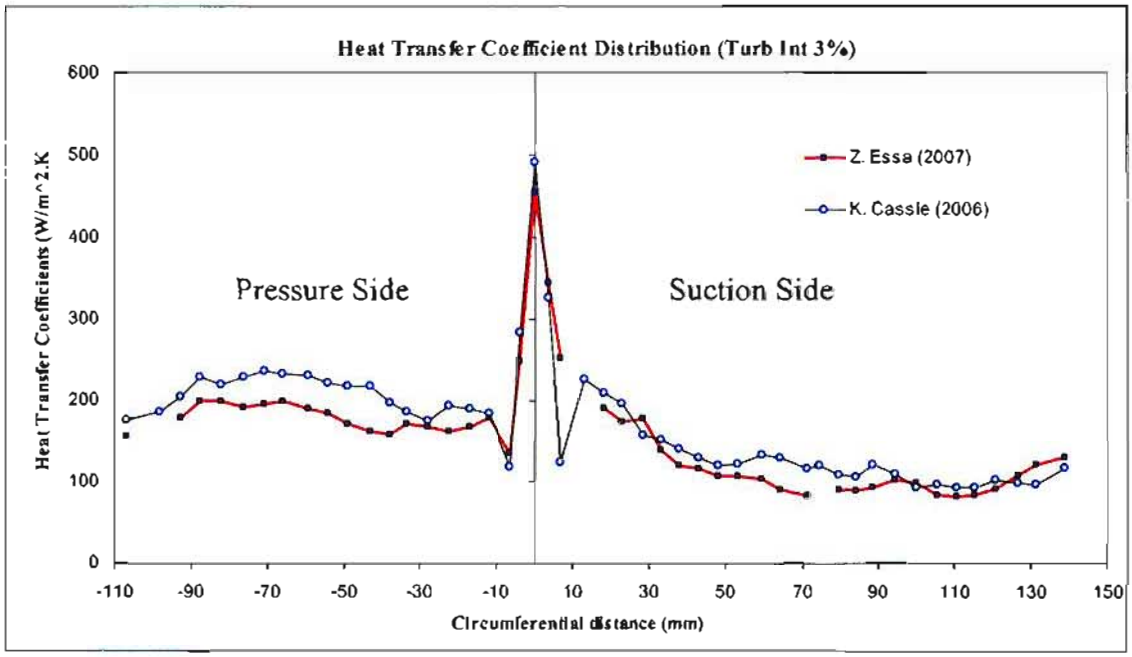

Figure 5-17: Heat transfer coefficient distribution after reassembly

The three missing points on the distribution curve accounts for the three broken sensors. The highest intensity of heat transfer occurs at the leading edge of the blade (0 mm circumferential distance), where there is an increase in heat transfer due to the stagnation zone of air flow. This value of around 453 W/m^{2}K compares to that of 495 W/m^{2}K of Cassie (2006). This discrepancy is also evident in results from de Villiers (2002), whose highest value of heat transfer at the leading edge was around 490 W/m^{2}K, compared to experiments run at the CSIR (1998), which yielded its highest heat transfer value in the area of 440 W/m^{2}K. The results also compare favourably to that of Stieger's (1998), whose highest heat transfer reading at freestream turbulence was around 425 W/m^{2}K.

The heat transfer rapidly decreases to its lowest level on the pressure side, close to 10 mm circumferential distance at 136 W/m^{2}K, before increasing again to 177 W/m^{2}K. This is indicative of a separation bubble also observed by Stieger (1998), who reported a drop in heat transfer of coefficient value of below 100 W/m^{2}K as shown in Figure 5-18.

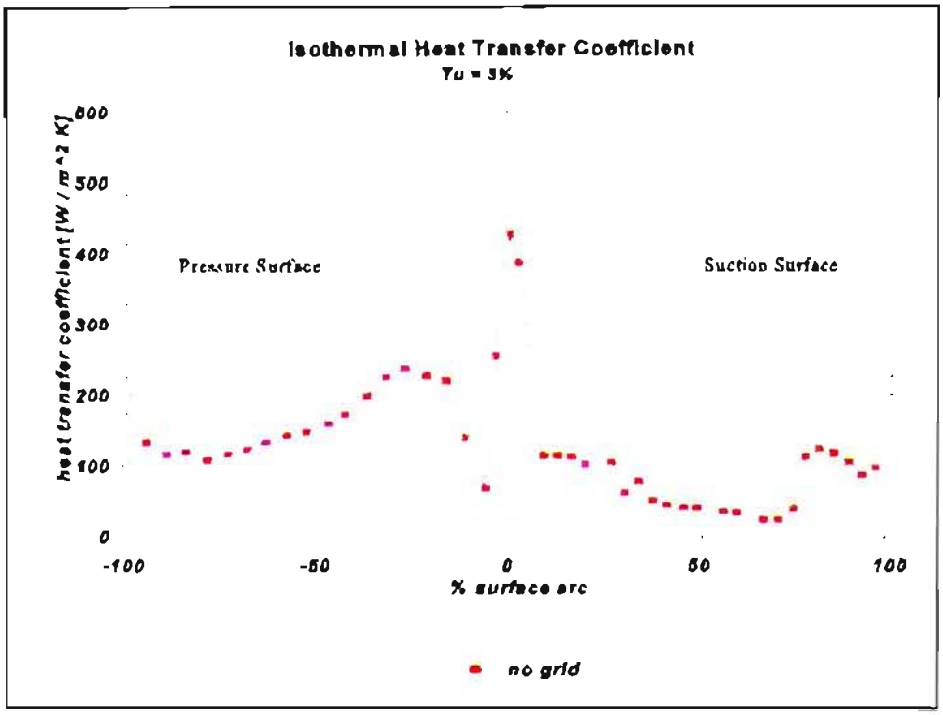

Figure 5-18: Heat transfer coefficient distribution of Stieger (1998) at Tu = 3%

This is believed to be caused by the acute change in curvature of the SMR-95 blade profile, with the change occurring on both the pressure and suction sides. It is thus to be expected that another separation bubble would form on the suction surface just after the leading edge, which causes the flow separation and a drastic drop in heat transfer. Other blade profiles may not exhibit this phenomenon if there is a less acute angle change on either the suction or pressure side of the leading edge.

After the turbulent reattachment of the flow on the pressure side, the heat transfer increases steadily to around 200 W/m^2K as the velocity of the air increases. This slowly begins to drop off as the air passes to the trailing edge of the turbine blade.

On the suction side, the heat transfer drops drastically from the leading edge. The expected separation bubble on the 10 mm suction side could not be seen, however, due to the broken sensor at this point. The trend shown by Cassie (2006) and Stieger (1998) showed a drastic drop in heat transfer at this point before increasing again. This is again due to the separation bubble that forms due to the separation of flow, and turbulent reattachment thereafter, similar to the trend shown on the pressure side. The point where heat transfer increases again (around 90 mm circumferential distance) compares to the point of pressure recovery on the pressure distribution plot, as also observed by De Villiers (2002), described as the air flow leaving the throat section of the blade passage. This is indicative of a shockwave at this point, investigated and illustrated by Stieger (1998) as shown in Figure 5-19, and a turbulent reattachment of the flow which increases the heat transfer slightly.

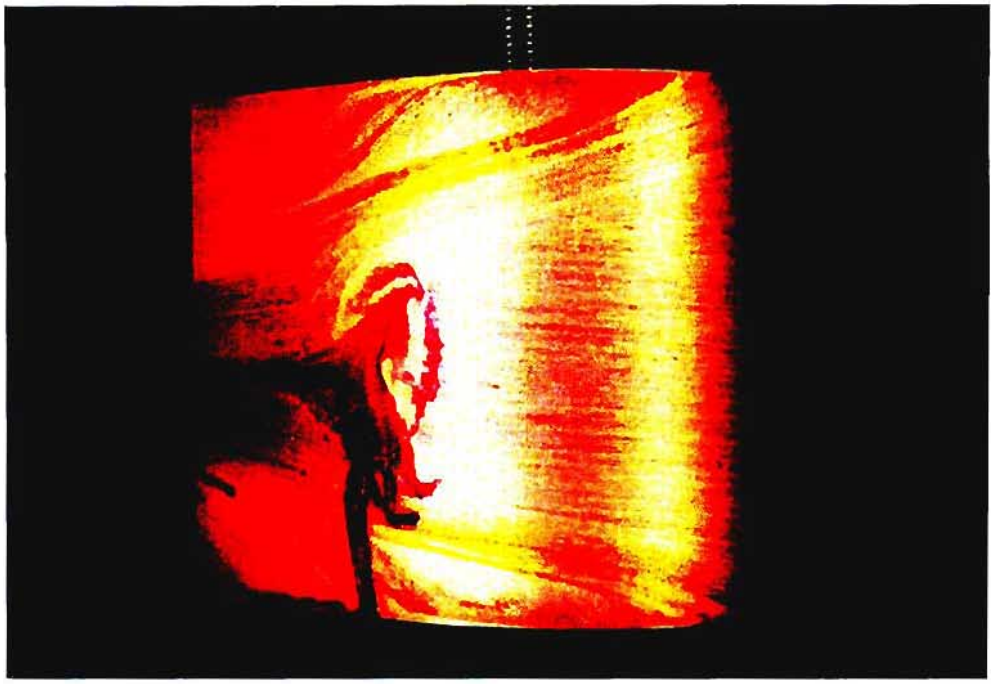

Figure 5-19: Separation bubble on suction surface illustrated by flow visualization (reproduced from Stieger (1998))

The changes in heat transfer as the air flow increases in velocity are not as sharp compared to the pressure side. This is due to the flow acceleration being less. The heat transfer rate remains relatively stable until 110 mm circumferential distance, before increasing slightly as it gets to the trailing edge of the blade.

After reviewing previous results from students that have worked on the project, it can be seen that a similar trend is followed, with small discrepancies of the magnitude of heat transfer coefficients. This can be due to various compounding errors that have contributed to the final values of magnitude. Firstly, the newly painted thin-film gauges had no significant increase in sensitivity, thus the issue of the noisy voltage traces still posed a problem. The data entered into the post-processing program could possibly have not been accurate enough, with some values previously been assumed to be constant, or certain values averaged. Significant changes in final results were noted with slight changes of parameter values.

Another major contributing factor that has always been a problem in the project's span was the inconsistent operating conditions. As discussed, maintaining exactly the same operating conditions for the experimental runs was almost impossible, with the fluctuating compressor blade speed and varying pressures and temperatures. These varied over the span of testing six sets of sensors after a period of hours. The resolution of data capturing was not sufficient, and

this could lead to slight discrepancies in the resulting output values. Ideally one would want every sensor to be sampled at the same time to have consistent operating conditions. However, the current data acquisition system only allows for eight sensors to be sampled at a time. For there to be simultaneous readings for all 48 sensors, the data acquisition would have to include 48 heat transfer analogy boards, and multiple A/D sampling boards, which is impractical. Improvements in numerical data acquisition techniques have been discussed in Section 2.3.6 of Chapter 2, and this would be the most realistic replacement of the current physical electrical analogue circuitry.

In previous years, the experimental rig had been set up by Snedden (1995) and Stieger (1998) to test the effects of different levels of turbulence intensities on the heat transfer of the turbine blade. The two main turbulence intensities investigated were 15% and 25.5% using a grid of rods of different diameters, as described in Section 4.3.3 of Chapter 4.

5.3.5.5 RESULTS ANALYSIS OF TU = 15%

To set the supersonic cascade for turbulence testing, one had to disassemble the cascade box from inside the plenum. The installation of the grid was straightforward and just required the rods to be slotted into the existing holes in the cascade box (covered with thin tape during freestream tests to ensure smooth walls). The grid was bolted tight, and the cascade box was placed carefully back into the plenum and reattached to the pneumatic ram and diffuser.

After many hours of testing, the previously noted problem of the leaking oil from the hydraulic motor worsened. Upon consultation with previous students of the project, it seemed the problem had occurred before and there was insufficient finance to replace the drive, or even repair it. The short-term solution was to just refill the oil after every run and constantly monitor the problem. Any failure of the hydraulic drive could potentially lead to heavily damaged equipment. It was also noted how much longer it took the plenum to reach the desired level of vacuum pressure, indicating that the vacuum pump would need servicing in the future.

The same procedure was used to acquire the data for the new test, and the final heat transfer coefficient distribution can be seen in Figure 5-20.

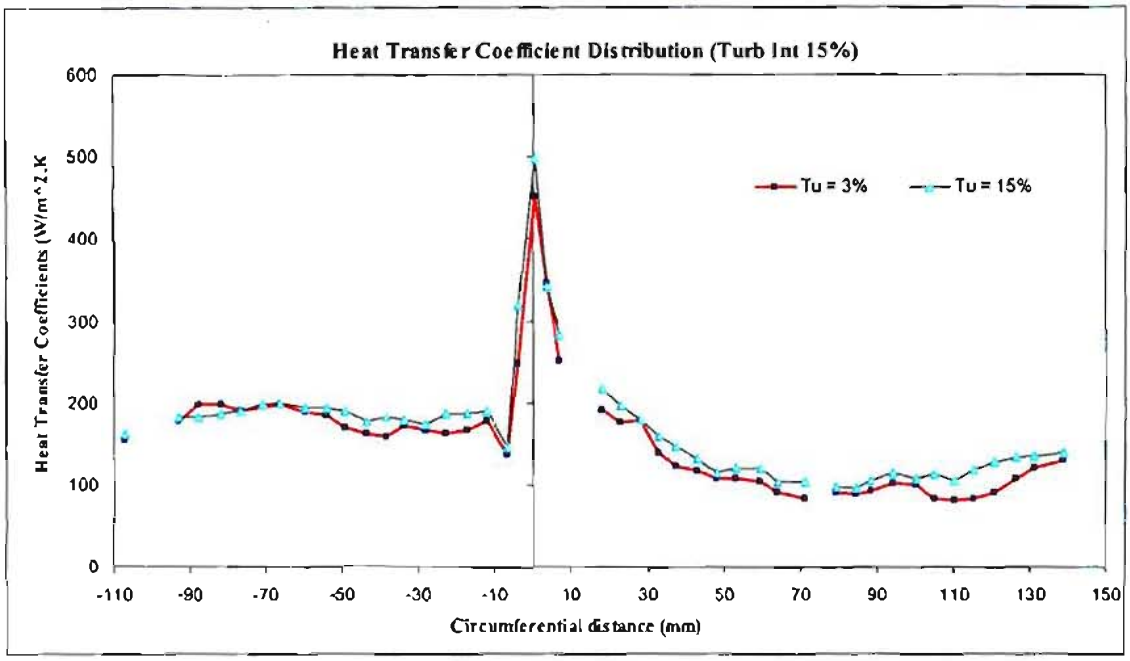

Figure 5-20: Heat transfer coefficient distribution for Tu = 15%

Upon reviewing the distribution compared to that of the freestream case (Tu = 3%), one can see the general increase in heat transfer all along the blade profile. The drop in heat transfer close to 10 mm circumferential distance on the pressure side shows the separation bubble existing for the turbulence intensity of 15%. The general trend is followed on the suction side, although there is an obvious increase in heat transfer from the Tu = 3% case is visible.

The broken sensor close to the leading edge prevents a full understanding of the possible separation bubble at this point, although the result of Stieger (1998) shows the drop in heat transfer around 10 mm circumferential distance which indicates that a separation bubble has formed, as can be seen in Figure 5-21.

One can see the stability of the distribution at around 110 mm circumferential distance as compared to the drop in heat transfer of the freestream case, which shows that the increase in turbulence intensity has minimised or eliminated the existence of the separation bubble that had occurred.

Upon reviewing the flow visualisation tests of Stieger (1998) as shown in Figure 5-22, the absence of the separation bubble can be seen (no disturbance in the flow), which is in agreement with the heat transfer coefficient distribution trend. The actual distribution of Stieger (1998) for the case of Tu = 15% shows a similar result and increase from his base test condition of freestream turbulence, as illustrated in Figure 5-21. The highest level of heat transfer is shown to be around 495 W/m^2K, comparing very well with the current test performed, which resulted in a heat transfer coefficient of 498 W/m^2K at the leading edge.

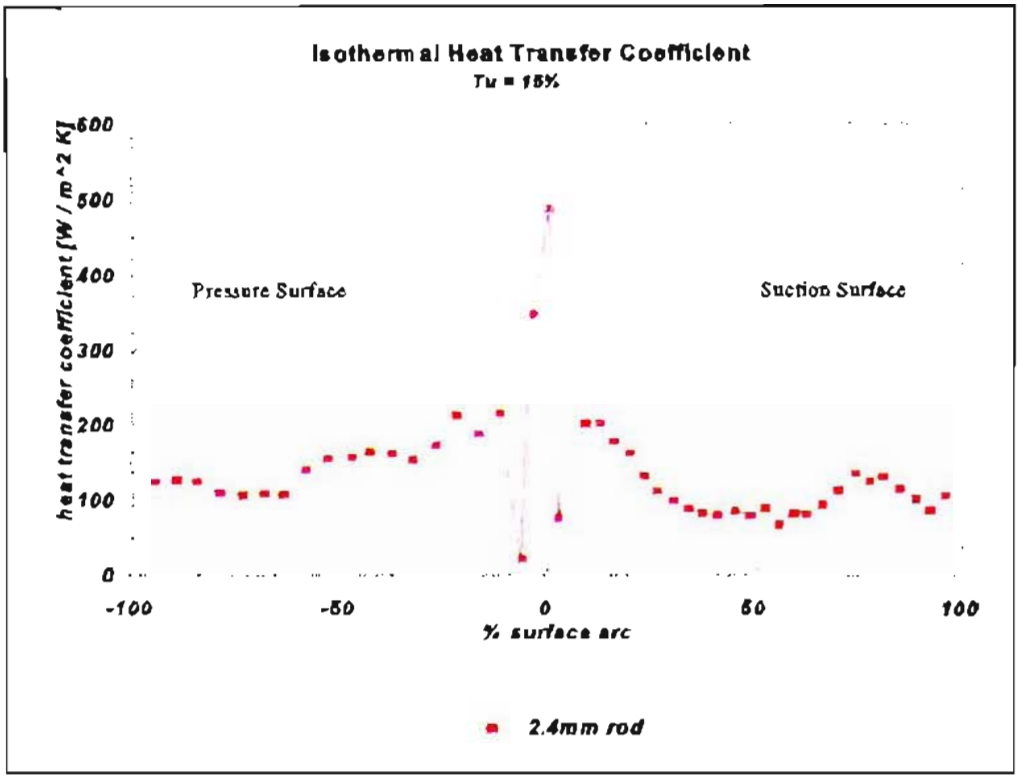

Figure 5-21: Heat transfer coefficient distribution of Stieger (1998) at Tu = 15%

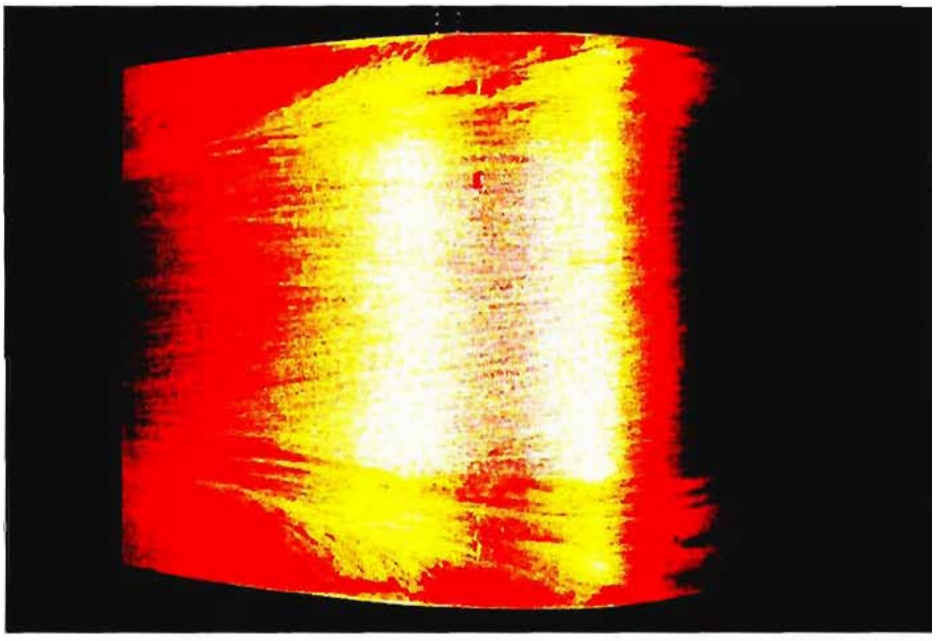

Figure 5-22: Flow visualisation test at Tu = 15% shows the absence of the separation bubble (reproduced from Stieger (1998))

The overall gain in heat transfer for Tu = 15% from Tu = 3% is an average of 6.2% on the pressure side, and 16.1% on the suction side.

5.3.5.6 RESULTS ANALYSIS OF TU = 25.5%

To install the turbulence intensity rods of 25.5% intensity, the same procedure as the 15% turbulence intensity was used. The cascade was dismantled and the old grid removed and covered with thin tape. The larger holes for the new rods were uncovered, and the grid was slotted into place and bolted tight. The cascade box was reassembled in the plenum, and instrumentation set up for another experimental run.

The oil leak in the hydraulic drive, which was monitored during testing, deteriorated further during the procedure. Towards the end of testing, the problem was at the point where the oil had to be refilled after every plunge. This would compromise the accuracy of the final results, as the period for each test was lengthened and base test conditions would be difficult to maintain. Other minor problems with the circuitry and sliding mechanism were encountered, but were easily restored. These problems and other problems encountered on the supersonic cascade facility will be discussed later. Data was acquired from every working sensor, however, and the heat transfer coefficient distribution calculated and drawn as shown in Figure 5-23.

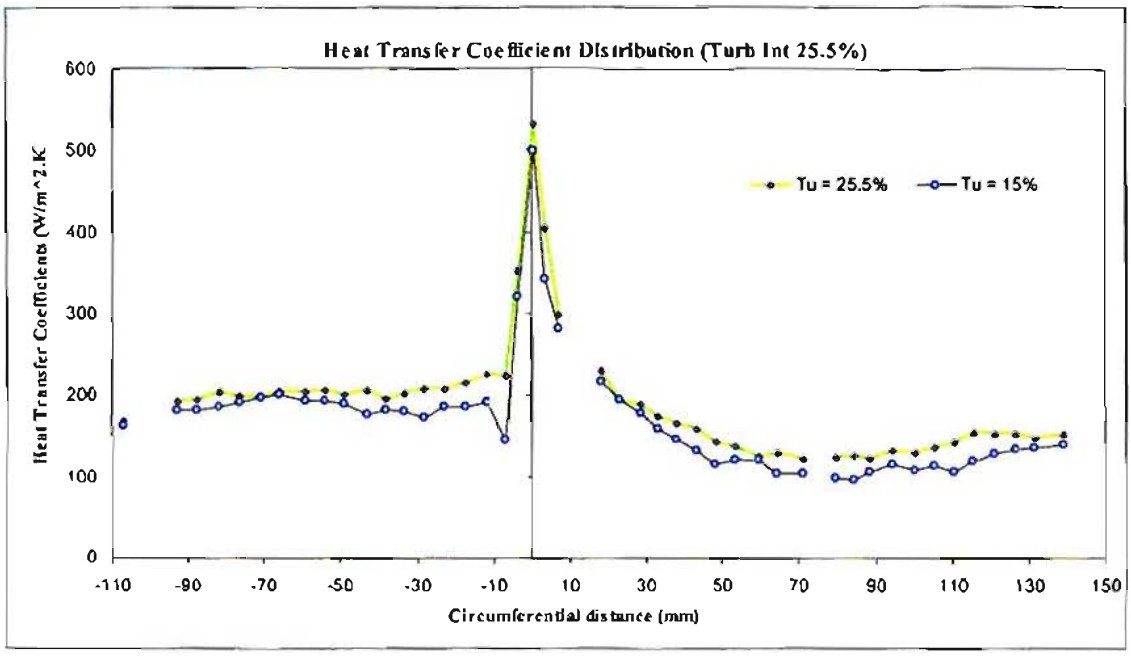

Figure 5-23: Heat transfer coefficient distribution for Tu = 25.5%

With the turbulence intensity significantly increased from the first test condition of freestream turbulence (Tu = 3%), there is a visibly large increase of heat transfer all along the blade profile. As a comparison to the distribution for Tu = 15%, one can see more of an increase of heat transfer near the leading edge of the blade for the distribution of Tu = 25.5%. The separation bubble that occurred at around 10 mm circumferential distance on the pressure side seems to

have diminished, with less of a drop in heat transfer as compared to both the 3% and 15% turbulence intensities. The value of the heat transfer coefficient at the leading edge of the blade for Tu= 25% was 532 W/m^{2}K. This compares to the value of around 550 W/m^{2}K from the results of Stieger (1998). His heat transfer coefficient distribution increase was similar as well, as can be seen in Figure 5-24. The main points to note are the fact that the separation bubbles on both sides near the leading edge still existed, however, were less pronounced compared to the results of the lower turbulence intensities.

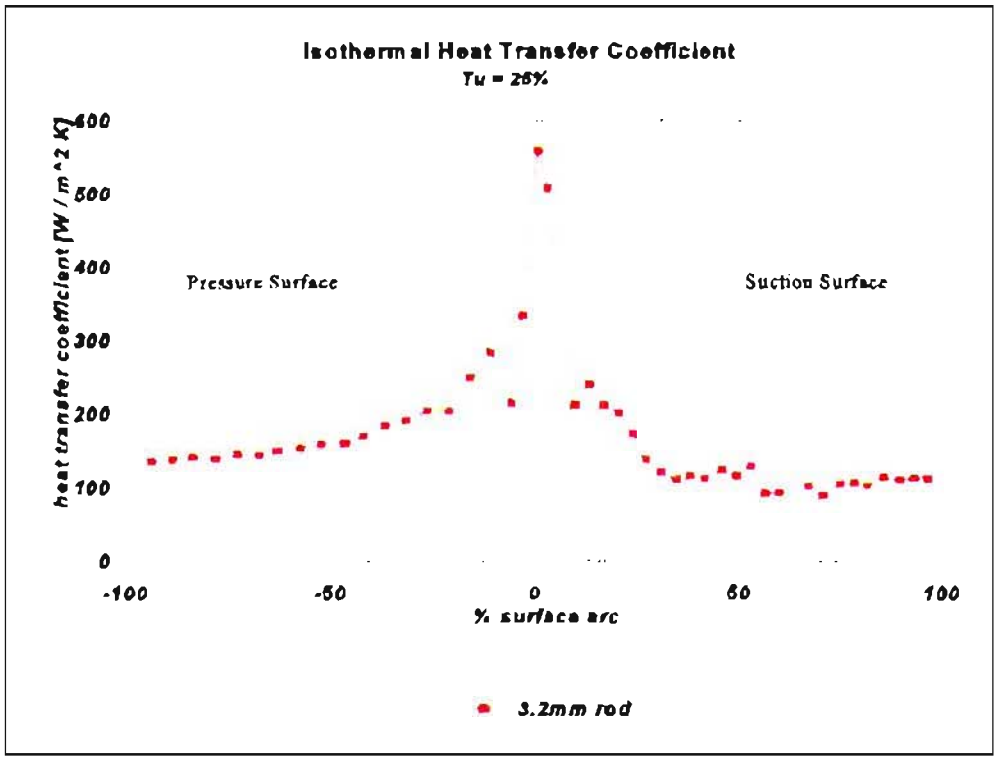

Figure 5-24: Heat transfer coefficient distribution of Stieger (1998) at Tu = 25.5%

The distribution on the suction side of the blade showed a similar trend to that of the Tu = 15% case, with no separation bubble forming near the trailing edge, and a general overall increase in heat transfer. The overall gain in heat transfer for Tu = 25.5% from Tu = 3% is an average of 18.6% on the pressure side, and 35.4% on the suction side.

This trend was in full agreement with that of Stieger (1998), and proved the consistency of the rig, procedure of obtaining results and the data acquisition system. Although the equipment was old and many major improvements could be made to the system, the heat transfer coefficient distribution was of a similar trend, and demonstrated the reliability of the technique.

The heat transfer coefficient distributions for the cases of 3%, 15%, and 25.5% turbulence intensities that were measured were plotted, as shown in Figure 5-25.

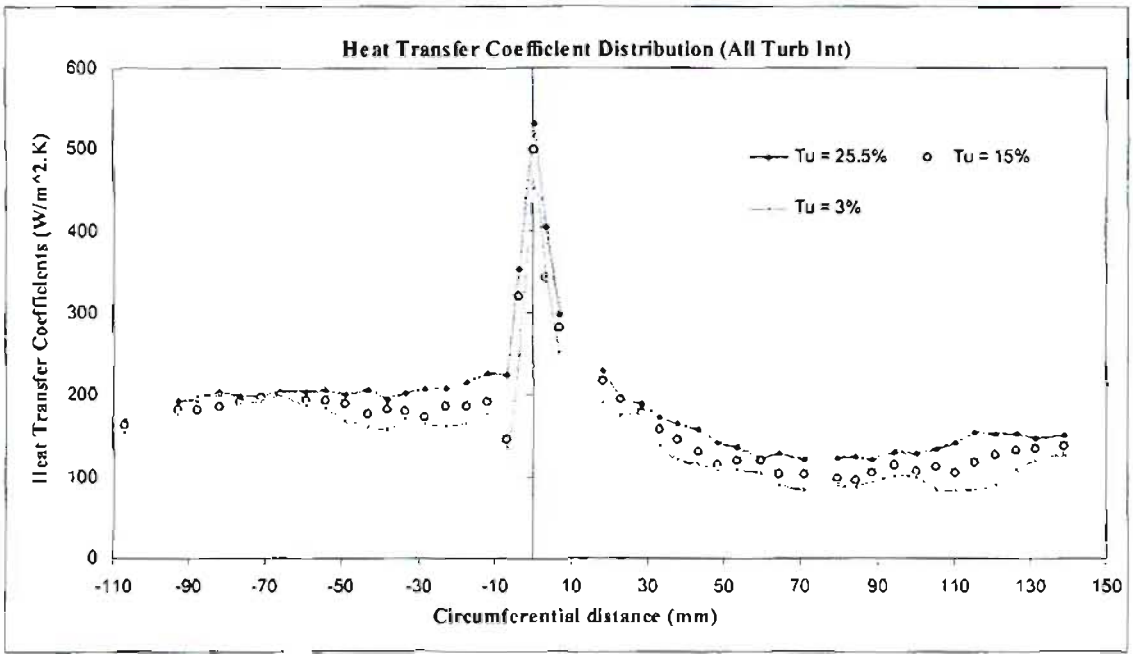

Figure 5-25: Heat transfer coefficient distributions for all measured turbulence intensities

For each level of increased turbulence intensity, the resulting increase in overall heat transfer can be seen along the entire profile of the SMR-95 turbine blade. The largest step of increased heat transfer visible is that of the case for Tu = 25.5%. A theoretical uncertainty analysis (Kline and McClintock method) was conducted by Snedden (1995) who used the same equipment and acquisition method. It was shown to be around 10%, with the calibration processes and temperature change being the highest contributing factors to the uncertainty. It was noted at the increased experimental uncertainty at higher turbulence levels, which were described to be higher than 30% past the 70% chord length due to the unpredictable nature of the shockwaves and turbulence.

The heat transfer results for each turbulence intensity reading were discussed, and a numerical comparison needed to be performed using the commercially available CFD package of FLUENT.

CHAPTER 6

NUMERICAL HEAT TRANSFER PREDICTION

6.1 OVERVIEW

Computational Fluid Dynamics (CFD) is an effective method to save testing time and the costs involved with experimental procedures and operations. The numerical codes have vastly improved over the past few decades, and the flow prediction is somewhat accurate provided the correct conditions and an accurate model are used. These predictions can never take into account every phenomenon that can occur, especially with turbulent flows, but the analysis gives a relatively accurate idea of the characteristics involved and the resulting flow conditions.

The numerical models need to be worked on by validating the results with that of experimental work. Once it is judged that the code can predict correct results with relative accuracy, the models can be adjusted for improvement and analysed, knowing the outcomes of such changes would be a fair reflection of what would occur if those changes were made in applications and thus saving time and money. Although it cannot be assumed to be fully accurate, the results can be used to improve real conditions and testing as a prediction of the flow that would most probably occur. Modifications and tests can be made, thus improving the general outcome in terms of finance and time.

The supersonic cascade experimental rig was used to analyse the data for turbulent flow conditions, and these results could be used to validate the results from the modelling in FLUENT. The cascade box was modelled using a 2-D model and the SMR-95 blade geometry coordinates. The geometries drawn by De Villiers (2002) were used, as the cascade box used for testing was the same. The mesh that was used was improved and refined slightly, and investigations were done on heat transfer on the turbine blade for the various levels of turbulence intensity.

6.2 SOLVERS AND TURBULENCE MODELS

6.2.1 INTRODUCTION

Before stating options and conditions in FLUENT, there are a number of specifications, equations and models that need to be identified in order for the results to be an accurate representation of the system being modelled. The system conditions are solved by using governing equations describing the fluid flow, which are converted to discrete equations that are solved iteratively. The governing equations are Navier-Stokes equations that describe the conservation of mass, momentum and energy. To solve the flow dynamics within the specified domain, the governing equations are integrated over a finite amount of cells of which the region is divided into. This method of using discretised control volumes, or grids and meshes, can be constantly improved and refined by certain methods within the FLUENT program.

Certain terms in the equations are accounted for by specifying a sufficient number of boundary conditions such that the equations can be solved by iteration. By using the RANS equations (described in Section 2.4 of Chapter 2), the method of generating solutions can be described by either a segregated solver, or a couple solver. A number of turbulence models are available in FLUENT, each with their own characteristics and specific to a certain type of system. The choice of turbulence model would depend on considerations such as the physics encompassed in the flow, the level of accuracy needed, the available computational resources and the amount of time available to run the simulation. The program incorporates both one-equation and two-equation models and is listed below.

- Reynolds stress model (RSM)
- Large eddy simulations (LES)
- Spalart-Allmaras model
- k-ε models
    - Standard k-ε
    - Realisable k-ε
    - Renormalisation group k-ε (RNG)
- k-ω models
    - Standard k-ω
    - Shear stress transport k-ω (SST)

As described in Section 2.4, the Reynolds stress model and large eddy simulation methods were impractical in the scope of the project due to their resource-hungry and time-consuming characteristics. The models described in the following sections are summaries of the full descriptions given in the FLUENT user manuals.

6.2.2 SPALART-ALLMARAS (ONE-EQUATION MODEL)

The Spalart-Allmaras model available in FLUENT is a one-equation model used to solve one turbulent transport equation. It was designed for the turbomachinery and aerospace industry, which involves wall-bounded flows. The model is utilised for a low Reynolds number, thus the viscous affected region of the boundary layer would need to be solved. Being specific to systems and boundary layers with adverse pressure gradients and transonic flow over blade profiles, this model suited the flow of the SMR-95 blade profile. From the FLUENT online manuals, the Spalart-Allmaras model is most effective if the region is meshed correctly, specifically the near-wall region mesh spacing.

6.2.3 TWO-EQUATION MODELS

Two-equation turbulence models are one of the most common types of turbulence models used in industry, such as the k-ε and k-ω models. Two-equation models have an extra two transport equations to represent the turbulent characteristics and properties of the specified flow, and thus can account for history effects such as convection and diffusion of turbulent energy.

The transported variable of turbulent kinetic energy, k, is coupled together with a second transported variable. The two that were used with FLUENT were that of turbulent dissipation rate ε, and the specific dissipation rate of ω. This second variable determines the scale of the turbulence, namely the length-scale or time-scale. The variable k determines the energy in the turbulence.

These two models have a number of variances in FLUENT, which are available to suit a number of different flow conditions that the user would deem suitable.

6.2.3.1 k-ε TURBULENCE MODELS

The k-ε models in FLUENT are available in three variations, namely the Standard k-ε model, Realisable k-ε model, and the Renormalisation Group k-ε model (RNG). All three models have similar forms, with transport equations for k and ε. The major differences in the model are as follows:

- The method of calculating turbulent viscosity.
- The turbulent Prandtl numbers governing the turbulent diffusion of k and ε.
- The generation and destruction terms in the ε equation.

The standard k-ε model is the most widely used in industry, since it was proposed by Launder and Spalding (1972). It has a reasonable accuracy for a broad range of turbulent flows which makes this semi-empirical model popular. As the advantages and disadvantages of the standard k-ε model have become known, improvements have been made to the model to improve its performance in the form of its variants of the RNG k-ε model and the Realisable k-ε model. These disadvantages include poor performance in flows where there is a large stream line curvature and strong separation. The RNG k-ε model was derived using a rigorous statistical technique (called Renormalisation Group theory). It has a similar form to the standard k-ε model, but includes the following refinements:

- The RNG model has an additional term in its ε equation that significantly improves the accuracy for rapidly strained flows.
- The effect of swirl on turbulence is included in the RNG model, enhancing accuracy for swirling flows.
- The RNG theory provides an analytical formula for turbulent Prandtl numbers, while the standard k-ε model uses user-specified, constant values.
- While the standard k-ε model is a high Reynolds-number model, the RNG theory provides an analytically derived differential formula for effective viscosity that accounts for low Reynolds-number effects. Effective use of this feature does, however, depend on an appropriate treatment of the near-wall region.

These features make the RNG k-ε model more accurate and reliable for a wider class of flows than the standard k-ε model. The realisable k-ε model is a relatively recent development and differs from the standard k-ε model in two significant ways. The realisable k-ε model contains a new formulation for the turbulent viscosity, and a new transport equation for the dissipation rate ε has been derived from an exact equation for the transport of the mean-square vorticity fluctuation.

The term "realisable" means that the model satisfies certain mathematical constraints on the Reynolds stresses, consistent with the physics of turbulent flows. Both the standard k-ε model and the RNG k-ε model are not realisable.

An instant advantage of the realisable k-ε model is that it more accurately predicts the spreading rate of both planar and round jets. It is also likely to provide superior performance for flows involving rotation, boundary layers under strong adverse pressure gradients, separation and recirculation.

Both the realisable and RNG k-ε models have shown substantial improvements over the standard k-ε model where the flow features include strong streamline curvature, vortices and rotation. Since the model is still relatively new, it is not clear in exactly which instances the realisable k-ε model consistently outperforms the RNG model. However, initial studies have shown that the realisable model provides the best performance of all the k-ε model versions for several validations of separated flows and flows with complex secondary flow features.

The near-wall modelling significantly affects the reliability of numerical solutions, since the walls are the main source of vorticity and turbulence. The solution variables have large gradients at the near-wall region, and the momentum and other scalar transports occur most vigorously at this point. Accurate representation of the flow in the near-wall region determines successful predictions of wall-bounded turbulent flows.

6.2.3.2 NEAR-WALL TREATMENT FOR k-ε MODELS

The near-wall treatments available in FLUENT allows for modification to the k-ε model that takes into account viscous effects and the no-slip condition (law-of-the-wall). There are two approaches to modelling the near-wall region. In one approach, the viscosity-affected inner region (viscous sublayer and buffer layer) is not resolved. Semi-empirical wall functions are used instead to bridge the viscosity-affected region between the wall and the fully turbulent

region. Wall functions (split into standard wall functions, and non-equilibrium wall functions) must be used together with taking into account the need to modify the turbulence models to account for the presence of the wall. In another approach, the turbulence models are modified to enable the viscosity-affected region to be resolved with a mesh all the way to the wall, including the viscous sublayer. These approaches are illustrated in Figure 6-1.

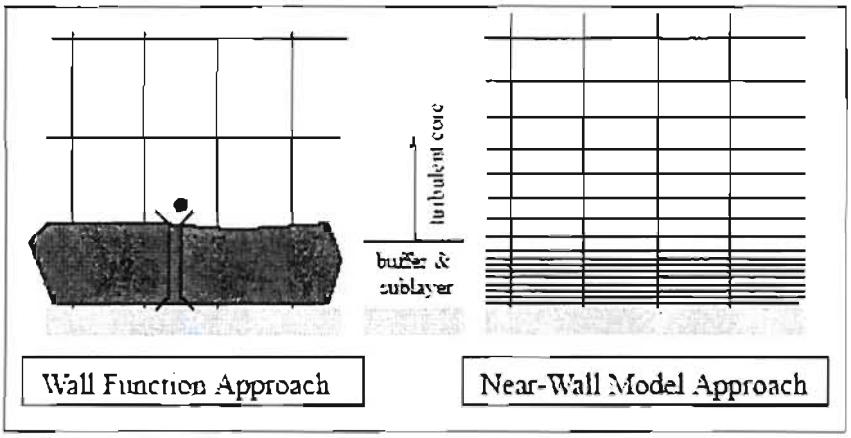

Figure 6-1: Near-wall treatments available (reproduced from FLUENT user manual)

In most high Reynolds-number flows, the wall function approach saves a considerable amount on computational resources because the viscosity-affected near-wall region in which the solution variables change most rapidly does not need to be resolved. The wall function approach is widely used as it is economical and robust within reasonable accuracy. It is a practical option for the near-wall treatments for industrial flow simulations. The wall function approach has proved to be inadequate in situations with a low Reynolds number. Such situations require near-wall models that are valid in the viscosity-affected region and thus possible to integrate all the way to the wall.

Another approach to this problem involves the use of enhanced wall treatment. This is a near-wall modelling method that combines a two-layer model with enhanced wall functions, but does require for the near-wall mesh to be sufficiently fine everywhere. This imposes a large amount of computational time, and FLUENT accommodates the option of combining the two-layer model with enhanced functions. This allows for significant improvements in computing times, without considerably decreasing the accuracy of the results.

6.2.3.3 k-ω TURBULENCE MODELS

There are two k-ω models available in FLUENT, namely the standard k-ω model and the SST (Shear Stress Transport) k-ω models. Both models have similar forms, with transport equations k and ω. The standard k-ω model is based on the model by Wilcox (1998), which incorporates modifications for low Reynolds-number effects, compressibility and shear flow spreading. The Wilcox model predicts free shear flow spreading rates that are in close agreement with measurements for far wakes, mixing layers, and plane, round and radial jets. This makes the model applicable to wall-bounded flows and free shear flows.

In addition to the standard k-ω model, FLUENT also provides a variation in the SST k-ω model, with the definition of the turbulent viscosity modified to account for the transport of the principal turbulent shear stress. The SST k-ω model was developed by Menter (1994) to effectively blend the reliable and accurate formulation of the k-ω model in the near-wall region with the freestream independence of the k-ε model in the far field. This is achieved by converting the k-ε model into a k-ω formulation.

The standard k-ω model and the transformed k-ε model are both multiplied by a blending function and both models are added together. The blending function ensures that the model equations behave appropriately in both the near-wall and far-field zones. Together with a few other minor refinements, these features make the SST k-ω model more accurate and reliable than the standard k-ω model for a wider class of flows involving adverse pressure gradient flows, airfoils and transonic shock waves.

The models described in this chapter were all used for the modelling of the system, as they all were suitable for the purpose of transonic flow across the SMR-95 turbine blade. Ranging from the almost rudimentary one-equation models to the more accurate two-equation variations, one could ascertain the accuracy of all the models compared to the experimental data and judge the feasibility of those models with regard to computing power and time.

6.3 MODELLING AND RESULTS

6.3.1 MODEL SETUP

6.3.1.1 INTRODUCTION

The modelling of the flow conditions inside the cascade and plenum of the experimental supersonic cascade facility requires certain specifications and conditions to be correct and relevant to the actual system. Before applying these conditions, the actual system geometry had to be modelled in the pre-processor of GAMBIT.

The blade coordinates and cascade geometries were already created by De Villiers (2002). This was used for the numerical validation, as the actual cascade and blade geometries in the facility were unchanged. The model was drawn up as 2-D geometry, and both the cascade box and entire plenum were modelled in separate files to compare the accuracy of the results. Since the experimental data was acquired from the mid-span of the test blade, and it was known that there were no significant secondary flow effects, the 2-D model seemed sufficient for the scope of validation as opposed to a 3-D model of the system.

The mesh that was created by De Villiers (2002) was looked at for any possible improvements, and was reconstructed using the boundary layer mesh. Certain other meshing techniques were looked at for better accuracy, including a decomposed grid to minimise the size of the cells used. The accuracy of these results compared to the boundary layer mesh would be judged as a feasibility of the extra computational time required.

6.3.1.2 OPERATING CONDITIONS

The "material" setup in FLUENT is for the program to model the correct fluid used in the system. The standard conditions for air were used, and the default settings for specific heat, viscosity and thermal conductivity were given by the program. The density of the operating fluid was set to "ideal-gas", most importantly, as FLUENT would then recognise the flow as compressible. This automatically enables the energy equations within the program, which are solved simultaneously with the transport equations when using the coupled solver.

The operating pressure is directly linked to the choice of using the fluid as an "ideal-gas", as this law incorporates the equation:

$$\rho = \frac{p_{op} + p}{RT} \qquad (6.3.1.2.1)$$

where p_{op} is the operating pressure, p is the local relative (gauge) pressure, R is the universal gas constant of 287 Pa.m^3/kg.K, and T is the temperature. The operating pressure must be set as defined by the Mach number observed in the system. The FLUENT user manual suggests the use of the operating pressure set to 0 Pa when M > 0.1. This is suited to the operating conditions inside the plenum, and thus the operating pressure was set to 0 Pa. Thus it must be noted that all pressure values entered into and displayed by the program are relative to this operating pressure.

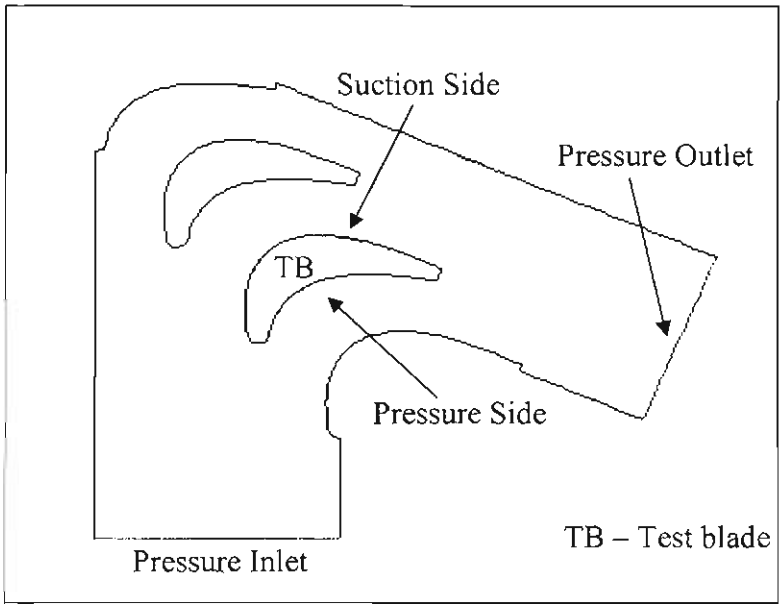

Figure 6-2: GAMBIT cascade geometry

The pressure inlet and outlet settings in the program were set using the values attained in the static pressure testing, described in Section 5.2 of Chapter 5. The inlet conditions were obtained from the pressure and temperature probes, and the settings entered into FLUENT are shown in Table 6-1, and applied to the inlet section as shown in Figure 6-2.

The total gauge pressure was set at 40 kPa. The "Supersonic/Initial Gauge Pressure" was set at 35 kPa, corresponding to the static pressure at the inlet of the cascade box, which was measured experimentally. The total stagnation temperature was also measured experimentally by the Kiel probe at the inlet of the cascade. The practical method of specifying turbulence was by using the

"Intensity and Hydraulic Diameter", where the turbulence intensity was measured to be 3% for a free inlet by Snedden (1995) and the hydraulic diameter being the characteristic width of the inlet.

Table 6-1: Inlet Conditions

SETTING	VALUE
Total Gauge Pressure	40 000 Pa
Supersonic/Initial Gauge Pressure	35 000 Pa
Total Temperature	373 K
Direction Specification Method	Normal to Boundary
Turbulence Specification Method	Intensity and Hydraulic Diameter
Turbulence Intensity	3%
Hydraulic Diameter	118.72 mm

Similarly, the outlet conditions were set by using experimental data and entering the values into the program, applied to the outlet section as seen in Figure 6-2. These settings are shown in Table 6-2.

Table 6-2: Outlet Conditions

SETTING	VALUE
Total Gauge Pressure	27 000 Pa
Backflow Total Temperature	350 K
Direction Specification Method	Normal to Boundary
Turbulence Specification Method	Intensity and Hydraulic Diameter
Turbulence Intensity	3%
Hydraulic Diameter	92 mm

The gauge pressure was measured experimentally, and entered relative to the operating pressure. The turbulent intensity was kept constant, and the hydraulic diameter was the characteristic width at the outlet of the cascade.

6.3.2 CONVERGENCE CONSIDERATIONS

To start the iteration process, all zones in the model were initialised to give the program a starting point with initial conditions that allow for the final solution to be attained after iteration. FLUENT calculated average values for velocities, gauge pressure, turbulent kinetic energy and turbulence dissipation rates. The velocities were set manually to zero (in both the x- and y-directions) as it was found that this yielded faster convergence times in the simulations.

For the program to iterate successfully and achieve convergence, there must be some considerations which need to be taken into account. Once the initial guess is made, and an approximate solution is attained, this leads to a small imbalance in the conservation equation. This imbalance in each cell in the model is referred to as the residual. When iterating, this value decays and begins to "level off" at a certain value. Judging convergence is usually done by monitoring the residuals, of which the values tend to drop in the order of 10^{-3}. This is the default value set by FLUENT and was used in all the simulations. The program checks certain criteria with residual monitors and stops the simulation automatically once these criteria are met.

Together with these criteria, the drag coefficient and the mass flow balance at the inlet and outlet were monitored as well.

Another factor that affected the convergence of the simulation was the Courant number (CFL), which is the main control over the time-stepping scheme. The FLUENT user manual suggests a default CFL value of 5 for the coupled implicit solver, and possibly increasing it to 10, 20, 100, or even higher. Lower CFLs are suggested at the start of the simulation, when changes in the solution are highly non-linear, and can be increased as the solution progresses as larger values lead to faster convergence. Different values for the CFL were found to be suitable for the different turbulence models, and are shown in Table 6-3.

Table 6-3: Suitable CFL Numbers for Different Turbulence Models

TURBULENCE MODEL	CFL
Spalart-Allmaras	20
Realisable k-ε	10
RNG k-ε	10
Standard k-ω	10
SST k-ω	15

6.3.3 MODELS AND MESHING

There were two geometric models used by De Villiers (2002). One included just the cascade box and blade geometries, while the other model incorporated the entire plenum space from the annular radiator and the cascade. The meshes used by De Villiers (2002) were refined such that the accuracy of results was increased and the convergence times improved. By observing the "equiangle skewness" in GAMBIT, one could judge the improvement of the mesh by finding the cell with the worst skewness.

The first model that was adjusted was the grid involving only a 2-D model of the cascade box and SMR-95 blades, as shown in Figure 6-3. There are a number of meshing schemes that can be used, with several shapes of cells. The choice of scheme would depend on the complexity of the geometry, setup time and computational expense of the final grid.

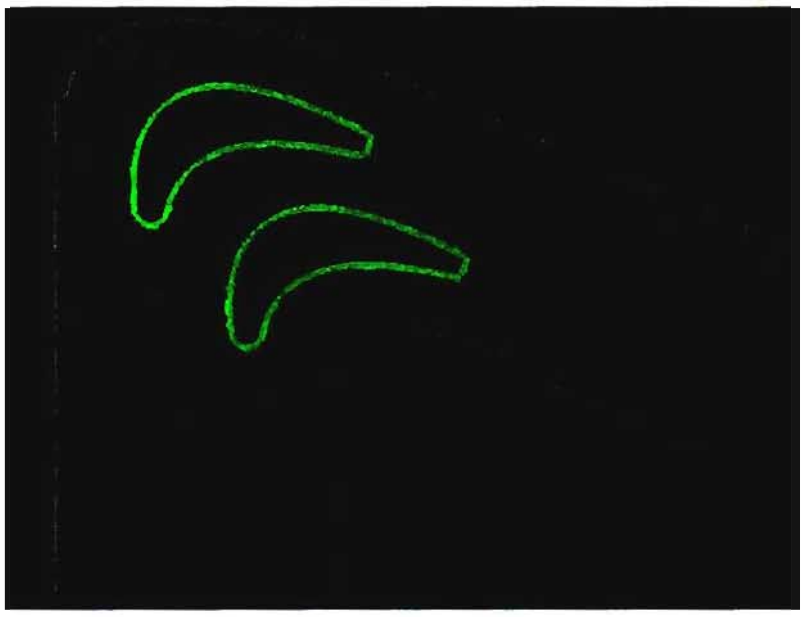

Figure 6-3: Refined mesh using boundary layers

Instead of using a fully unstructured grid, a boundary layer mesh was applied to both the test blade and the neighbouring dummy blade. The resulting cell sizes on the walls of the suction and pressure sides of the test blade would result in more accurate predictions, and a better resolution. A boundary layer mesh was applied to the dummy blade as well, since the flow at the trailing edge affected the flow on the pressure side of the test blade. The previous grid of De Villiers (2002) had a first cell height of 0.01 mm, growth rate of 1.35 and 16 rows, which yielded a boundary layer height of 3.45 mm, and $y^+ \approx 1$, which reduces stability problems in certain turbulence models. The worst cell skewness was 0.67.

The boundary layer applied to the new mesh had a first cell height of 0.001 mm, growth factor of 1.2, and a larger number of rows of 27 as the cell sizes were chosen to be smaller. The pave meshing scheme was used to fill the cascade space for the main flow using quad elements of interval size 1.5. This yielded a worst equiangle skewness of 0.52, which was favourable compared to the previous cell skewness of De Villiers (2002).

To improve the resolution of the cells in the mesh, and possibly improve the accuracy of the results, a decomposed mesh was constructed. This involved splitting the domain into several sections such that the skewness would be minimal when using only quad cells. This mesh is shown in Figure 6-4.

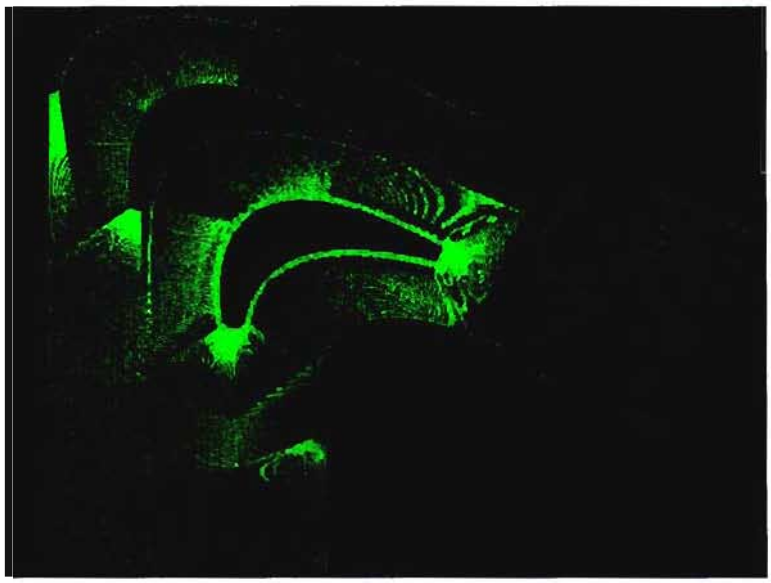

Figure 6-4: Decomposed mesh

This mesh was achieved by using the same boundary layer mesh on the blades as used in the previous grid, and meshing the incomplete regions with quad cells using an interval size of 1. This resulted in a total number of elements of close to 400 000, as compared to the total number of cells of around 18 500 for the previous grid. Cassie (2006) investigated the results of the simulations using this grid, and proved that the change in results was insignificant as compared to the original grid. The computational time was almost tripled, and thus the model was discarded, proving that the initial boundary layer mesh was sufficient for relatively accurate results.

The geometry used by De Villiers (2002), which incorporated the entire plenum was investigated and the mesh improved. This model is shown in Figure 6-5. A transition in the resolution of the mesh size was achieved from the cascade to the plenum. The walls of the bell-mouth inlet were meshed using the boundary layer option, and a larger interval size was used

for a smooth transition and minimal skew cells at the inlet of the cascade. The plenum was meshed using a very coarse mesh, as the flow in this area was not of close concern. The inlet conditions for this model would need to be known at the annular radiator, making this method unfavourable. It was shown by De Villiers (2002) that the difference in results of this plenum model proved to be insignificant compared to the original grid of the cascade box. Together with this knowledge and the fact that the inlet conditions were not accurately known, this model was discarded and the cascade box with definite inlet and outlet conditions was used.

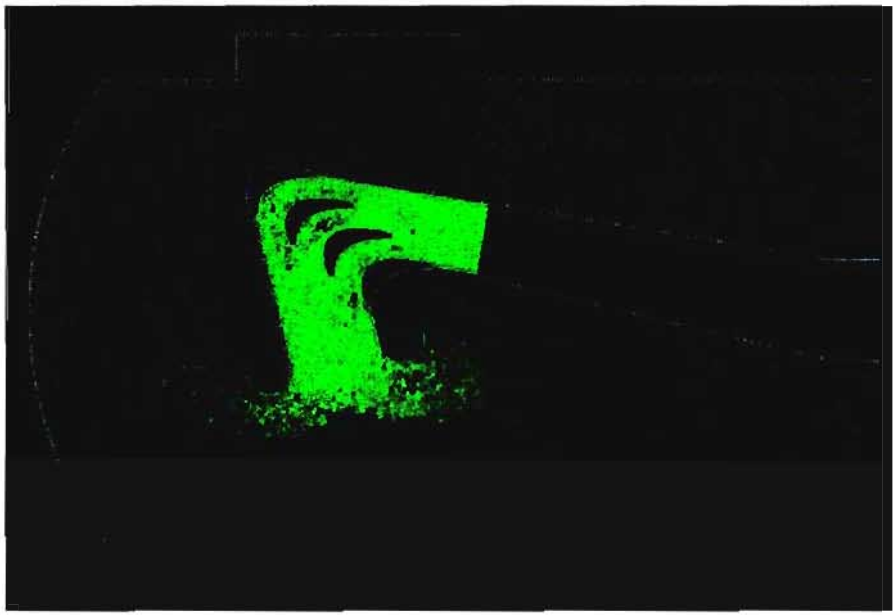

Figure 6-5: Grid incorporating entire plenum

6.3.4 RESULTS

The conditions and parameters were set in FLUENT and simulations were run for the free inlet condition using the different turbulence models. The initial blade wall temperatures were set at 313 K, as measured experimentally. By using the various CFL values for different turbulence models (as described in Section 6.3.2), FLUENT performed the iterations to attain a final solution that would calculate the heat flux into the blade along the pressure and suction surfaces, based on the flow conditions and the temperatures that would be calculated.

The conversion from the heat flux to a heat transfer coefficient was of the same method of the experimental calculation. This would involve dividing the wall heat flux by the difference between the total and wall temperatures at the point that would be calculated. The wall flux values were exported from FLUENT by coordinates, and using the x-axis for "curve length" and the y-axis for "wall fluxes".

The solutions for the various turbulence models all seemed to converge after around 2 000 iterations after using their specific CFL values. The Spalart-Allmaras model initially was not converging, and this non-convergence result was reported by De Villiers (2002). However, after lowering the CFL to around 5 in the initial stages of the simulation and gradually increasing this value back to 20 during the course of the iteration process, the solution converged. This method of maintaining a stable solution has been discussed previously in Section 6.3.2.

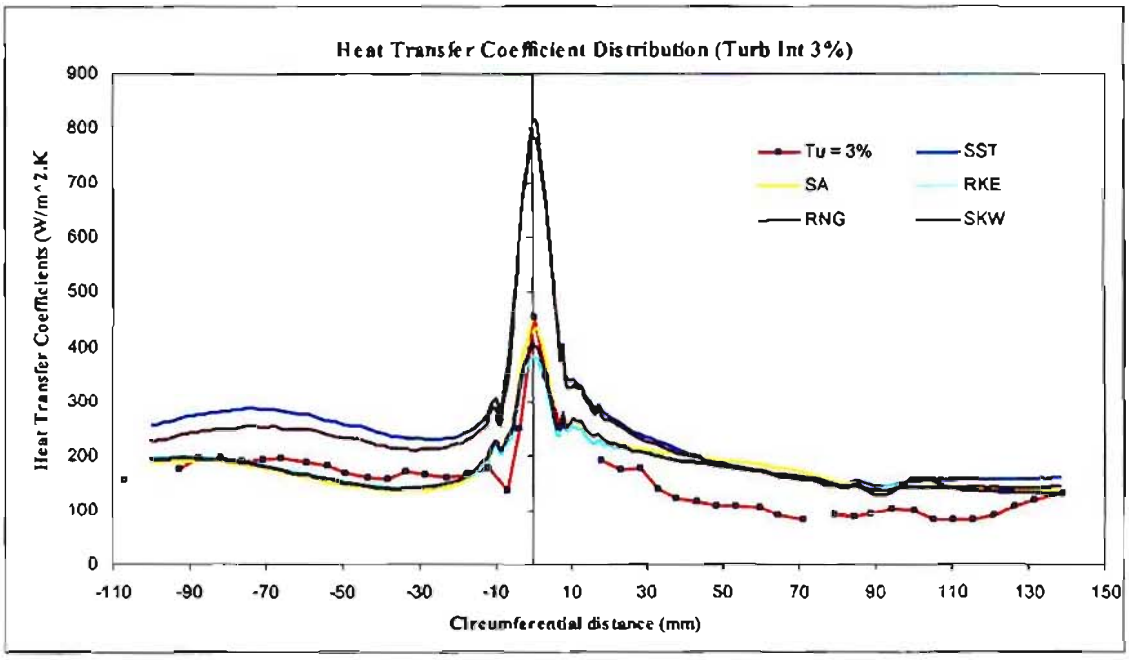

Figure 6-6: Heat transfer coefficient prediction for Tu = 3%

The heat transfer coefficient distribution along the SMR-95 blade that was predicted by each turbulence model is shown in Figure 6-6, together with the distribution that was calculated from experimental testing.

One can see that the general trend from the k-ε models followed the experimental distribution with regard to the magnitude of the heat transfer coefficient on the pressure side. Although there is a slight under-prediction between 70 mm and 20 mm circumferential distance on the pressure side (and consequently a different curve), the heat transfer coefficient at the leading edge was accurately predicted. The Spalart-Allmaras model was the most accurate in predicting the leading edge heat transfer coefficient.

The separation bubble that forms at around the 10 mm circumferential distance on the pressure side (as evident by the drop in heat transfer in the experimental distribution) is shown to be predicted by the k-ε models by looking at the discontinuity of the curve at this point. This is also evident on the suction side of the curve, where the discontinuity in the curve occurs at the

speculated point of another separation bubble. This phenomenon was unclear in the experimental heat transfer coefficient distribution due to reasons described in Section 5.3.5.4. Further examination of the velocity vector plot at this point revealed a reversal in flow, as shown in Figure 6-7 and reported by De Villiers (2002) and Cassie (2006). Further turbulent regions and flow reversal were also noted from the vector plot at the trailing edge of the blade.

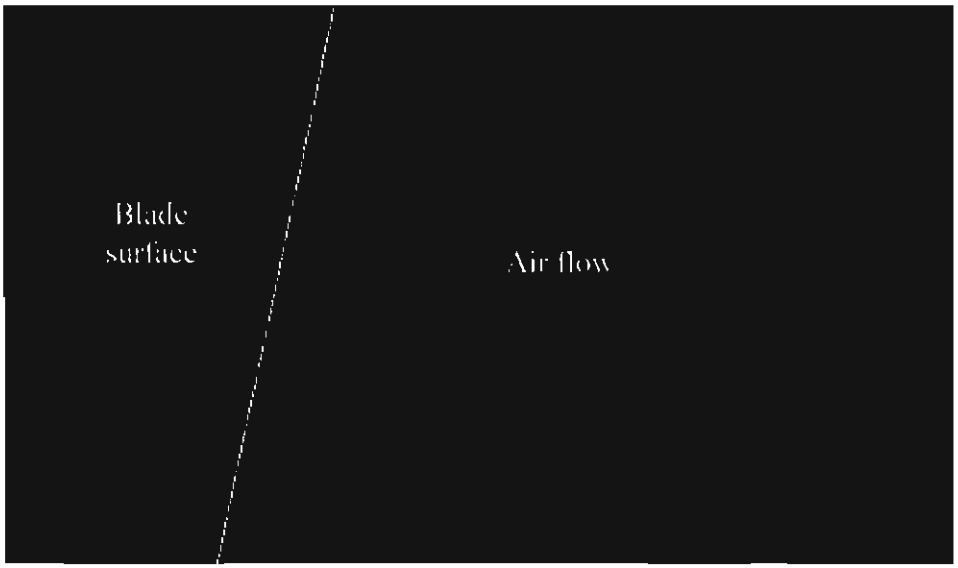

Figure 6-7: Flow reversal in the velocity vector plot indicating a separation bubble

The distribution on the suction side seemed to follow a similar trend compared to the experimental curve, however, there was a large over-prediction in the magnitude of the heat transfer coefficients for both the k-ε models and k-ω turbulence models. The slight disturbance in the curves of all the turbulence models at around 95 mm circumferential distance on the suction side was expected, as the experimental plot showed evidence of a smaller separation bubble at this point.

The SST k-ω model seemed to follow the experimental distribution the most accurately on both the suction and pressure surfaces, as well as predicting the separation bubbles that occurred at various points along the SMR-95 surface. There was a large over-prediction in the magnitude of the heat transfer coefficient when compared to the experimental curve, and this proved to be somewhat constant throughout the distribution.

The standard k-ω model predicted a distribution similar to that of the SST k-ω turbulence model, with a few discrepancies when closely compared to the experimental distribution. The leading edge heat transfer coefficient was largely over-predicted as well, and proved to do so even further in the cases for Tu = 15% and Tu = 25.5%. Hence the model results for the standard k-ω turbulence model will be omitted from those particular comparisons following.

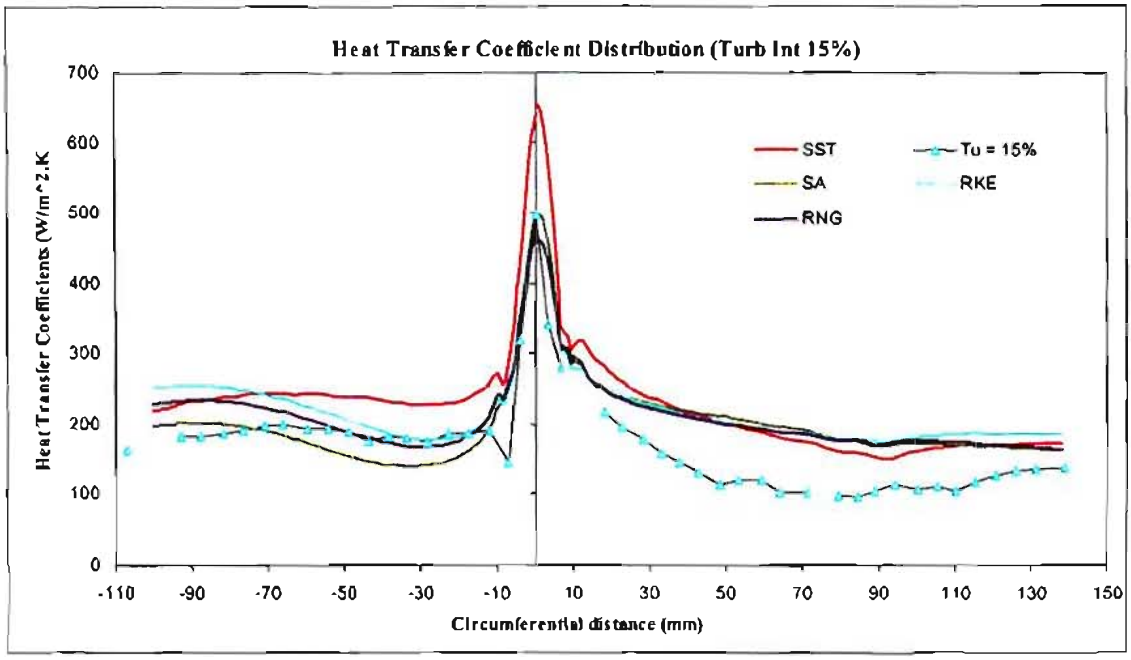

Figure 6-8: Heat transfer coefficient prediction for Tu = 15%

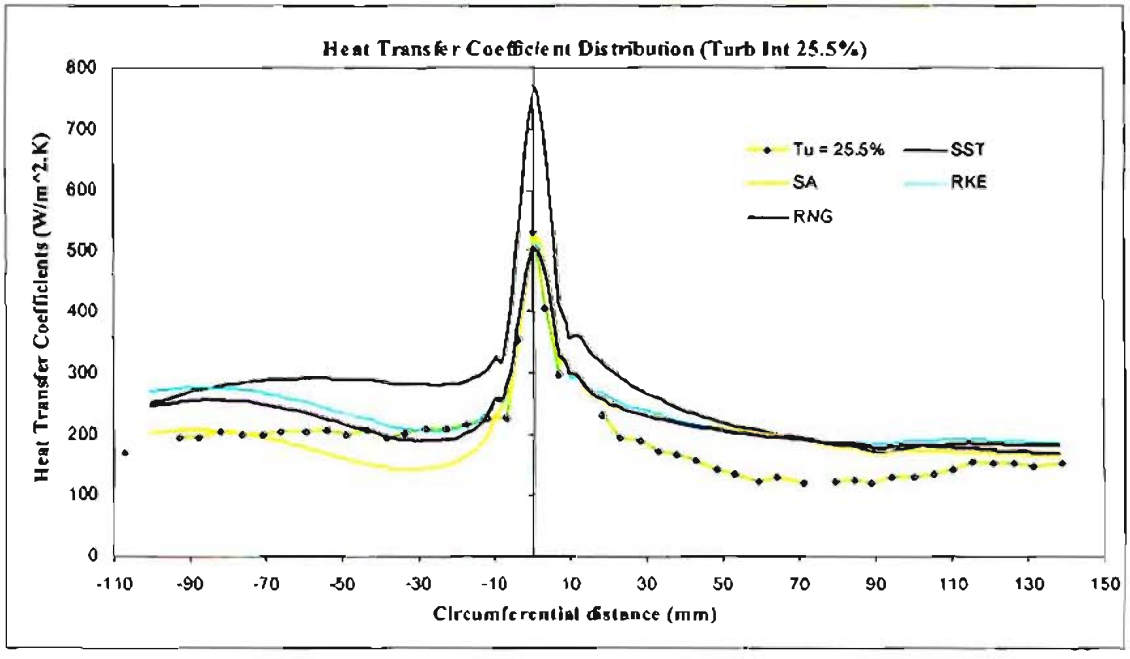

Figure 6-9: Heat transfer coefficient prediction for Tu = 25.5%

The heat transfer coefficient distributions shown in Figure 6-8 and Figure 6-9 depict the predictions of the turbulence models together with the experimental distribution curve for both Tu = 15% and Tu = 25.5% respectively. One can see the steady increase of the overall heat transfer from the free inlet condition for all turbulence models.

The k-ε models still represent a closer prediction to the experimental curve with regard to the magnitude of heat transfer. The actual curves do not match the experimental distributions for both the Tu = 15% and Tu = 25.5% cases, and again there is a large over-prediction on the suction side of the blade. The Spalart-Allmaras model again accurately predicted the heat transfer coefficient at the leading edge of the blade for both turbulence conditions when compared to the free inlet condition. One can see in the results for Tu = 15% that the disturbances (occurring at the discussed points where separation bubbles occur) have diminished slightly. This prediction is representative of the actual occurrence in the experimental plot as discussed in Section 5.3.5.5. The SST k-ω turbulence model again predicts a more accurate distribution, but the magnitude of heat transfer is shown to be largely over-predicted, especially at the leading edge of the blade.

The discontinuity of the distribution curve on the suction side of the SST k-ω model at approximately 90 mm circumferential distance gives a good indication of the diminishing phenomenon of the drop in heat transfer at this point. The lack of continuity of the experimental distribution along this range gives an indication of the almost crude nature of the data acquisition system, and the various experimental errors that could have affected the results.

By comparing this directly with the case for Tu = 25.5%, one can see the lack of drop in heat transfer at the points near the leading edge where the separation bubbles occur for lower turbulence intensities. The indication of a small bubble near the trailing edge of the blade is now almost completely absent when looking at the SST k-ω turbulence model.

6.3.5 CONCLUSIONS

From the different geometries of incorporating the entire plenum and decomposing the mesh for the cascade geometry, only one model was deemed accurate and reliable enough to attain heat transfer coefficient distribution predictions along the SMR-95 turbine blade to compare to the experimental data set.

The cascade model was used and the boundary layer mesh was improved together with the pave meshing scheme. With the inlet and outlet conditions accurately known, these were applied to the model with the relevant CFL values that seemed to optimise each turbulence model. The resulting solutions from FLUENT provided insight into the different predictions of the various turbulence models.

The trend seemed consistent for all the turbulence intensity cases, with the k-ε turbulence models proving to be the most accurate in predicting the heat transfer close to the leading edge of the blade. The Spalart-Allmaras model seemed to accurately predict the heat transfer coefficient at the leading edge. Both the Realisable k-ε model and the RNG k-ε model lacked the ability to closely predict the distribution curve on both the pressure and suction sides of the blade, when compared to the experimental distribution. There was a large over-prediction of the magnitude of heat transfer on the suction side for all turbulence models.

The SST k-ω turbulence model proved to be the most accurate in predicting the actual curve compared to the experimental distribution, however, it over-predicted the magnitude of heat transfer along the entire surface of the blade and even more at the leading edge of the blade. This shows the model's strength in predicting flows in transonic conditions, but did not perform due to the conditions of large flow separation. This is a commonly-known disadvantage of this turbulence model, as it uses the Boussinesq approximation which results in an inability to predict anisotropy (Pattijn *et al.* (1999)).

The discrepancies in the CFD results are believed to be the result of using a 2-D model where the secondary flow effects are not taken into account, and of course the various experimental errors that could have contributed to the inaccuracies of the experimental heat transfer distribution. Cassie (2006) used a 3-D geometry to ascertain whether there would be a difference in the prediction of heat transfer for the turbulence models. He showed that there was no significant difference on the pressure surface of the blade. The presence of horseshoe vortices, which was also reported by Graziani *et al.* (1980), was shown to increase the heat transfer slightly on the suction side. Since the experimental data is taken at the midspan of the blade, there is not enough of a significant difference in the heat transfer prediction between the 2-D and 3-D models to validate the extremely large computational times needed for the 3-D simulations.

The static pressure contour plots for all the turbulence models are given in Appendix B, showing the visual differences in the predictions for the models with the various turbulence intensities.

CHAPTER 7

CONCLUSIONS

7.1 SUMMARY

This project served as a continuation of the ongoing study of aerodynamic flow and heat transfer effects at UKZN, with the goal being to ascertain the functionality of the supersonic cascade experimental rig, its reliability, continuity and its consistency of the results generated over the number of years of operation. This included a review of the current equipment, and researching suitable modern replacements of the ageing hardware. The heat transfer effects on the SMR-95 turbine blade were investigated for varying levels of turbulence intensity (namely the free inlet condition of Tu = 3%, as well as Tu = 15% and Tu = 25.5%). These were compared to previous results which were attained by MSc students who had worked on the experimental rig. The computational results of the CFD package of FLUENT were also investigated. These numerical predictions were compared to the existing experimental data for the varying levels of turbulence.

7.2 CONCLUSIONS

The current data acquisition system that was implemented by Snedden (1995) by using heat transfer analogue circuit boards proved to be rudimentary and generated an unsatisfactory amount of electrical noise, which seemed to affect the post-processing measurement of the results. Various numerical techniques were looked at and it was shown that the Crank-Nicholson scheme proved to be the most suitable technique to be used with the conditions prescribed and defined by the experimental facility. This technique was shown to be favourable when compared to the Cook-Felderman and Fourier Transform techniques by Dénos (1996), as well as the Walker inverse approach, which was shown to be impractical for the UKZN facility.

This implementation of a numerical data acquisition method would require a stable and reliable facility. The experimental rig at UKZN underwent refurbishments by the researchers who worked on the project, as the equipment that was used had always tended to be faulty, and certain components broke down or failed, and needed repair or replacement. This was thought to have a long-term effect on the results that the rig would generate, and static pressure tests were initially run to ascertain the conditions of the rig. The most recent refurbishments (with the aid

of Cassie (2006)) were the replacement of the leaking annular radiator, repair of the data acquisition boards and the re-instrumentation of the thin-film gauges for heat transfer analysis.

The results of the static pressure distribution along the blade compared very well to previous results attained, proving the consistency and reliability of the rig despite the numerous and lengthy downtimes that it had experienced over the years. The results were most comparable to that of Cassie (2006), mostly for the reason that he was the most recent of researchers that worked on the experimental facility.

The re-instrumentation of thin-film gauges on the SMR-95 Macor test blade was performed such that the blade would be set up with more sensitive gauges, and provide more accurate results if the electrical noise was reduced in relative comparison to what would be higher amplitude voltage changes. The actual gauges were painted onto the blade with platinum, with the connections to the leads being painted in gold. The properties and method of baking both sets of paint were basically the same, which aided in the ease of the process. After several layers of platinum and adjusting to the required resistances, the calibration of the gauges proved that the overall increase of sensitivity was minimal. Every gauge was functional, however, and this full resolution would aid in a full understanding of the results generated.

The heat transfer results for the free inlet condition compared well to that of Stieger (1998) and Cassie (2006). It was found that experimental errors occur for every reading of the sensors with the fluctuating compressor speed and varying temperatures and pressures. These conditions were monitored closely and the constant inputs into the post-processing program were as accurate as possible to try minimise any errors. The results of the heat transfer distribution with higher levels of turbulence intensity compared well again to those of Stieger (1998). The increase in heat transfer that was observed was of similar magnitude in previous results, as well as the diminishing effects of the separation bubbles which occurred around the leading edge of the blade in the free inlet condition.

The experimental data attained from the facility for the various turbulence levels were compared to numerical solutions attained from FLUENT. The existing geometrical model was used, created by De Villiers (2002), with the mesh reconstructed and refined. Other meshing strategies and models investigated and used by De Villiers (2002) and Cassie (2006) were not used after it had been reported that there were insignificant changes in results with higher resolution meshes. The pave meshing scheme with boundary layers on the blade proved to be sufficient with a 2-D model of the cascade box, where the inlet and outlet conditions were known from experimental probes and gauges during testing. Several turbulence models were

used to simulate the flow, and the results proved consistent for all turbulence levels. The k-ε turbulence models of the Realisable k-ε and RNG k-ε models (including the Spalart-Allmaras model) proved to be accurate in predicting the heat transfer around the leading edge of the blade when compared to the experimental data. Although the trend of the curve of distribution did not match well, the magnitude of heat transfer was favourable, with the Spalart-Allmaras model closely predicting the heat transfer coefficient at the leading edge. The SST k-ω turbulence model was shown to accurately predict the trend of the heat transfer coefficient distribution when compared directly to the experimental set, however, the model over-predicted the magnitude of heat transfer greatly along the entire surface of the blade. This unfortunate condition is a result of the model's inability to accurately predict flow conditions where there is large flow separation. The discrepancies seen in both the k-ε and k-ω models could also be due to the lack of consideration of secondary flow effects with the 2-D model and the unpredictability of turbulence, and of course the fact that the entire plenum cannot be successfully modelled and implemented without accurate inlet and outlet conditions. However, the phenomenon observed in the experimental data was shown to have been predicted by the numerical models, particularly the SST k-ω model, with regard to the effects and formation of separation bubbles at the different turbulence intensities.

This numerical model validation was successful when compared to the experimental heat transfer distribution that was attained from the experimental facility.

7.3 Recommendations for Future Work

The condition of the experimental facility slowly deteriorated over the period of testing, with the most concerning problem being the oil leak in the hydraulic motor. The funding for any repair or replacement would exceed that given for the project. This problem, along with various other minor issues, proved that the facility needs a major reconstruction and the equipment to be modernised before any implementation of different methods and techniques to acquire heat transfer data. Ideally an allowance for all the sensors to be sampled at the same time would be needed, which is not possible with the current system. This system needs many hours for all the sensors to be finally sampled, and the base test conditions and temperatures fluctuate with the inconsistent compressor blade speeds. This would lead to unfavourable experimental errors.

This facility would need a major overhaul if research is to successfully continue. The deteriorating conditions of the rig would only lead to inaccuracies of results and the eventual

breakdown of key components that would allow continuous safe running and generation of results. The damaged sensors and lack of resolution in these areas would mean that another re-instrumentation of the blade would be necessary, including investigating a safer method of the plunging mechanism such that there would be no reoccurrence of this problem.

The problematic hydraulic drive could be replaced altogether, with a DC drive motor, for example, to run the centrifugal compressor. This would also allow the user to remain in the plenum room and adjust the compressor blade speed, whereas currently the user has to leave the room to attend to the hydraulic drive and manually adjust the angle of the swash-plate from there.

When the facility is running in a condition where there would be more research than repair, the implementation of the numerical heat transfer data acquisition system would be recommended, together with automated control of certain components of the facility (and the upgrade and replacement of the ageing equipment) that would allow for constant operating conditions and minimal experimental error.

REFERENCES

Bellows, W.J. and Mayle, R.E. 1986. Heat transfer downstream of a leading edge bubble. *ASME Journal*, 86-GT-59.

Bezuidenhout, J.J. 2000. *Convective heat flux determination using surface temperature history measurements and an inverse calculation method.* MSc dissertation. Virginia: Virginia Polytechnic Institute and State University.

Boyle, R.J., Lucci, B.L., Verhoff, V.G., Camperchioli, W.P. and La, H. 1998. Aerodynamics of a Transitioning Turbine Stator over a Range of Reynolds Numbers. *ASME Paper* 98-GT-295 (NASA/TM-1998-208408).

Buttsworth, D.R. 1997. *A finite difference routine for the solution of transient one dimensional heat conduction problems with curvature and thermal-dependent thermal properties.* University of Oxford, OUEL Report number 2130/97.

Cassie, K.B. 2006. *An experimental and numerical convective heat transfer analysis over a transonic gas turbine rotor blade.* MSc dissertation. University of KwaZulu-Natal.

Cengel, Y.A. and Boles, M.A. 2001. *Thermodynamics: An Engineering Approach.* 4th Edition. New York: McGraw-Hill.

Consigny, H. and Richards, B.E. 1982. Short Duration Measurements of Heat Transfer Rate to a Gas Turbine Blade. *ASME Journal of Engineering for Power*, 104 (3), 542-551.

Cook, W.J. and Felderman, E.J. 1966. Reduction of Data from Thin-Film Heat-Transfer Gauges: A Concise Numerical Technique. *AIAA Journal*, 4 (3), 561-562.

Cook, W.J. 1970. Determination of Heat-Transfer Rates from Transient Surface Temperature Measurements. *AIAA Journal*, 8 (7), 1366-1368.

De Villiers, J.E. 2002. *Experimental and numerical validation of the flow and heat transfer on a transonic turbine blade.* MSc dissertation. School of Mechanical Engineering, University of Natal.

Dénos, R. 1996. *Aero-thermal investigation of the unsteady flow field in the rotor of a transonic turbine*. PhD thesis. University of Poitiers, Poitiers.

Diller, T.E. and Kidd, C.T. 1997. *Evaluation of Numerical Methods for Determining Heat Flux with a Null Point Calorimeter*. Proceedings of the 42nd International Instrumentation Symposium, ISA, Research Triangle Park, NC, pp. 251-262.

Diller, T.E. 1993. Advances in heat flux measurements. Academic Press Inc, ISBN 0-12-020023-6, *Advances in heat transfer*, 23, 279-368.

Doorly, D.J. and Oldfield, M.L.G. 1985. Simulation of the Effects of Shock Waves Passing on a Turbine Rotor Blade. *ASME Journal of Engineering for Gas Turbines and Power*, 107, 998-1006.

Doorly, J.E. and Oldfield, M.L.G. 1986. New heat transfer gages for use on multilayered substrates. *Journal of Turbomachinery*, 108, 153-160.

Doorly, J.E. and Oldfield, M.L.G. 1987. The Theory of Advanced Multi-Layer Thin Film Heat Transfer Gauges. *Journal of Heat Mass Transfer*, 30 (6), 1159-1168.

Doorly, J.E. 1988. Procedures for determining surface heat flux using thin film gages on a coated metal model in a transient test facility. *Journal of Turbomachinery*, 110, 242-250.

Dunn, M.G. 2001. Convective heat transfer and aerodynamics in axial flow turbines. *ASME TURBO EXPO*, 2001-GT-0506.

Dunn, M.G. 1984. Turbine Heat Flux Measurements: Influence of Slot Injection on Vane Trailing Edge Heat Transfer and Influence of Rotor on Vane Heat Transfer. *ASME Paper* 84-GT-175.

Dunn, M.G., Martin, H.L. and Stanek, M.J. 1986. Heat Flux and Pressure Measurements and Comparison with Prediction for a Low Aspect Ratio Turbine Stage. *ASME Journal of Turbomachinery*, 108, 108-115.

Eagle Technology. 1990. *User manual for PC30 PGL and PC30 PGH*, 2nd Edition. Cape Town: Eagle.

Feist, J.P., Heyes, A.L. and Seefelt, S. 2003. Thermographic phosphor thermometry for film cooling studies in gas turbine combustors. Proceedings of the Institution of Mechanical Engineers, Part A: *Journal of Power and Energy*, 217 (2), 193-200.

Fluent Inc. 2006. Fluent Inc. Product Documentation.
root:\Fluent.inc\documentaion\Fluent.inc\manuals\index.html

Frati, G. and Dénos, R. 2002. One-dimensional unsteady modeling of the flow-field in a short duration facility. *ASME/IGTI, GT-2002-30456.*

Goldstein, R.J. and Cho, H.H. 1995. A review of mass transfer measurements using naphthalene sublimation. *Experimental Thermal and Fluid Science*, 10 (4), 416-434.

Goldstein, R.J. and Spores, R.A. 1988. Turbulent Transport on the Endwall in the Region between Adjacent Turbine Blades. *ASME Journal of Heat Transfer*, 110, 862-869.

Goldstein, R.J. and Yoshida, T. 1982. The influence of a laminar boundary layer and laminar injection on film cooling performance. *Journal of Heat Transfer*, 104, 355-362.

Gratton, A.R. 2004. *Measurements and Predictions of Heat Transfer for a First Vane Design.* MSc dissertation. Virginia Polytechnic Institute and State University, Virginia.

Graziani, R.A., Blair, M.F., Taylor, J.R. and Mayle, R.E. 1980. An experimental study of endwall and airfoil surface heat transfer in a large scale turbine blade cascade. *Journal of Engineering and Power*, 102, 257-267.

Han, J., Dutta, S. and Ekkad, S. 2000. *Gas Turbine Heat Transfer and Cooling Technology.* New York: Taylor and Francis.

Hayashi, M., Aso, S. and Tan, A. 1989. Fluctuation of Heat Transfer in Shock Wave/Turbulent Boundary-Layer Interaction. *AIAA Journal*, 27 (4), 399-404.

Hinz, J. 1975. *Turbulence*, 2nd Edition. New York: McGraw-Hill.

Holden, M.S. 1972. Shock Wave-Turbulent Boundary Layer Interaction in Hypersonic Flow. *AIAA Paper*, 72-74.

Hong, K. and Song, T. 2007. Development of optical naphthalene sublimation method. *International Journal of Heat and Mass Transfer*, 50 (19-20), 3890-3898.

Incropera, F.P. and DeWitt, D.P. 1996. *Fundamentals of heat and mass transfer*. 4th Edition. Hoboken: John Wiley.

Jones, W.P. and Launder, B.E. 1973. The calculation of low-Reynolds-number phenomena with a two-equation model of turbulence. *International Journal of Heat and Mass Transfer*, 16, 1119-1130.

Kader, B. 1993. Temperature and Concentration Profiles in Fully Turbulent Boundary Layers. *International Journal of Heat and Mass Transfer*, 24 (9), 1541-1544.

Launder, B.E. and Spalding, D.B. 1972. *Lectures in Mathematical Models of Turbulence*. London: Academic Press.

Launder, B.E. and Spalding, D.B. 1974. The numerical computation of turbulent flows. *Computer Methods in Applied Mechanics and Engineering*, 3, 269-289.

Ligrani, P.M., Camci, C. and Grady, M.S. 1982. *Thin film heat transfer gage construction and measurement details*. Technical Memorandum 33, Von Karman Institute for Fluid Dynamics.

McDonald, G. 1994. *Measurement of tip clearance pressure distributions and heat transfer on a turbine blade at realistic blade velocities*. MSc dissertation. School of Mechanical Engineering, University of Natal.

Menter, F.R. 1994. Two-equation Eddy-Viscosity Turbulence Models for Engineering Applications. *AIAA Journal*, 32 (8), 1598-1605.

Nasir, H. 2004. *Turbine blade tip cooling and heat transfer*. PhD thesis. Louisiana State University and Agricultural and Mechanical College, Louisiana.

Nix, A.C. 2003. *Effects of High Intensity, Large-Scale Freestream Combustor Turbulence on Heat Transfer in Transonic Turbine Blades*. PhD thesis. Virginia Polytechnic Institute and State University, Virginia.

Noel, J.P., Hamm, H.E. and Sigler, P.B. 1993. The 2.2 A crystal structure of transducin-alpha complexed with GTP gamma S. *Nature*, 366 (6456), 654 -663.

Oldfield M.L.G., Burd, H.J. and Doe, N.G. 1982. *Design of wide-bandwidth analogue circuits for heat transfer instrumentation in transient tunnels.* Department of Engineering Science, University of Oxford.

Oldfield, M.L.G., Schultz, D.L. and Jones, T.V. 1978. On-line computer for transient turbine cascade instrumentation. *IEEE Transactions on Aerospace and Electronic Systems*, AES-14 (5), 738-749.

Pattijn, S., Steelant, J. and Dick, E. 1999. The potential of non-linear turbulence models – Importance of the basic two-equation model. *AIAA Fluid Dynamics Conference, 30th*, AIAA-1999-3778. Norfolk, VA.

Peabody, H.L. 1997. *Evaluation of a Heat Flux Microsensor in a Transonic Turbine Cascade.* MSc dissertation. Virginia Polytechnic Institute and State University, Virginia.

Polanka, M.D. 1999. *Detailed Film Cooling Effectiveness and Three Component Velocity Field Measurements on a First Stage Turbine Vane Subject to High Freestream Turbulence.* PhD thesis. University of Texas, Austin.

Radomsky, R.W. and Thole, K.A. 1998. Effects of High Freestream Turbulence Levels and Length Scales on Stator Vane Heat Transfer. *ASME 98-GT-236.*

Reiss, H., Bölcs, A., and Drost, U. 1998. *The Transient Liquid Crystal Technique Employed for Sub- and Transonic Heat Transfer and Film Cooling Measurements in a Linear Cascade.* XIV biennial Symposium on Measuring Techniques in Transonic and Supersonic Flow in Cascades and Turbomachinery, University of Limerick, Ireland.

Schultz, D.L. and Jones, T.V. 1973. Heat transfer measurements in short duration hypersonic facilities. *AGARD*, AG-165.

Snedden G.C. 1998. *SMR-95 Cascade Aerodynamic Characterisation and Heat Transfer Measurement.* IZMAR 6, CSIR, AEROTEK, Pretoria.

Snedden, G.C. 1995. *Transient measurement of heat transfer in steady state turbine cascades.* MSc dissertation. School of Mechanical Engineering, University of Natal.

Stasiek, J.A. and Kowalewski, T.A. 2002. Thermochromic liquid crystals applied for heat transfer research. *Opto-Electronics Review*, 10 (1), 1-10.

Stieger, R. 1998. *Experimental evaluation of heat transfer distribution on a turbine blade*. MSc dissertation. School of Mechanical Engineering, University of Natal.

Thole, K.A., Bogard, D.G. and Whan-Tong, J.L. 1994. Generating High Freestream Turbulence Levels. *Experiments in Fluids*, 17, 375-380.

Van der Steege, A.W. 1990. *Experimental investigations of special turbine blade cooling configurations*. MSc dissertation. School of Mechanical Engineering, University of Natal.

VKI web site, "http://www.vki.ac.be/", Internet [Accessed: March 2007]

Walker, G. 1997. *Estimation of Unsteady Nonuniform Heating Rates from Surface Temperature Measurements*. PhD dissertation. Virginia Polytechnic Institute and State University, Virginia.

Wang, J.H., Jen, H.F. and Hartel, E.O. 1985. Airfoil heat transfer calculation using a low reynolds number version of a two-equation turbulence model. *ASME Journal of Engineering for Gas Turbines and Power*, 107, 60-67.

Wilcox, D.C. 1998. *Turbulence Modeling for CFD*. DCW Industries Inc, LA California.

Wolfstein, M. 1969. The velocity and temperature distribution of one-dimensional flow with turbulence augmentation and pressure gradient. *International Journal of Heat and Mass Transfer*, 12, 301-318.

APPENDICES

APPENDIX A

A 1.1 SMR-95 BLADE COORDINATES

Table A1-1: SMR-95 Blade Coordinates

SUCTION SURFACE		
	X COORDINATE (MM)	Y COORDINATE (MM)
1	9.383	2.000
2	9.262	2.003
3	9.136	2.009
4	9.000	2.019
5	8.859	2.033
6	8.717	2.051
7	8.583	2.072
8	8.454	2.095
9	8.334	2.120
10	8.216	2.146
11	8.094	2.177
12	7.964	2.213
13	7.827	2.255
14	7.690	2.301
15	7.561	2.348
16	7.440	2.396
17	7.327	2.443
18	7.217	2.492
19	7.102	2.546
20	6.981	2.607
21	6.854	2.675
22	6.724	2.749
23	6.604	2.822
24	6.497	2.890
25	6.397	2.957
26	6.299	3.026
27	6.192	3.105
28	6.085	3.188
29	5.971	3.282
30	5.860	3.378
31	5.756	3.474
32	5.664	3.564
33	5.580	3.649
34	5.499	3.737
35	5.411	3.836
36	5.318	3.947
37	5.228	4.061
38	5.142	4.177
39	5.068	4.283
40	4.999	4.388

PRESSURE SURFACE		
	X COORDINATE (MM)	Y COORDINATE (MM)
235	97.861	31.162
236	97.770	30.997
237	97.655	30.864
238	97.518	30.764
239	97.361	30.699
240	97.186	30.669
241	96.995	30.675
242	94.849	31.137
243	92.700	31.587
244	90.548	32.026
245	88.395	32.456
246	86.240	32.876
247	84.082	33.278
248	83.600	33.364
249	83.112	33.450
250	82.549	33.547
251	81.918	33.653
252	81.328	33.751
253	80.804	33.836
254	80.263	33.922
255	79.750	34.002
256	79.240	34.080
257	78.711	34.159
258	78.163	34.240
259	77.579	34.324
260	76.998	34.406
261	76.434	34.484
262	75.909	34.555
263	75.403	34.621
264	74.895	34.686
265	74.372	34.751
266	73.782	34.823
267	73.224	34.889
268	72.708	34.949
269	72.180	35.008
270	71.602	35.072
271	71.042	35.132
272	70.605	35.177
273	70.053	35.233
274	69.484	35.289

Table A1-1 (continued)

	Suction Surface	
	X Coordinate (mm)	Y Coordinate (mm)
41	4.937	2.486
42	4.871	4.596
43	4.807	4.709
44	4.745	4.824
45	4.678	4.955
46	4.629	5.057
47	4.558	5.215
48	4.481	5.399
49	4.435	5.523
50	4.403	5.624
51	4.387	5.685
52	4.362	5.792
53	4.340	5.889
54	4.279	6.167
55	4.264	6.237
56	4.250	6.302
57	4.218	6.451
58	4.210	6.488
59	4.160	6.726
60	4.072	7.173
61	4.003	7.583
62	3.958	7.924
63	3.932	8.197
64	3.909	8.517
65	3.891	8.770
66	3.860	9.224
67	3.829	9.677
68	3.761	10.563
69	3.693	11.449
70	3.634	12.238
71	3.596	12.745
72	3.574	13.077
73	3.537	13.800
74	3.501	14.682
75	3.469	15.819
76	3.453	16.607
77	3.445	17.268
78	3.441	18.056
79	3.446	18.896
80	3.457	16.552
81	3.477	20.320
82	3.507	21.099
83	3.553	21.972
84	3.600	22.695
85	3.659	23.442
86	3.732	24.224
87	3.821	25.037
88	3.911	25.764
89	4.011	26.486

	Pressure Surface	
	X Coordinate (mm)	Y Coordinate (mm)
275	68.857	35.348
276	68.401	35.389
277	67.858	35.435
278	67.266	35.483
279	66.668	35.528
280	66.251	35.557
281	65.761	35.589
282	65.100	35.628
283	64.477	35.661
284	64.143	35.677
285	63.659	35.697
286	63.233	35.713
287	62.283	35.742
288	61.192	35.766
289	60.066	35.775
290	58.941	35.768
291	57.891	35.748
292	56.984	35.722
293	56.566	35.708
294	56.027	35.687
295	55.697	35.672
296	55.200	35.647
297	54.564	35.612
298	54.027	35.58
299	53.505	35.546
300	53.050	35.513
301	52.463	35.467
302	51.918	35.421
303	51.317	35.364
304	50.829	35.314
305	50.300	35.254
306	49.743	35.186
307	49.136	35.106
308	48.590	35.028
309	48.071	34.950
310	47.528	34.862
311	46.967	34.766
312	46.410	34.665
313	45.872	34.562
314	45.334	34.454
315	44.812	34.344
316	44.282	34.227
317	43.755	34.105
318	43.196	33.971
319	42.675	33.841
320	42.190	33.715
321	41.672	33.576
322	41.120	33.424
323	40.556	33.262

Table A1-1 (continued)

	Suction Surface	
	X Coordinate (mm)	Y Coordinate (mm)
90	4.133	27.291
91	4.266	28.081
92	4.392	28.773
93	4.536	29.506
94	4.700	30.285
95	4.883	31.097
96	5.045	31.764
97	5.240	32.518
98	5.447	33.263
99	5.687	34.066
100	5.900	34.731
101	6.143	35.441
102	6.415	36.181
103	6.723	36.965
104	4.012	37.655
105	7.312	38.332
106	7.647	39.045
107	8.005	39.764
108	8.351	40.422
109	8.717	41.082
110	9.110	41.756
111	9.529	42.436
112	9.931	43.056
113	10.362	43.689
114	10.811	44.315
115	11.296	44.957
116	11.767	45.549
117	12.259	46.136
118	12.769	46.713
119	13.307	47.290
120	13.846	47.838
121	14.391	48.365
122	14.962	48.888
123	15.548	49.395
124	16.754	50.368
125	17.370	50.827
126	17.994	51.267
127	18.637	51.697
128	19.291	52.110
129	19.940	52.497
130	20.618	52.880
131	21.333	53.260
132	22.034	53.608
133	22.709	53.923
134	23.388	54.218
135	24.149	54.527
136	24.871	54.798
137	25.599	55.051
138	26.281	55.272

	Pressure Surface	
	X Coordinate (mm)	Y Coordinate (mm)
324	40.090	33.124
325	39.553	32.959
326	39.029	32.792
327	38.461	32.604
328	37.998	32.445
329	37.491	32.262
330	36.967	32.066
331	36.401	31.845
332	35.906	31.644
333	35.421	31.439
334	34.911	31.214
335	34.385	30.974
336	33.890	30.740
337	33.406	30.501
338	32.913	30.251
339	32.421	29.991
340	31.947	29.732
341	31.473	29.464
342	30.995	29.185
343	30.517	28.897
344	30.059	28.611
345	29.599	28.315
346	29.139	28.009
347	28.680	27.694
348	28.244	27.385
349	27.803	27.062
350	27.361	26.729
351	26.918	26.383
352	26.500	26.046
353	26.080	25.698
354	25.660	25.338
355	25.240	24.966
356	24.844	24.604
357	24.448	24.230
358	24.054	23.846
359	23.656	23.445
360	23.277	23.050
361	22.904	22.649
362	22.539	22.243
363	22.175	21.823
364	21.820	21.399
365	21.476	20.975
366	21.138	20.543
367	20.807	20.105
368	20.476	19.652
369	20.161	19.204
370	19.853	18.752
371	19.556	18.300
372	19.255	17.825

Table A1-1 (continued)

	Suction Surface	
	X Coordinate (mm)	Y Coordinate (mm)
139	27.079	55.511
140	27.827	55.718
141	28.569	55.908
142	29.254	56.070
143	30.042	56.241
144	30.827	56.396
145	31.560	56.542
146	33.064	56.754
147	33.852	56.850
148	34.583	56.926
149	35.335	56.991
150	36.194	57.050
151	36.982	57.088
152	37.732	57.111
153	38.410	57.120
154	39.254	57.118
155	40.023	57.104
156	40.813	57.080
157	41.485	57.051
158	42.330	57.005
159	43.135	56.951
160	43.872	56.886
161	45.333	56.760
162	46.149	56.671
163	46.871	56.584
164	47.612	56.487
165	48.426	56.371
166	49.203	56.250
167	49.935	56.127
168	50.650	55.999
169	51.521	55.834
170	52.283	55.681
171	53.037	55.522
172	53.665	55.384
173	54.504	55.193
174	55.272	55.011
175	56.026	54.828
176	56.658	54.671
177	57.450	54.469
178	58.253	54.258
179	58.959	54.069
180	59.632	53.885
181	60.359	53.681
182	61.132	53.459
183	61.843	53.249
184	62.587	53.025
185	63.386	52.779
186	64.130	52.544
187	64.837	52.315

	Pressure Surface	
	X Coordinate (mm)	Y Coordinate (mm)
373	18.966	17.353
374	18.688	16.883
375	18.424	16.419
376	18.158	15.934
377	17.900	15.447
378	17.652	14.958
379	17.412	14.469
380	17.173	13.962
381	16.944	13.457
382	16.714	12.926
383	16.521	12.462
384	15.754	10.405
385	15.110	8.305
386	14.891	7.231
387	14.741	6.648
388	14.592	6.171
389	14.406	5.626
390	14.238	5.155
391	14.210	5.086
392	14.161	4.980
393	14.092	4.845
394	13.985	4.659
395	13.896	4.512
396	13.845	4.431
397	13.779	4.331
398	13.715	4.238
399	13.640	4.133
400	13.551	4.017
401	13.465	3.909
402	13.379	3.807
403	13.298	3.715
404	13.214	3.625
405	13.129	3.537
406	13.053	3.444
407	12.937	3.353
408	12.833	3.260
409	12.723	3.168
410	12.617	3.084
411	12.517	3.009
412	12.420	2.939
413	12.320	2.871
414	12.207	2.798
415	12.087	2.724
416	11.958	2.650
417	11.827	2.580
418	11.704	2.518
419	11.590	2.464
420	11.481	2.417
421	11.370	2.371

Table A1-1 (continued)

	Suction Surface	
	X Coordinate (mm)	Y Coordinate (mm)
188	65.518	52.091
189	66.334	51.817
190	67.065	51.566
191	67.798	51.310
192	68.426	51.088
193	69.227	50.800
194	69.969	50.530
195	70.693	50.263
196	71.316	50.031
197	72.050	49.755
198	72.813	49.464
199	73.513	49.194
200	74.189	48.931
201	74.876	48.661
202	75.612	48.367
203	76.308	48.087
204	77.045	47.787
205	77.787	47.481
206	78.505	47.182
207	79.176	46.898
208	79.882	46.597
209	80.694	46.247
210	81.408	45.934
211	82.095	45.631
212	82.700	45.361
213	83.512	44.995
214	84.221	44.673
215	84.947	44.341
216	85.500	44.087
217	86.273	43.729
218	87.013	43.385
219	87.693	43.067
220	88.289	42.787
221	88.981	42.461
222	89.745	42.098
223	90.403	41.784
224	91.067	41.466
225	93.834	40.120
226	96.589	38.750
227	99.332	37.358
228	99.483	37.244
229	99.599	37.112
230	99.680	36.964
231	99.724	36.802
232	99.731	36.628
233	99.699	36.444
234	98.780	33.803

	Pressure Surface	
	X Coordinate (mm)	Y Coordinate (mm)
422	11.244	2.322
423	11.108	2.274
424	10.964	2.227
425	10.821	2.185
426	10.687	2.150
427	10.559	2.120
428	10.442	2.096
429	10.323	2.074
430	10.196	2.054
431	10.058	2.036
432	9.913	2.021
433	9.771	2.010
434	9.636	2.003
435	9.506	2.000

A 1.2 Blade Measurement Positions

The positions of the thin-film gauges on the SMR-95 blade are shown in Table A1-2, and the pressure tapping points in Table A1-3. The circumferential distances are relative to the leading edge (LE) of the blade. The positions are given over the suction surface to the trailing edge (TE), and then back along the pressure surface to the leading edge sensor/tapping.

Table A1-2: SMR-95 Blade Sensor Positions

Sensor Number	Circumferential Distance (mm)	D-Type Connector
(LE) 1	0.3	**P1:** 1
2	3.5	2
3	6.9	3
4	13	4
5	18.1	5
6	23.1	6
7	28.3	7
8	33	8
9	37.8	**P2:** 1
10	43.1	2
11	48.3	3
12	53.3	4
13	58.4	5
14	64.3	6
15	69.4	7
16	74.6	8
17	79.5	**P3:** 1
18	84.5	2
19	88.7	3
20	94.4	4
21	99.7	5
22	105.4	6
23	110.5	7
24	115.4	8
25	121	**P4:** 1
26	126.6	2
27	131.5	3
28	136.5	4

Table A1-2 (continued)

Sensor Number	Circumferential Distance (mm)	D-Type Connector
(TE) 29	107	5
30	98.2	6
31	92.8	7
32	87.6	8
33	81.9	**P5:** 1
34	76.2	2
35	70.8	3
36	66	4
37	60.4	5
38	55	6
39	49	7
40	44.5	8
41	38.9	**P6:** 1
42	33.5	2
43	28.2	3
44	22.7	4
45	17.3	5
46	12	6
47	6.7	7
48	3.7	8

Table A1-3: SMR-95 Blade Pressure Tapping Positions

Pressure Tapping	Circumferential Distance (mm)
(LE) 1	0
2	7.7
3	20
4	31
5	39
6	45.4
7	50.8
8	56.1
9	60.7
10	65.7
11	70.5

Table A1-3 (continued)

PRESSURE TAPPING	CIRCUMFERENTIAL DISTANCE (MM)
12	75.4
13	80.4
14	85.6
15	90.8
16	96.5
17	102.3
18	108.3
19	114.5
20	120.9
21	127.4
22	133.9
23	141
(TE) 24	101.5
25	96
26	90.5
27	85.1
28	79.5
29	74.4
30	69.4
31	64.2
32	59.2
33	54.4
34	49.6
35	45
36	40
37	35.5
38	30.4
39	24.6
40	19.4
41	12.7
42	7

APPENDIX B

CFD STATIC PRESSURE RESULTS
(FLUENT CONTOUR PLOTS)

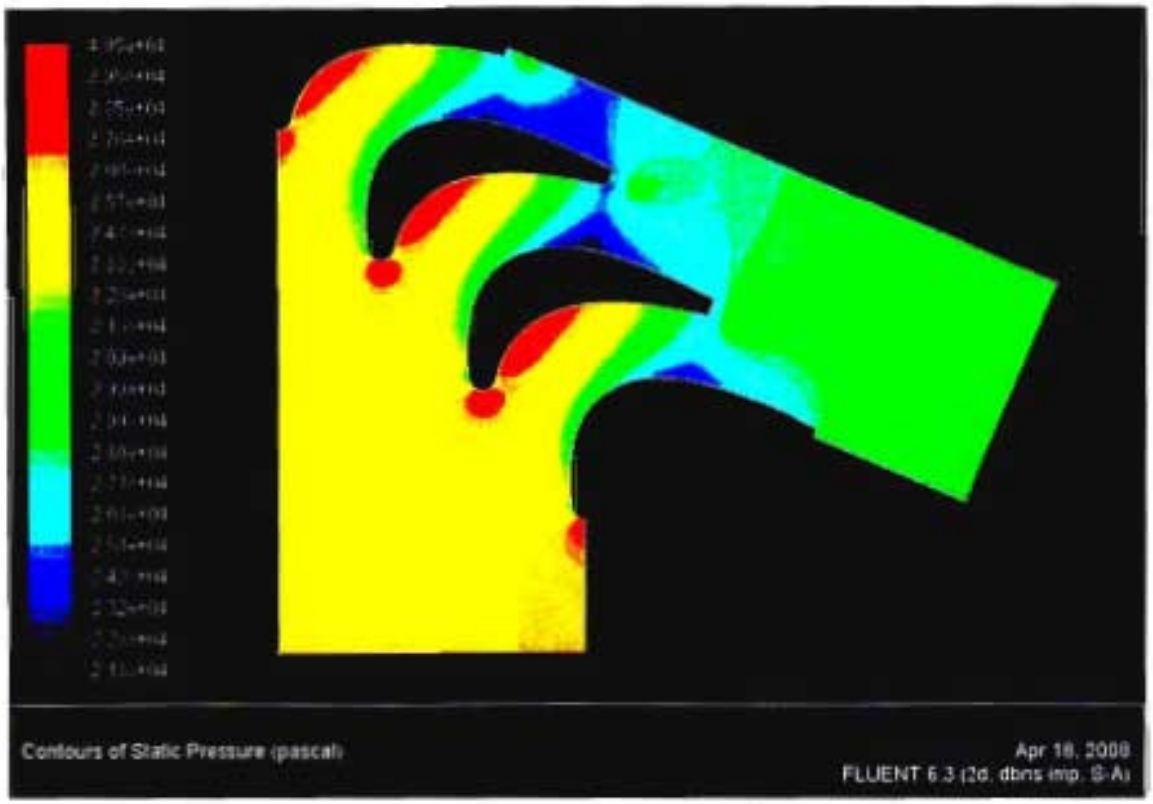

Figure B1-1: Static pressure contours of the Spalart-Allmaras model at Tu = 3%

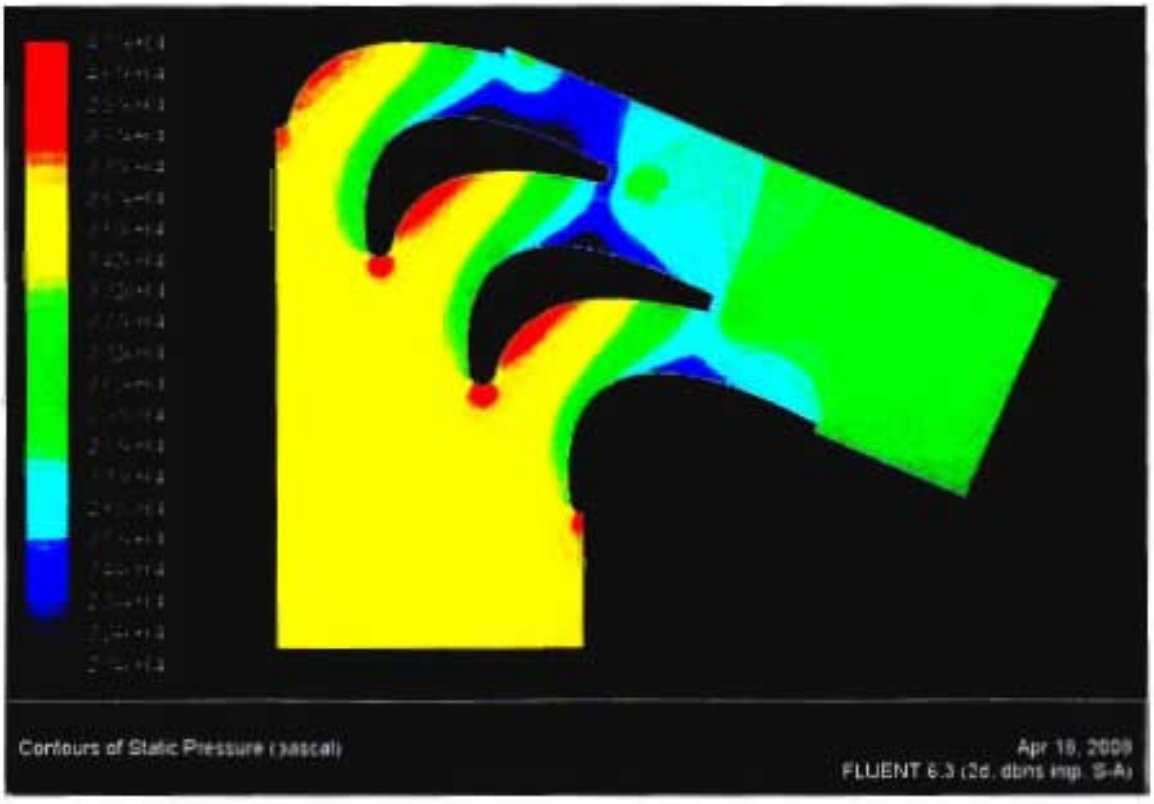

Figure B1-2: Static pressure contours of the Spalart-Allmaras model at Tu = 15%

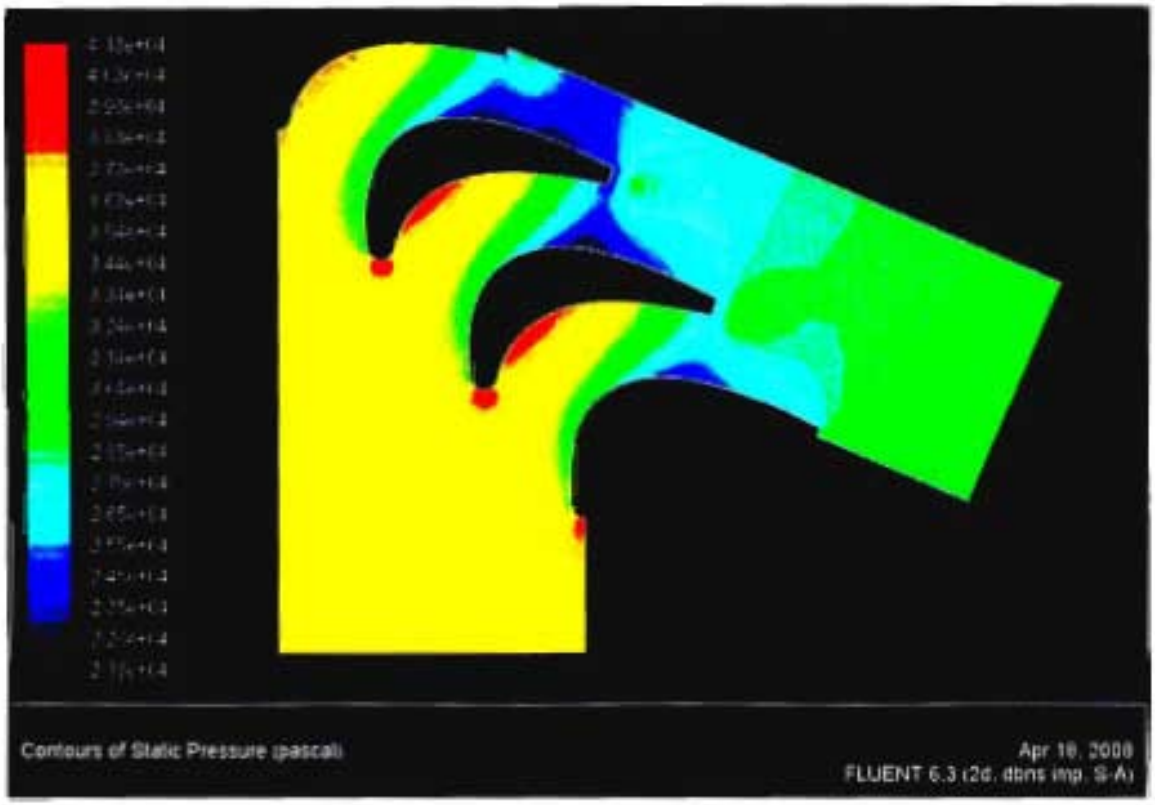

Figure B1-3: Static pressure contours of the Spalart-Allmaras model at Tu = 25.5%

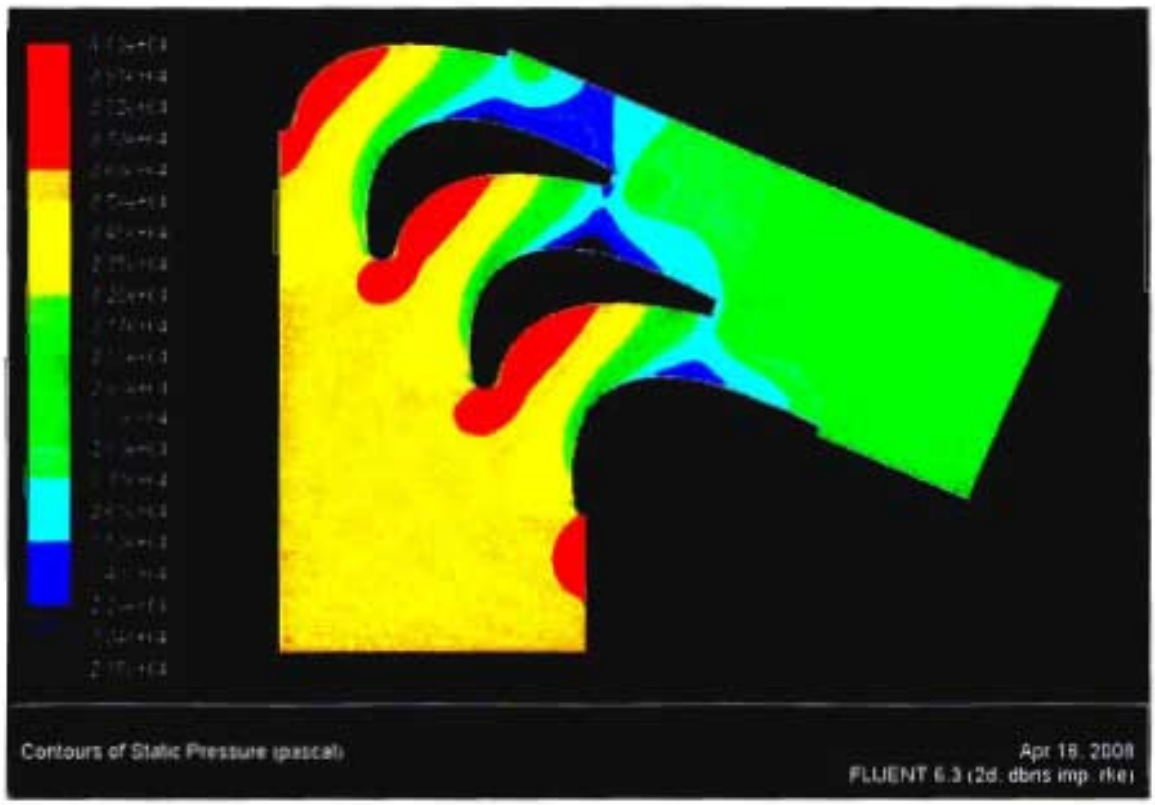

Figure B1-4: Static pressure contours of the Realisable k-ε model at Tu = 3%

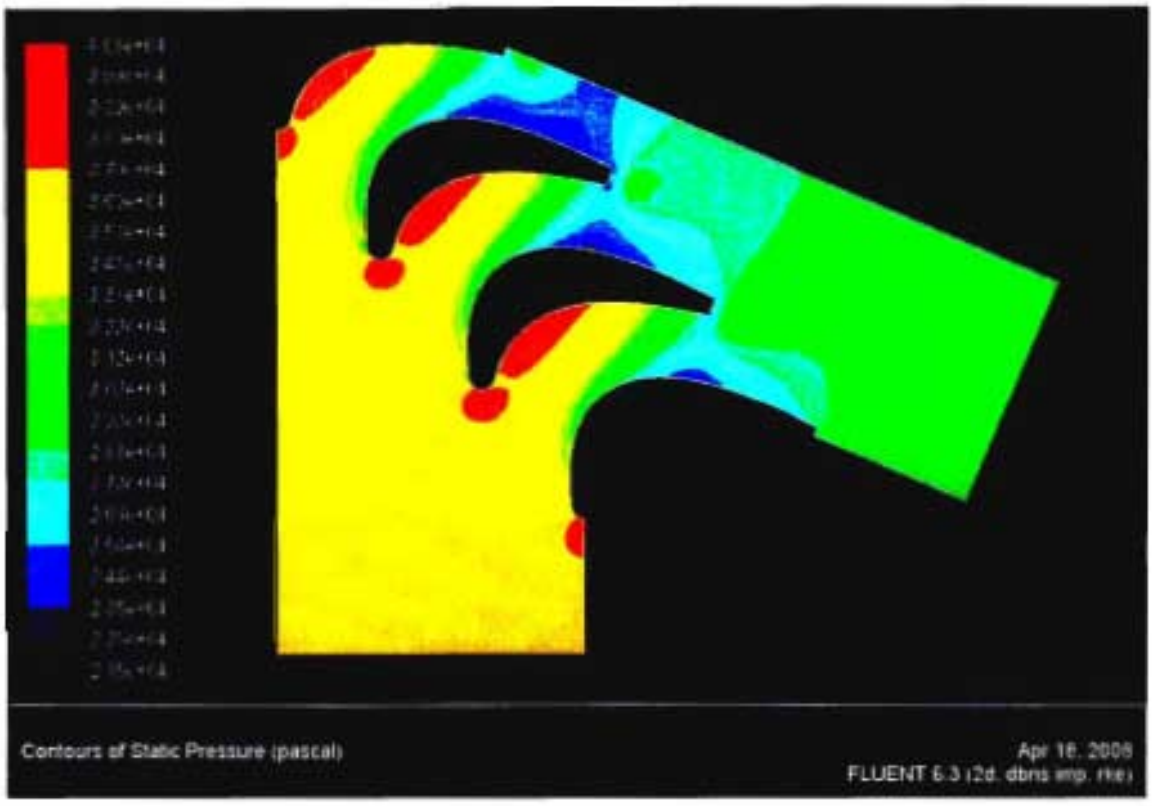

Figure B1-5: Static pressure contours of the Realisable k-ε model at Tu = 15%

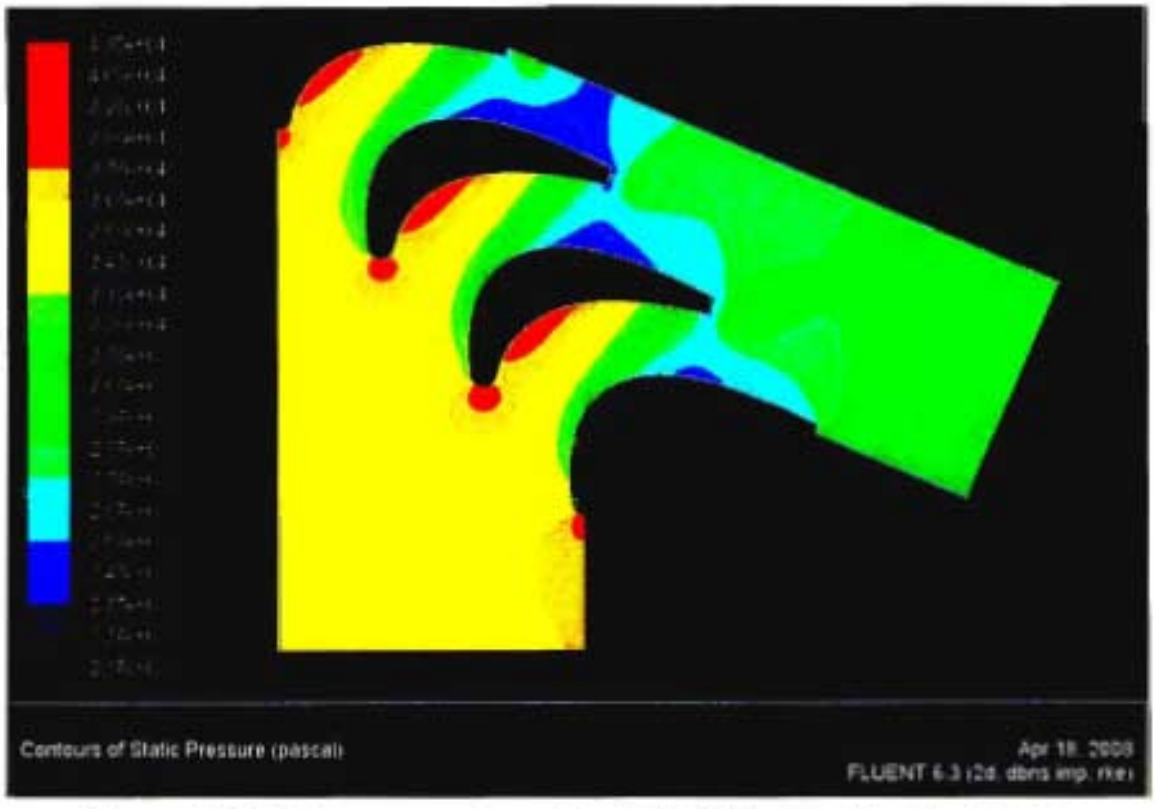

Figure B1-6: Static pressure contours of the Realisable k-ε model at Tu = 25.5%

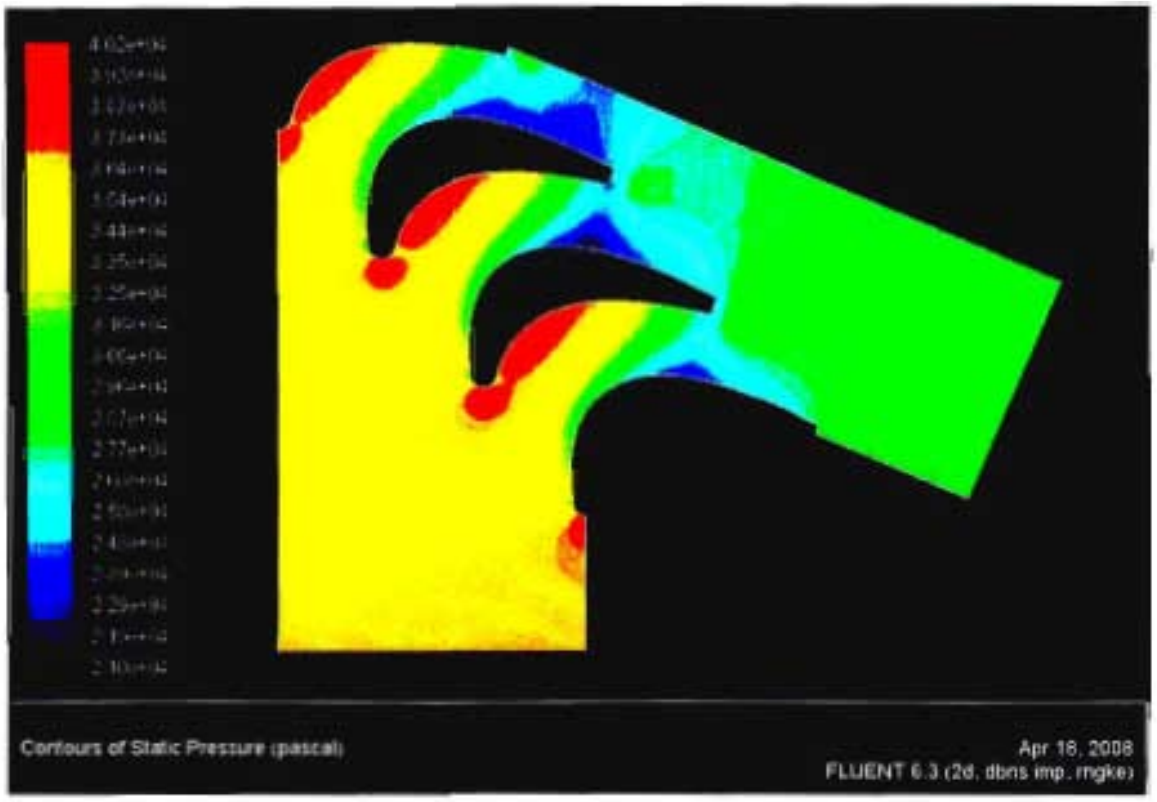

Figure B1-7: Static pressure contours of the RNG k-ε model at Tu = 3%

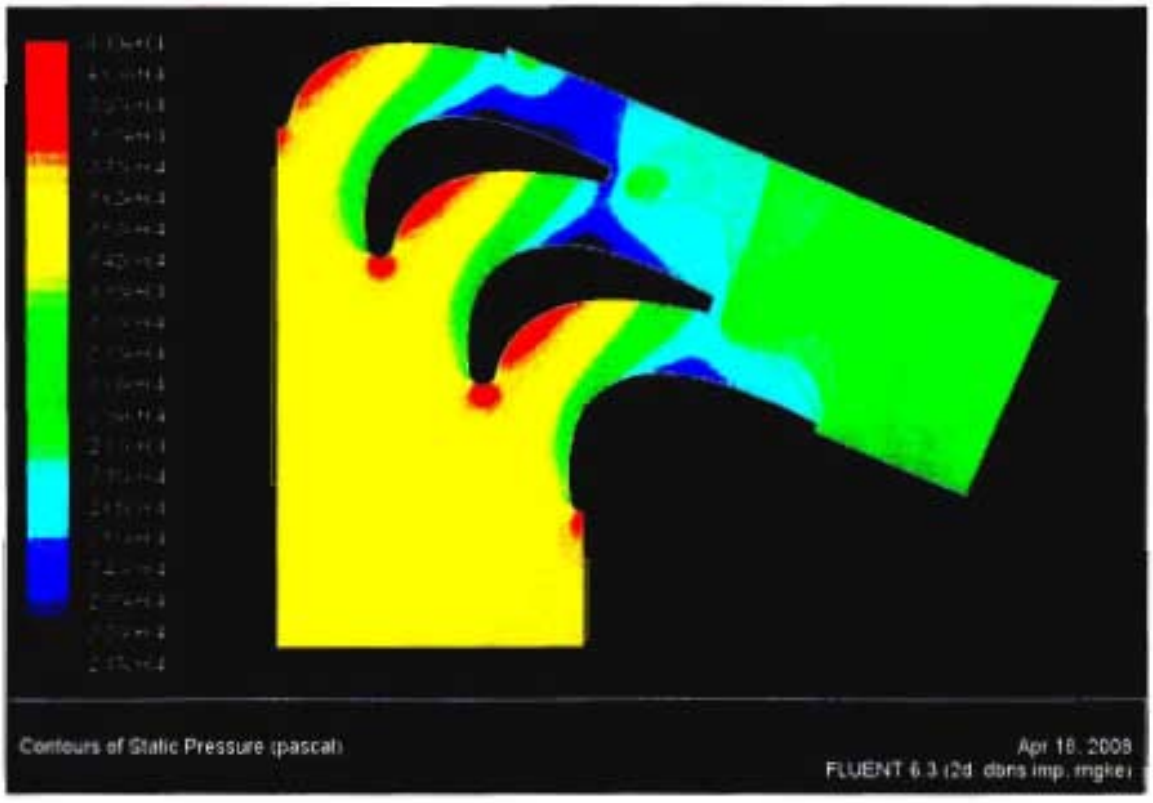

Figure B1-8: Static pressure contours of the RNG k-ε model at Tu = 15%

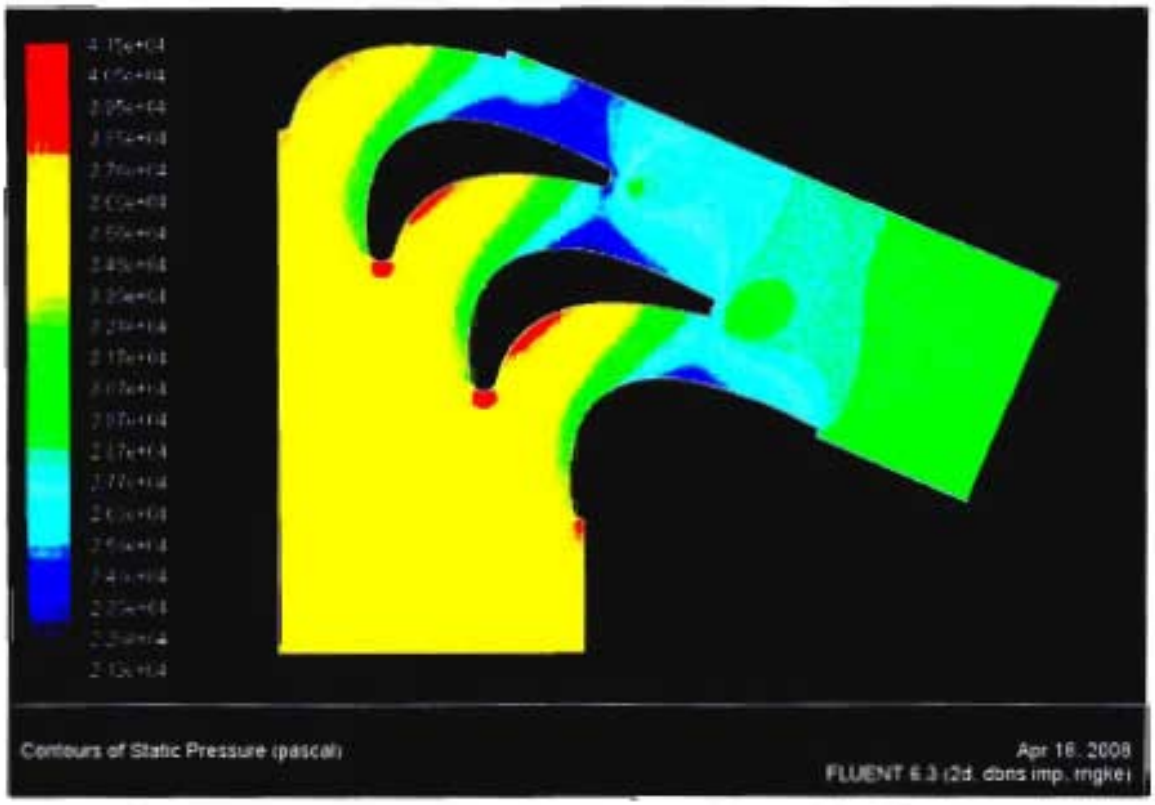

Figure B1-9: Static pressure contours of the RNG k-ε model at Tu = 25.5%

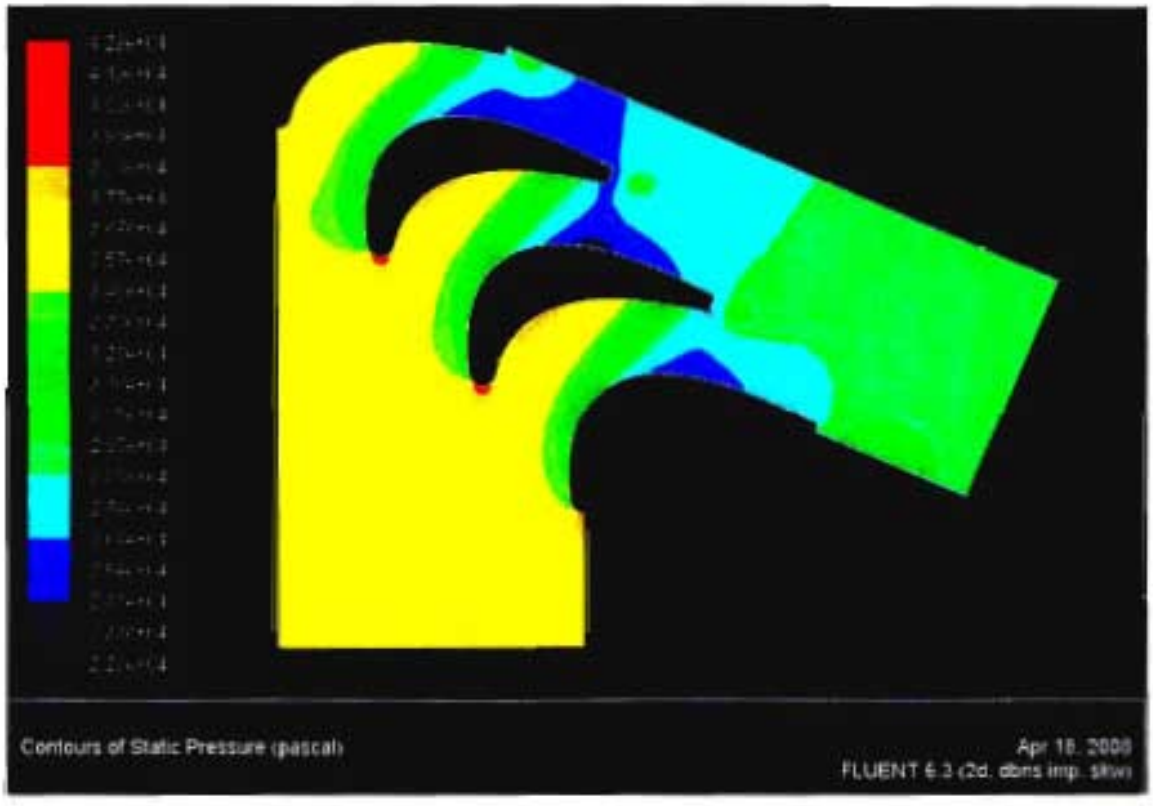

Figure B1-10: Static pressure contours of the standard k-ω model at Tu = 3%

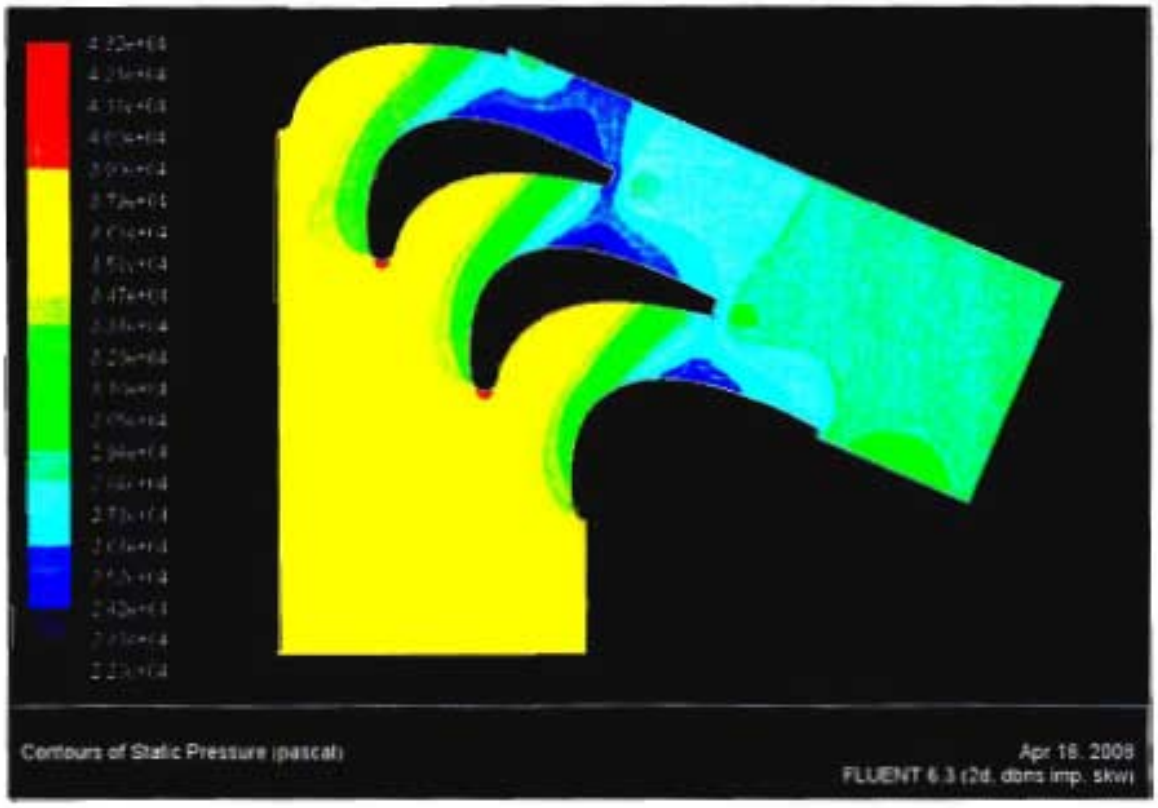

Figure B1-11: Static pressure contours of the standard k-ω model at Tu = 15%

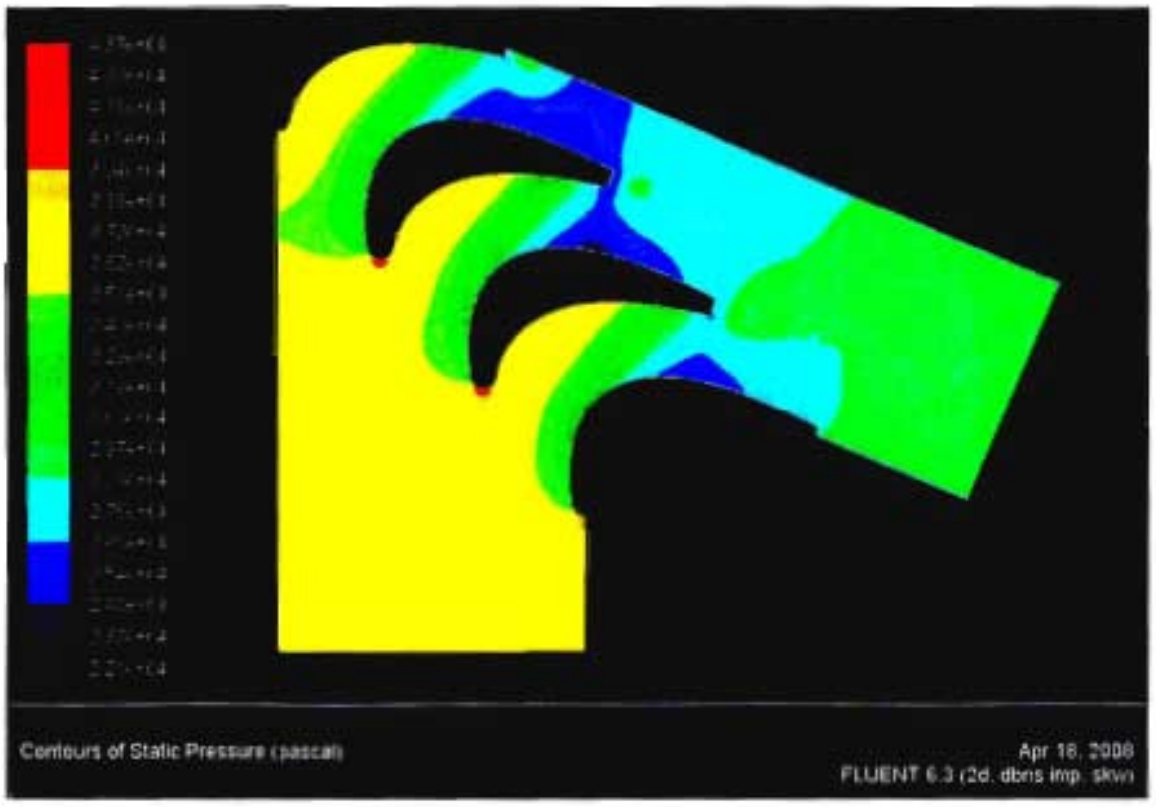

Figure B1-12: Static pressure contours of the standard k-ω model at Tu = 25.5%

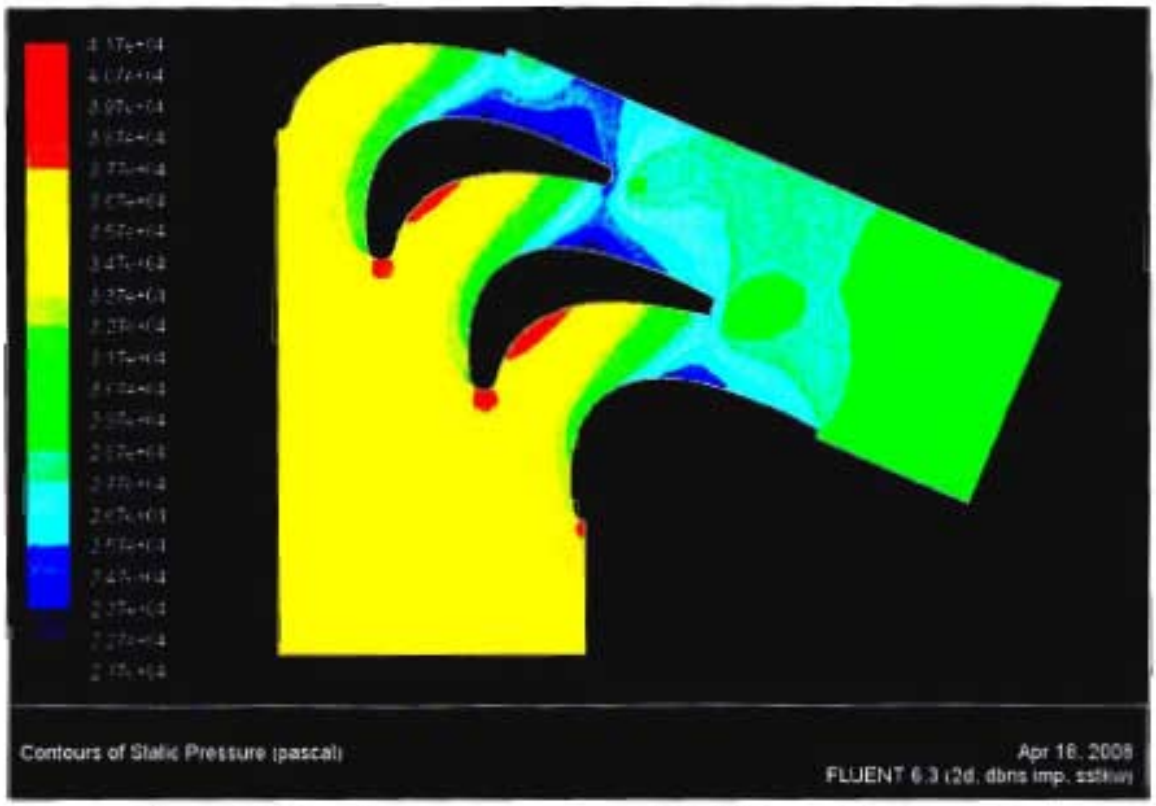

Figure B1-13: Static pressure contours of the SST k-ω model at Tu = 3%

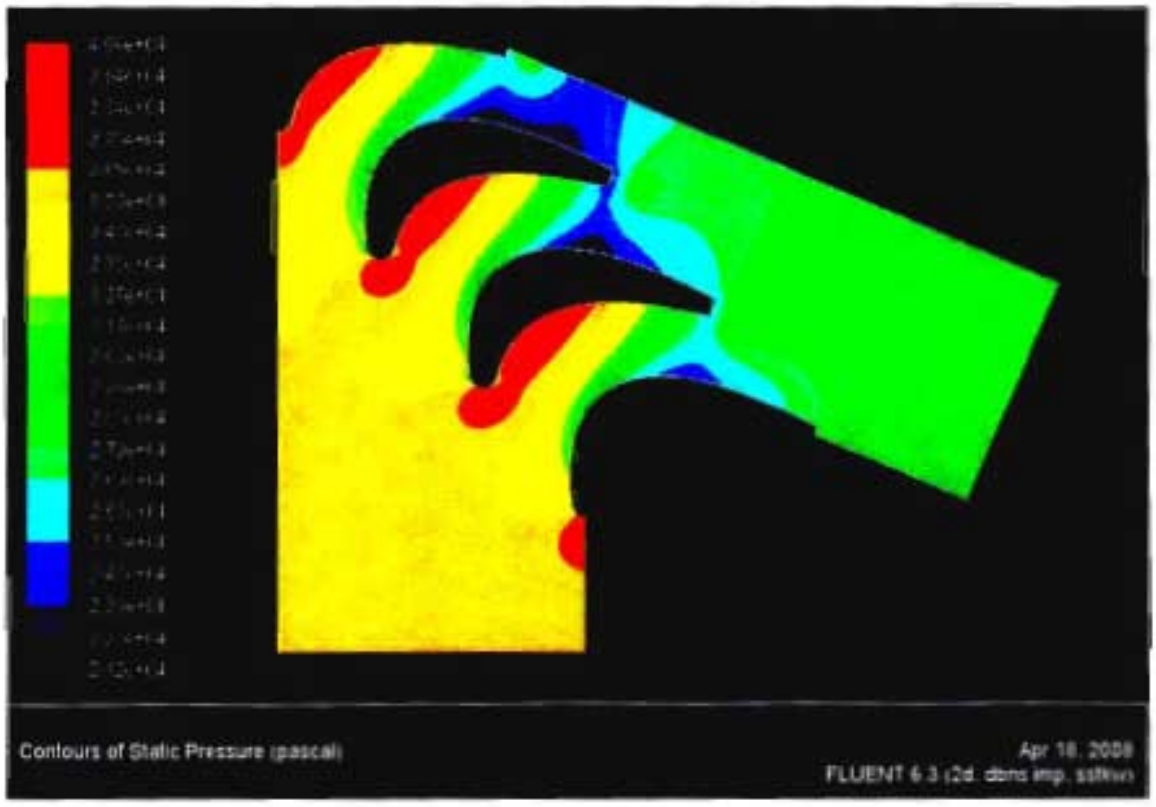

Figure B1-14: Static pressure contours of the SST k-ω model at Tu = 15%

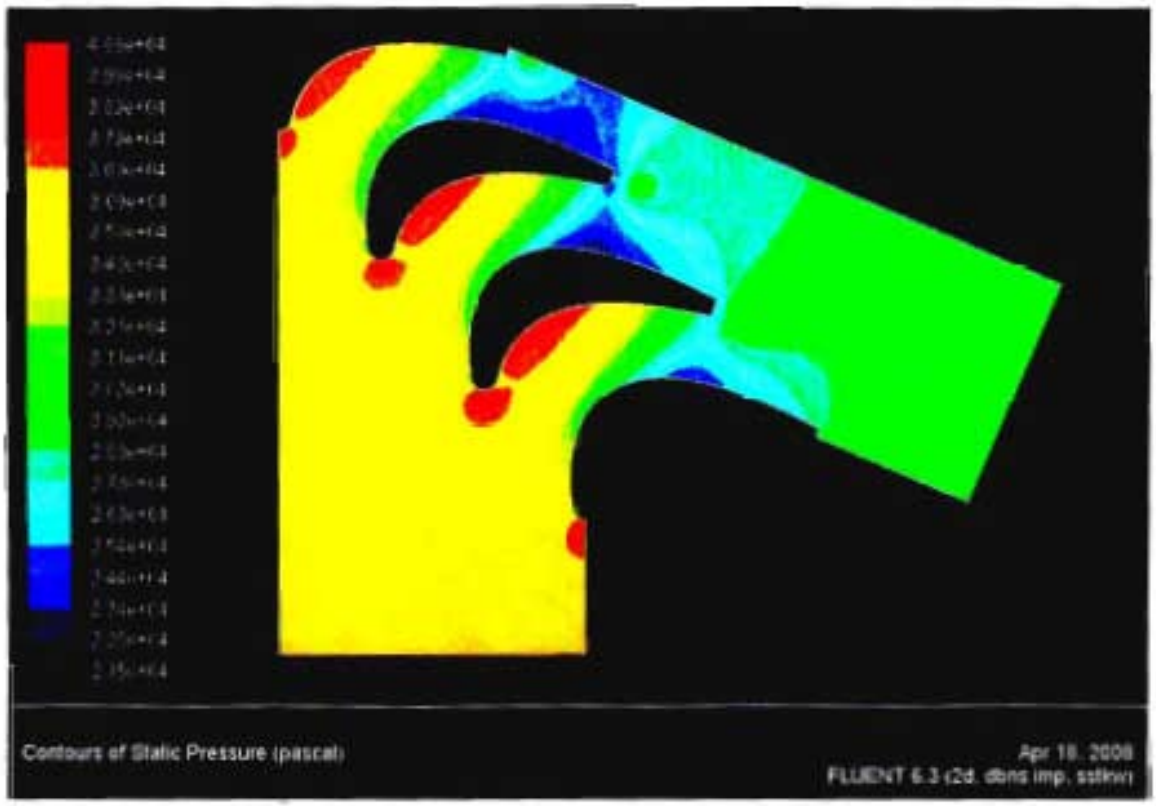

Figure B1-15: Static pressure contours of the SST k-ω model at Tu = 25.5%

APPENDIX C

The following experimental procedures and calibration procedures were already drawn up by Cassie (2006) and de Villiers (2002). The experimental facility and operating conditions were unchanged, thus these procedures were used with minor improvements.

C 1.1 EXPERIMENTAL RIG START UP PROCEDURE

1) Turn on the safety control box, display box and pressure control box.
2) Seal the plenum at all locations and start the vacuum pump.
3) Turn on the Hydrovane compressor to supply air to the pneumatic motor that is used for circulating the oil for gearbox lubrication.
4) Switch on the immersion heater located within the airpack to heat the gearbox oil to an operating temperature range between 50 – 70 °C.
5) Start the air pump. (Note: The oil flow, oil pressure and air pressure interlocks on the safety control box should deactivate and all illuminate green)
6) If the oil flow interlock does not deactivate, twist the oil flow meter until deactivated (faulty wiring).
7) Check that cooling water is available from the roof mounted reservoir by turning a stop cock valve on the heat exchanger used to cool the gearbox oil and seeing if there is water flow.
8) Once the total pressure inside the plenum reaches 0.55 bar and gearbox oil temperature of around 50 °C, the hydraulic motor can be started up successfully.
9) The start up procedure for the hydraulic motor involves ensuring that the swash-plate is in its neutral position, checking that there is an adequate amount of hydraulic oil, and that the hydraulic pump circuitry is switched to "Sonic".
10) After a fault-free system has been displayed on the main power box, the prime pump can be started, and then the main hydraulic pump.
11) To shut down the rig, these steps must be followed in reverse order.

C 1.2 Pressure Testing Setup and Procedure

1) Setup of the Cascade and Plenum for Pressure Measurements

   a) Insert the pressure measurement test blade into the cascade and fix the blade in place by bolting it to a plate on the base of the cascade box.
   b) Attach the cascade to the diffuser and fix it by bolting the four ends.
   c) Attach the pressure measurement cover plates to the plenum and connect the silicon tubes to the test blade, as well as tubes to the static inlet and outlet tappings on the cascade box.
   d) Attach the other ends of the silicon tubes to their respective scanivalve ports.
   e) Connect the Kiel pressure probe (which measures the total inlet pressure of the cascade) to the inlet copper tube of the cascade using a silicon tube.
   f) Close and seal the dished end.

2) Setup of Instrumentation for Pressure Results

   a) Attach a 24 V power supply to the scanivalve.
   b) Connect both Rosemount pressure transducers and the Kulite pressure transducer to the scanivalve to ensure that power is supplied.
   c) Connect the common ports on the scanivalve wafers to the low pressure side of the Rosemount transducer using silicon tubes.
   d) Connect silicon tubes from the Kulite pressure transducer to the high pressure side of the Rosemount transducers and the balance pressure port of the scanivalve.
   e) Make sure the U-tube manometer is also connected to further measure the total plenum pressure.

3) Setup of the Data Acquisition System

   a) Connect the PC 71 card to the PC 30 PGL card (located on the motherboard of the computer) using a D-type ribbon cable.
   b) Connect channels CH 0-3 as well as the GND of the PC 71 card to the scanivalve, and ensure the PC 71 card is correctly grounded to the PC casing.
   c) On the ports of the PC 71 card, connect GND, A 0-4 and B 0, representing the binary equivalent of the position of the scanivalve and the output voltage used to step the scanivalve.
   d) Ensure the voltage range is set to 0-10 V by jumper settings on the PC 30 card (illustrated in the PC 30 user manual).
   e) Start the PC, run the program "Pressure", then select "Winfin" from the VI list.

4) EXPERIMENTAL RIG OPERATING PROCEDURE TO ACQUIRE DATA

a) Follow the general rig start up procedure outlined in C 1.1.
b) Set the speed of the compressor blade to run at 2500 rpm.
c) Once the temperature inside the plenum rises to around 100 °C, vary the radiator cooling water flow rate carefully such that the temperature remains constant.
d) Once the desired operating conditions have been reached, and are stable, the data can be captured using the LabView software command "Perform Measurement".

C 1.3 HEAT TRANSFER TESTING SETUP AND PROCEDURE

1) SETUP OF THE CASCADE

a) Fasten the heat transfer blade stack to the sliding plate on the sliding mechanism.
b) Insert the blade stack into the cascade through the endwall, and fasten the sliding mechanism to the bottom of the cascade. Care must be taken to not scratch the sensors.
c) Attach the cooling box and perforated copper plate to the top of the cascade.
d) Fill the cooling box with insulating foam.
e) Connect the pneumatic ram through the top of the cooling box lid and screw into the top of the blade.
f) Fasten the pneumatic ram to the cascade box.
g) Attach the cascade to the diffuser and fix the ends with bolts.
h) Connect the cooling pipes from the blower to the corresponding inlets of the cooling box.
i) Connect the respective compressed air line pipes to the pneumatic cylinder.

2) SETUP OF THE INSTRUMENTATION

a) Run the heat flux sensor flying leads through one of the specially made cover ports and seal with silicon.
b) Connect the total inlet, static inlet and outlet pressure tappings of the cascade to their respective ports as describe in C 1.2, with the output voltages captured using a digital multimeter.
c) Connect the total inlet temperature thermocouple to the temperature display box.

d) Connect the blade thermocouples to the Fluke K/J digital thermometers.
e) Close and seal the dished end.
f) Ensure the voltage range of the PC 30 card is set to a range of -5 to +5 V by the corresponding jumper settings (illustrated by the PC 30 user manual).
g) Ensure the PC 71 interface card is correctly grounded to the casing of the PC.
h) Run the program WaveView, and ensure that all the initial voltage outputs of the analogue cards are settled on 0 V by adjusting the DC offset screws.

3) EXPERIMENTAL RIG OPERATING PROCEDURE TO ACQUIRE DATA

a) Follow the general rig start up procedure outlined in C 1.1.
b) Start up the blower to cool the blade inside the cooling box.
c) Increase the compressor blade speed to 2500 rpm.
d) Once the temperature inside the plenum has risen to 100 °C, adjust the cooling water flow rate through the radiator to maintain this temperature.
e) Once operating conditions are reached at 40 kPa, and are stable, record total pressure and static inlet and outlet pressures, as well as the compressor speed.
f) Record the total temperature, and the internal blade temperatures.
g) Ensure the correct D-type cable is connected to the analogue cards.
h) Record the initial resistances of the sensors with the power supply turned off.
i) Record the initial voltages of the sensors on the blade using the selector box to switch between sensors more efficiently, and with the power supply turned on.
j) Switch off the blower to ensure no additional electrical noise in the data output.
k) Start sampling the data using WaveView, and plunge the blade stack into the hot air stream.
l) Once the data has been sampled, retract the blade into the cooling box, restart the blower, and save the output data to a text file.
m) Wait until the internal blade temperatures have reached the initial temperature required of 40 °C (which may require reducing the compressor speed for faster cooling, then increasing the speed again to the operating conditions).
n) Connect the next D-type connector to the analogue cards and return to part "e".

The experimental template to record the values and data for each experimental run is given in Table C1-1.

Table C1-1: Template Used for Experimental Heat Transfer Tests

PLUG	SENSOR	CIRCUM POS	RES FOR 40 °C	α_R	INITIAL VOLT	INITIAL RES	RPM/INLET TEMP
P1	1	0.3	143.742	9.100E-04			RPM=
	2	3.5	53.060	9.103E-04			Blade Temps=
	3	6.9	66.265	9.145E-04			Cascade Temp=
	4	13	63.139	9.630E-04			Total Pressure=
	5	18.1	50.226	8.840E-04			Notes:
	6	23.1	55.333	9.090E-04			
	7	28.3	53.326	8.889E-04			
	8	33	51.911	8.823E-04			
P2	1	37.8	52.833	8.839E-04			RPM=
	2	43.1	53.765	9.002E-04			Blade Temps=
	3	48.3	55.111	8.565E-04			Cascade Temp=
	4	53.3	51.894	8.941E-04			Total Pressure=
	5	58.4	51.709	8.993E-04			Notes:
	6	64.3	52.980	9.192E-04			
	7	69.4	48.960	8.864E-04			
	8	74.6	132.940	9.591E-04			
P3	1	79.5	52.277	9.124E-04			RPM=
	2	84.5	51.806	9.111E-04			Blade Temps=
	3	88.7	52.140	9.129E-04			Cascade Temp=
	4	94.4	51.318	9.178E-04			Total Pressure=
	5	99.7	51.549	9.137E-04			Notes:
	6	105.4	52.093	9.349E-04			
	7	110.5	70.953	9.584E-04			
	8	115.4	123.150	9.338E-04			
P4	1	121	52.852	8.817E-04			RPM=
	2	126.6	52.824	8.822E-04			Blade Temps=
	3	131.5	64.932	9.441E-04			Cascade Temp=
	4	136.5	58.762	8.917E-04			Total Pressure=
	5	-107	52.918	9.675E-04			Notes:
	6	-98.2	52.179	9.391E-04			
	7	-92.8	64.932	9.441E-04			
	8	-87.6	61.138	9.143E-04			
P5	1	-81.9	60.508	9.569E-04			RPM=
	2	-76.2	55.420	9.636E-04			Blade Temps=
	3	-70.8	71.083	9.749E-04			Cascade Temp=
	4	-66	67.022	9.758E-04			Total Pressure=
	5	-60.4	52.758	8.586E-04			Notes:
	6	-55	54.852	9.899E-04			
	7	-49	52.587	9.261E-04			
	8	-44.5	53.312	9.623E-04			
P6	1	-38.9	52.392	1.002E-03			RPM=
	2	-33.5	51.794	9.461E-04			Blade Temps=
	3	-28.2	53.106	9.302E-04			Cascade Temp=
	4	-22.7	64.025	9.418E-04			Total Pressure=
	5	-17.3	59.165	9.364E-04			Notes:
	6	-12	66.205	1.618E-03			
	7	-6.7	52.632	1.647E-03			
	8	-3.7	52.542	1.439E-03			

C 1.4 ROSEMOUNT PRESSURE TRANSDUCER CALIBRATION

1) SETTING THE RANGE TO 0.4 BAR

   a) Apply zero differential pressure across the Rosemount by leaving both the HP and LP lines of the transducer open to atmosphere.

   b) Adjust the zero calibration screw until and output of 1.88 V is achieved, which should correspond to the lowest output of 4 mA of the transducer.

   c) Apply a pressure of 0.6 bar to the LP side of the Rosemount, thus providing a differential pressure of 0.4 bar.

   d) Adjust the span calibration screw until a maximum of 9.4 V is read by the voltmeter, which corresponds to the highest output of 20 mA.

   e) Repeat the process until the correct voltage range corresponds to the pressure range. Note that it is vital to repeat the process as adjusting the span screw affects the zero setting.

2) PLOT THE CALIBRATION CURVES

   a) Leave the HP side of the Rosemount transducer open to atmosphere and attach the LP side to the total inlet pressure.

   b) Attach the total pressure to a U-tube manometer.

   c) Start the vacuum pump.

   d) Once the vacuum pump is started, activate a stopwatch and record the height of the mercury every 20 s for 200 s.

   e) As the vacuum pump is started, capture the output signal which corresponds to the differential pressure, through channels 0 and 1 on the PC 71 card with WaveView software.

   f) Once the sampling is complete, export the data into a text file (noting that the software recorded the change in voltage signal against time) and extract the voltage signals corresponding to the 20 s time intervals.

   g) Convert the height measurements into pressures using $\Delta P = \rho g h$.

   h) Construct a straight line graph of differential pressure vs. voltage using the gradient and y-intercept as calibration constants to be inputted into the sub VI of the LabView program "Pressure Measurement".

C 1.5 KULITE PRESSURE TRANSDUCER CALIBRATION

1) PLOT THE CALIBRATION CURVES
    a) Attach the total plenum pressure to a U-tube manometer.
    b) Start the vacuum pump.
    c) Once the vacuum pump is started, activate a stopwatch and record the height of the mercury every 20 s for 300 s.
    d) As the vacuum pump is started, capture the output signal which corresponds to the total pressure of the Kulite, through channel 3 on the PC 71 card with the WaveView software.
    e) Once the sampling is complete, export the data to a text file (noting that the software recorded the change in voltage signal against time) and extract the voltage signals corresponding to the 20 s time intervals.
    f) Convert the height measurements into pressures using $\Delta P = \rho g h$.
    g) Construct a straight line graph of total pressure vs. voltage using the gradient and y-intercept as calibration constants to be inputted into the sub VI of the LabView program "Pressure Measurement".

C 1.6 THIN-FILM GAUGE CALIBRATION

1) EXPERIMENTAL SETUP AND PROCEDURE
    a) Place the heat transfer blade stack on ceramic blocks within an industrial convection oven.
    b) Instrument the blade with thermocouples at the front, top and rear sections of the profile.
    c) Run the sensor plugs to the heat transfer analogue (noting that the heat transfer analogue remains unplugged for the duration of the calibration).
    d) Connect the outputs of the selector box to a multimeter to read resistance.
    e) Run the wiring of the heat transfer blade stack through the linings of the door and switch on the oven.
    f) Record the measurements of all the thermocouples as well as the oven display and average for the final temperature.
    g) Record the resistances of all the corresponding sensors by changing the plugs and switching the selector box.

h) Increase the temperature of the oven by approximately 20 °C and repeat steps "f" to "g" up to 100 °C.

i) Input the data into an Excel spreadsheet and calculate the respective calibration constants of α_R and R_0.

C 1.7 Heat Transfer Analogy Calibration

1) Experimental Setup and Procedure

a) Provide a ±15 V supply to the heat transfer analogy and ensure that the blade stack is not connected, creating an open circuit to the heat transfer analogue cards.

b) Connect the PC 71 interface card to the input of the analogy.

c) Run the calibration program "Cal30", which generates a parabolic signal to the heat transfer analogue cards and records the output step voltage.

d) Plot the step output voltage in Excel and calculate the amplitude of the step.

e) Repeat the calibration process to determine the average circuit calibration constant (as the signal is very noisy).

f) Switch to the next heat transfer analogue card at the housing and repeat steps "a" to "e".

APPENDIX D

D 1.1 ELECTRICAL ANALOGUE EQUATIONS DERIVATION

The transient heat conduction equation and transmission line equation are derived by Schultz and Jones (1973) as shown below:

a) THERMAL

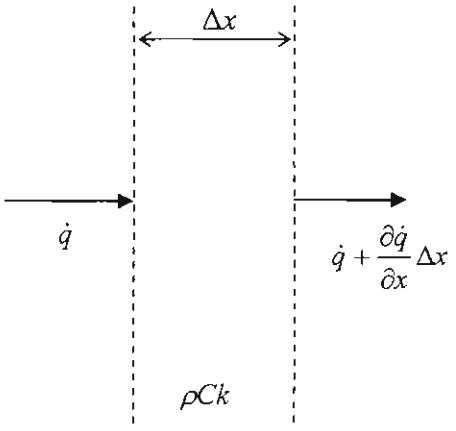

The rate of gain of energy in element Δx

$$= -\frac{\partial \dot{q}}{\partial x}\Delta x \qquad \text{(A-15a)}$$

and by conservation of energy

$$= \rho C \Delta x \frac{\partial T}{\partial t} \qquad \text{(A-16a)}$$

Therefore,

$$\frac{\partial \dot{q}}{\partial x} = -\rho C \frac{\partial T}{\partial t} \qquad \text{(A-17a)}$$

The conduction equation is

$$\dot{q} = -k\frac{\partial T}{\partial x} \qquad \text{(A-18a)}$$

Combining the above equations gives the diffusion equation:

$$\frac{\partial^2 T}{\partial x^2} = \frac{\rho C}{k}\frac{\partial T}{\partial t} \qquad \text{(A-19a)}$$

b) ELECTRICAL

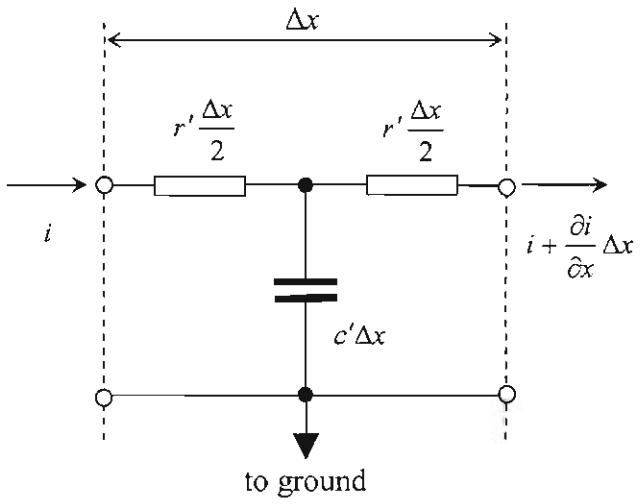

The rate of gain of charge in element Δx

$$= -\frac{\partial i}{\partial x}\Delta x \qquad \text{(A-15b)}$$

and by conservation of energy

$$= c'\Delta x \frac{\partial V}{\partial t} \qquad \text{(A-16b)}$$

Therefore,

$$\frac{\partial i}{\partial x} = -c'\frac{\partial V}{\partial t} \qquad \text{(A-17b)}$$

Ohm's law is

$$i = -\frac{1}{r'\Delta x}\frac{\Delta V}{\Delta x}\Delta x = -\frac{1}{r'}\frac{\partial V}{\partial x} \qquad \text{(A-18b)}$$

Combining the above equations gives the transmission line equation:

$$\frac{\partial^2 V}{\partial x^2} = r'c'\frac{\partial V}{\partial t} \qquad \text{(A-19b)}$$

D 1.2 PROPERTIES OF "ISOTEMP1"

The post processing of the data sampled in the heat transfer experimental tests was performed using a program designed by Snedden (1995) with LabView. The purpose of this program is to reconstruct the wall temperature history (which was captured by WaveView) and calculate the isothermal heat transfer coefficients with certain constants entered by the user.

The basic procedure to acquire these results is to first have a text file in the correct format such that the program does not return any errors. This limits the format to have no headings and any descriptions, and a delimiter (tab) must be used for any spacing within the file. The voltage readings are plotted against the time readings, and the resulting graph should show a voltage step change. This step change can be isolated by cropping the necessary range, and filters are used within the program to achieve a clear signal.

Once the calibration constants and other operating conditions are entered into the program by the user, Istotemp1 converts the voltage readings into heat flux data. The heat flux is plotted against temperature, and a best-fit line (judged by the user) allows the program to calculate the resulting isothermal heat transfer coefficient. These results are performed for every sensor input, and can be saved as a PDF file.

The details and code of Isotemp1 is given in Appendix 4 of the dissertation of Snedden (1995).

APPENDIX E

E 1.1 ROSEMOUNT TRANSDUCERS CALIBRATION DATA

Table E1-1: Rosemount A Data

TIME (S)	MANOMETER HEIGHT (M)	DIFFERENTIAL PRESSURE (KPA)	PLENUM PRESSURE (KPA)	CORRESPONDING VOLTAGE (V)
0	0	0	101.325	1.89
20	0.024	6.403968	94.92103	3.072
40	0.046	12.27427	89.05073	4.071
60	0.066	17.61091	83.71409	4.933
80	0.082	21.88022	79.44478	5.709
100	0.097	25.8827	75.4423	6.4
120	0.111	29.61835	71.70665	7.004
140	0.124	33.08717	68.23783	7.587
160	0.135	36.02232	65.30268	8.125
180	0.145	38.69064	62.63436	8.601
200	0.155	41.35896	59.96604	9.043

Table E1-2: Rosemount B Data

TIME (S)	MANOMETER HEIGHT (M)	DIFFERENTIAL PRESSURE (KPA)	PLENUM PRESSURE (KPA)	CORRESPONDING VOLTAGE (V)
0	0	0	101.325	1.895
20	0.025	6.6708	94.6542	3.145
40	0.047	12.5411	88.7839	4.205
60	0.065	17.34408	83.98092	5.116
80	0.082	21.88022	79.44478	5.893
100	0.097	25.8827	75.4423	6.647
120	0.111	29.61835	71.70665	7.336
140	0.123	32.82034	68.50466	7.949
160	0.135	36.02232	65.30268	8.515
180	0.145	38.69064	62.63436	9.031
200	0.155	41.35896	59.96604	9.512

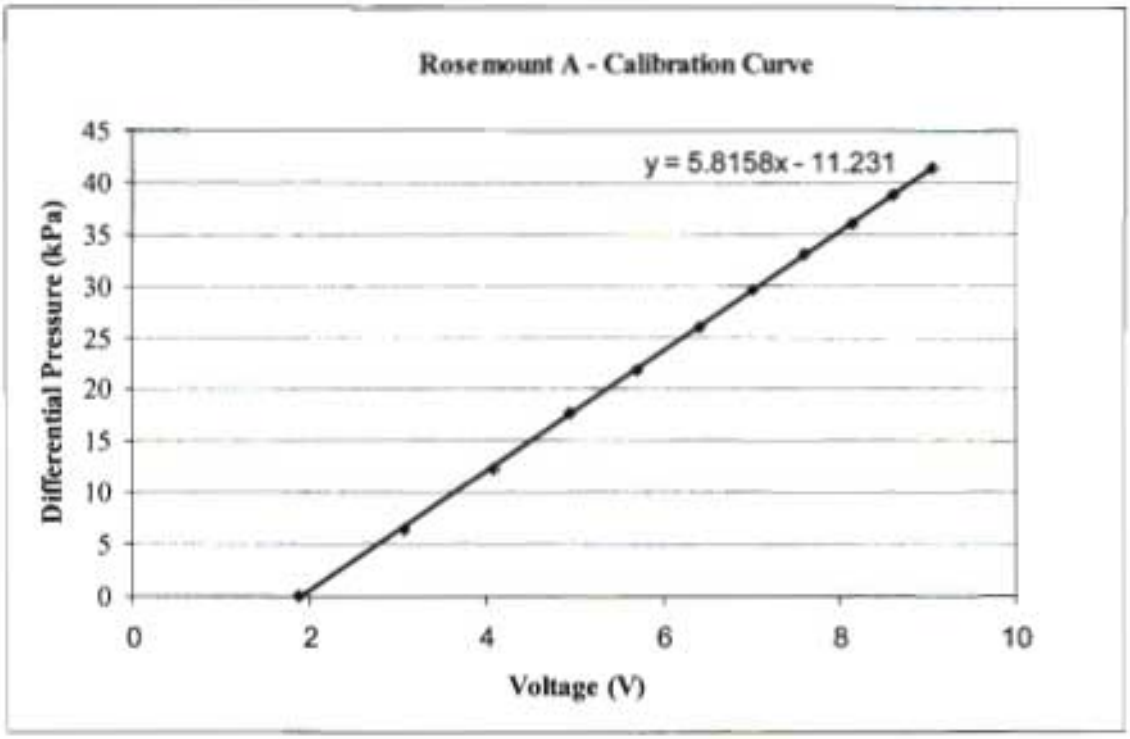

Figure E1-1: Rosemount A calibration curve

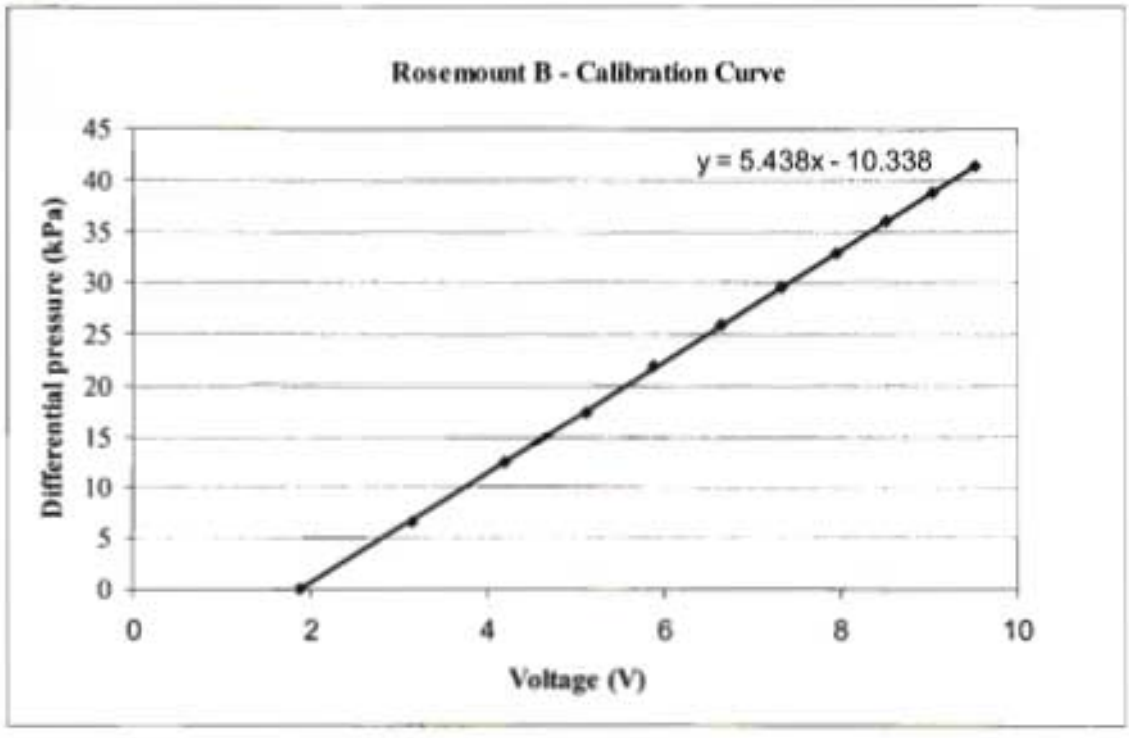

Figure E1-2: Rosemount B calibration curve

E 1.2 KULITE TRANSDUCER CALIBRATION DATA

Table E1-3: Kulite Calibration Data

TIME (S)	MANOMETER HEIGHT (M)	DIFFERENTIAL PRESSURE (KPA)	PLENUM PRESSURE (KPA)	CORRESPONDING VOLTAGE (V)
0	0	0	101.325	0.115
20	0.024	6.403968	94.92103	0.1084
40	0.046	12.27427	89.05073	0.103
60	0.064	17.07725	84.24775	0.098
80	0.079	20.525	80.8	0.095
100	0.092	24.54854	76.77646	0.09
120	0.103	27.4837	73.8413	0.088
140	0.113	30.15202	71.17298	0.085
160	0.123	32.82034	68.50466	0.083
180	0.132	35.22182	66.10318	0.081
200	0.139	37.08965	64.23535	0.078
220	0.146	38.95747	62.36753	0.076
240	0.152	41.525	59.8	0.0733
260	0.157	43.625	57.7	0.071
280	0.162	46.025	55.3	0.068
300	0.167	49.025	52.3	0.065

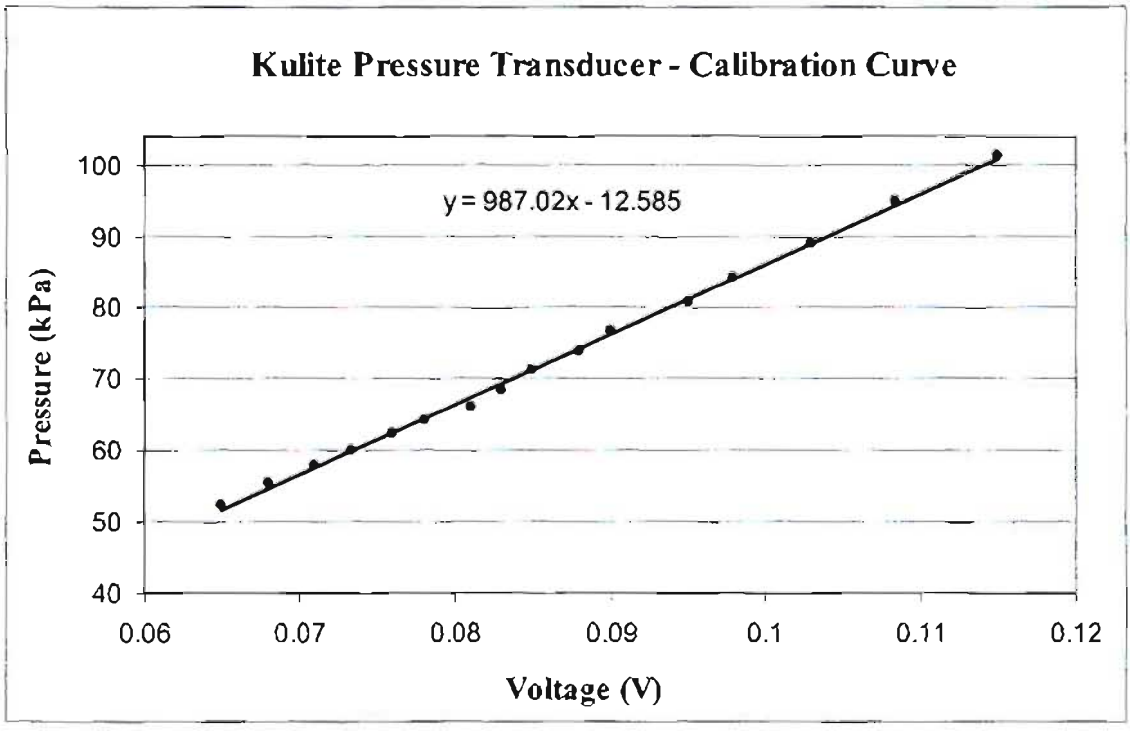

Figure E1-3: Kulite calibration curve

E 1.3 Heat Transfer Circuit Calibration Data

Table E1-4: Circuit Calibration Data

Channel	Test 1	Test 2	Average
0	-2.854	-2.893	-2.873
1	-2.784	-2.752	-2.768
2	-2.735	-2.694	-2.714
3	-2.678	-2.673	-2.676
4	-2.628	-2.644	-2.636
5	-2.611	-2.650	-2.631
6	-2.604	-2.628	-2.616
7	-3.102	-3.111	-3.107

E 1.4 THIN-FILM GAUGES CALIBRATION DATA

Table E1-5: Calibration Data for D-type Connector P1

		PINS	1&2	3&4	5&6	7&8	9&10	11&12	14&15	16&17
T_{AVE} (°C)	KELVIN	SENSOR #	1	2	3	4	5	6	7	8
24.175	297.175	Res (Ω)	141.86	52.38	65.41	62.27	49.51	54.62	52.61	51.29
39.875	312.875		143.89	53.1	66.32	63.21	50.23	55.39	53.41	51.95
59.925	332.925		145.75	53.79	67.19	64.06	51.15	56.07	54.07	52.56
80.125	353.125		149	55	68.69	65.58	51.94	57.38	55.23	53.75
100.15	373.15		151.85	56.06	70.04	66.92	52.92	58.45	56.25	54.78
		GRADIENT	0.1308	0.0483	0.0606	0.0608	0.0444	0.0503	0.0474	0.0458
		y-INTERCEPT	138.5100	51.1280	63.8410	60.7070	48.4500	53.3210	51.4300	50.0790
		R_0 at 40°C (Ω)	143.742	53.06	66.265	63.139	50.226	55.333	53.326	51.911
		α_R	9.1E-04	9.1E-04	9.1E-04	9.6E-04	8.8E-04	9.1E-04	8.9E-04	8.8E-04

Table E1-6: Calibration Data for D-type Connector P2

		PINS	1&2	3&4	5&6	7&8	9&10	11&12	14&15	16&17
T_{AVE} (°C)	KELVIN	SENSOR #	1	2	3	4	5	6	7	8
24	297	Res (Ω)	52.19	53.09	54.44	51.23	51.05	52.29	48.2	131.05
39.825	312.825		52.87	53.8	55.15	51.93	51.75	53	49.21	133.06
59.95	332.95		53.5	54.47	55.82	52.59	52.4	53.73	49.6	134.97
80.05	353.05		54.71	55.7	57.01	53.77	53.57	54.94	50.63	138.07
100.025	373.025		55.75	56.78	58.04	54.76	54.6	55.99	51.67	140.79
		GRADIENT	0.0467	0.0484	0.0472	0.0464	0.0465	0.0487	0.0434	0.1275
		y-INTERCEPT	50.9650	51.8290	53.2230	50.0380	49.8490	51.0320	47.2240	127.840
		R_0 at 40°C (Ω)	52.833	53.765	55.111	51.894	51.709	52.98	48.96	132.94
		α_R	8.8E-04	9.0E-04	8.6E-04	8.9E-04	9.0E-04	9.2E-04	8.9E-04	9.6E-04

Table E1-7: Calibration Data for D-type Connector P3

		PINS	1&2	3&4	5&6	7&8	9&10	11&12	14&15	16&17
T_{AVE} (°C)	KELVIN	SENSOR #	1	2	3	4	5	6	7	8
23.95	296.95	Res (Ω)	51.56	51.12	51.44	50.62	50.86	51.37	69.87	121.37
39.95	312.95		52.33	51.84	52.18	51.36	51.55	52.13	71	123.2
59.925	332.925		53.05	52.54	52.9	52.07	52.34	52.87	72.1	125.22
80.025	353.025		54.2	53.72	54.07	53.23	53.45	54.08	73.89	127.76
100.1	373.1		55.21	54.71	55.07	54.21	54.43	55.07	74.96	130.14
		GRADIENT	0.0477	0.0472	0.0476	0.0471	0.0471	0.0487	0.0680	0.1150
		y-INTERCEPT	50.3690	49.9180	50.2360	49.4340	49.6650	50.1450	68.2330	118.550
		R_0 at 40°C (Ω)	52.277	51.806	52.14	51.318	51.549	52.093	70.953	123.15
		α_R	9.1E-04	9.1E-04	9.1E-04	9.2E-04	9.1E-04	9.3E-04	9.6E-04	9.3E-04

Table E1-8: Calibration Data for D-type Connector P4

		PINS	1&2	3&4	5&6	7&8	9&10	11&12	14&15	16&17
T_{AVE} (°C)	KELVIN	SENSOR #	1	2	3	4	5	6	7	8
24.075	297.075	Res (Ω)	52.15	52.12	63.97	57.95	52.13	51.42	63.97	60.27
39.825	312.825		52.85	52.82	64.94	58.76	52.91	52.17	64.94	61.16
59.825	332.825		53.69	53.66	66.08	59.74	53.88	53.09	66.08	62.15
79.75	352.75		54.73	54.69	67.4	60.87	54.94	54.16	67.4	63.38
100.025	373.025		55.68	55.65	68.62	61.92	56.02	55.12	68.62	64.52
		GRADIENT	0.0466	0.0466	0.0613	0.0524	0.0512	0.0490	0.0613	0.0559
		y-INTERCEPT	50.9880	50.9600	62.4800	56.6660	50.8700	50.2190	62.4800	58.9020
		R_0 at 40°C (Ω)	52.852	52.824	64.932	58.762	52.918	52.179	64.932	61.138
		α_R	8.8E-04	8.8E-04	9.4E-04	8.9E-04	9.7E-04	9.4E-04	9.4E-04	9.1E-04

Table E1-9: Calibration Data for D-type Connector P5

		PINS	1&2	3&4	5&6	7&8	9&10	11&12	14&15	16&17
T_{AVE} (°C)	KELVIN	SENSOR #	1	2	3	4	5	6	7	8
23.9	296.9	Res (Ω)	59.62	54.61	70.02	66.04	52.19	54.03	51.74	52.53
39.925	312.925		60.52	55.43	71.12	67.04	52.7	54.89	52.74	53.33
59.975	332.975		61.55	56.36	72.31	68.15	53.44	55.79	53.43	54.21
79.95	352.95		62.82	57.56	73.86	69.63	54.56	57.01	54.56	55.39
99.85	372.85		64.02	58.66	75.3	71.01	55.59	58.18	55.51	56.42
		GRADIENT	0.0579	0.0534	0.0693	0.0654	0.0453	0.0543	0.0487	0.0513
		y-INTERCEPT	58.1920	53.2840	68.3110	64.4060	50.9460	52.6800	50.6390	51.2600
		R_0 at 40°C (Ω)	60.508	55.42	71.083	67.022	52.758	54.852	52.587	53.312
		α_R	9.6E-04	9.6E-04	9.7E-04	9.8E-04	8.6E-04	9.9E-04	9.3E-04	9.6E-04

Table E1-10: Calibration Data for D-type Connector P6

		PINS	1&2	3&4	5&6	7&8	9&10	11&12	14&15	16&17
T_{AVE} (°C)	KELVIN	SENSOR #	1	2	3	4	5	6	7	8
23.75	296.75	Res (Ω)	51.58	51.03	52.34	63.07	58.34	64.96	51.51	51.98
39.8	312.8		52.41	51.81	53.12	64.05	59.16	66.15	52.72	52.28
59.775	332.775		53.31	52.66	53.98	65.1	60.11	67.57	53.72	53.26
79.925	352.925		54.47	53.74	55.07	66.46	61.35	70.18	55.93	55.33
99.85	372.85		55.59	54.77	56.11	67.66	62.56	73.19	58.21	57.66
		GRADIENT	0.0525	0.0490	0.0494	0.0603	0.0554	0.1071	0.0867	0.0756
		y-INTERCEPT	50.2920	49.8340	51.1300	61.6130	56.9490	61.9210	49.1640	49.5180
		R_0 at 40°C (Ω)	52.392	51.794	53.106	64.025	59.165	66.205	52.632	52.542
		α_R	1.0E-03	9.5E-04	9.3E-04	9.4E-04	9.4E-04	1.6E-03	1.6E-03	1.4E-03